WOOD AND FIBER SCIENCE

The Sustainable Natural Materials Journal

Volume 57, Number 1, 2025 (ISSN 0735-6161)

Open Access

JOURNAL OF THE

SWST – International Society of Wood Science and Technology

EDITORIAL AND PUBLICATION POLICY

Wood and Fiber Science as the official publication of the Society of Wood Science and Technology publishes open access papers with both professional and technical content. Original papers of professional concern, or based on research of international interest dealing with the science, processing, and manufacture of wood and composite products of wood or wood fiber origin will be considered.

All manuscripts are to be written in US English, the text should be proofread by a native speaker of English prior to submission. Any manuscript submitted must be unpublished work not being offered for publication elsewhere.

Papers will be reviewed by referees selected by the editor and will be published in approximately the order in which the final version is received. Research papers will be judged on the basis of their contribution of original data, rigor of analysis, and interpretations of results; in the case of reviews, on their relevancy and completeness.

Color photos/graphics will be offered at no additional cost to authors. The Open Access fee will be $1800/article for SWST members and $2000/article for nonmembers. Reduced rates are available for authors based in developing countries.

Technical Notes

Authors are invited to submit Technical Notes to the Journal. A Technical Note is a concise description of a new research finding, development, procedure, or device. The length should be **no more than two printed pages in WFS**, which would be five pages or less of double-spaced text (TNR12) with normal margins on 8.5 x 11 paper, including space for figures and tables. In order to meet the limitation on space, figures and tables should be minimized, as should be the introduction, literature review and references. The Journal will attempt to expedite the review and publication process. As with research papers, Technical Notes must be original and go through a similar double-blind, peer review process.

On-line Access to *Wood and Fiber Science* Back Issues

SWST is providing readers with a means of searching all articles in *Wood and Fiber Science* from 1968 to present.

Visit the SWST website at https://www.swst.org and go to Wood & Fiber Science Online. Click on either SWST Member Publication access (SWST members) or Subscriber Publication access (Institution Access). All must login with their email and password on the https://www.swst.org site or use their ip authentication if they have a site license.

As an added benefit to our current subscribers, you can now access the electronic version of every printed article along with exciting enhancements that include:

- IP authentication for institutions (only with site license)
- Enhanced search capabilities
- Email alerting of new issues
- Custom links to your favorite titles

(ISSN 0735-6161)

WOOD AND FIBER SCIENCE

JOURNAL OF THE SOCIETY OF WOOD SCIENCE AND TECHNOLOGY

VOLUME 57 JANUARY 2025 NUMBER 1

CONTENTS

Articles

Printability and mechanical properties of wood resin polymer composites manufactured using stereolithography

Oladayo Ariyo†
Graduate Student
Department of Applied Engineering Technology
North Carolina Agricultural and Technical State University,
Greensboro, North Carolina, U.S.A.
E-mail: oariyo@aggies.ncat.edu

Wenjia Wang
Assistant Professor
Department of Wood Science and Engineering,
Oregon State University
Corvallis, Oregon, U.S.A
E-mail: wenjia.wang@oregonstate.edu

James D. Kribs
Assistant Professor
Department of Applied Engineering Technology
North Carolina Agricultural and Technical State University
Greensboro, North Carolina, U.S.A
E-mail: jdkribs@ncat.edu

*Aixi Zhou**
Vice Provost of Research and Innovation; Professor of Engineering
Norfolk State University
Norfolk, Virginia, U.S.A
E-mail: azhou@nsu.edu

(Received 24 September 2024)

Abstract. Wood polymer composites (WPC) fabrication using stereolithography has received little attention. WPC research has been mostly directed to traditional manufacturing methods and fused deposition modeling. Stereolithography offers better print precision, structural accuracy, and ease of production than other 3D printing methods and directly creates the final wood polymer composite. Typically, WPCs fabricated using traditional methods used 40-60% wood in the mixture; however, the highest ratio used with stereolithography has been 10%. Increased wood content reduces costs and creates a product that more closely resembles the mechanical properties of wood. This study focused on increasing the wood flour ratio of WPC printed using stereolithography beyond 10% while studying the factors influencing printability and the mechanical properties of the printed materials. A blend of maple and oak wood flour was combined with methacrylate-based resin at wood levels of 2.5, 5, 7.5, 10, 12.5, 15, and 17.5 wt. % to fabricate the wood polymer composite. The highest ratio of wood flour successfully printed in this study was 17.5 wt.%. This paper discusses the tensile and compressive behaviors of the WPC, as well as the dimensional accuracy of the stereolithography process for higher wood ratio WPC fabrication. The process of fabrication, post processing, success and failure in printing, and characterization of print defects were also studied. Stereolithography can be used to manufacture wood polymer composites in a direct production method at higher wood flour ratios, and improving the capability of the method holds the potential to increase access to a sustainable substitute for conventional wood for various uses.

Keywords: Wood, Wood Polymer Composite, 3D Printing, Stereolithography, Sustainability

Introduction

The growing need for sustainable composite materials has spurred interest in pairing wood and other natural fibers with polymers. Wood, renowned for its specific strength, stiffness, biodegradability, and non-abrasive nature, is particularly appealing as a reinforcing material (Bledzki et al. 2005; Nachtigall et al. 2007). The use of natural fibers in this capacity has witnessed substantial growth in recent years, due to advantages such as lower production cost, density, ease of preparation, and reduced energy requirements for processing (Baley 2002; Bledzki 1999; Oksman et al. 2003; van Voorn et al. 2001). Wood polymer composite or wood plastic composite (WPC)

* Corresponding author
† Society of Wood Science & Technology member

are materials generated from the amalgamation of wood-derived elements like sawdust or lumber fibers with polymers to produce a composite material (Gardner et al. 2015; Schwarzkopf and Burnard 2016). These composites exhibit improved mechanical properties, moisture resistance, biological resistance and high molding performance (Huang et al. 2021). Given the different anatomical structures of various wood species, and the chemical structure of polymers, a blend of both produces distinct physical, thermal, and mechanical properties, paving the way for a new generation of hybrid materials (Youngquist et al. 1994). Wood fibers contribute to the composite's overall strength and stiffness, while the polymer matrix binds it together and provides flexibility (Faruk et al. 2012; Peltola et al. 2014). Strength and stiffness are essential properties in architectural applications, ensuring structural integrity and durability. Conversely, materials with high compliance provide flexibility and adaptability, making them ideal for applications requiring resilience and the ability to deform under stress without sustaining permanent damage. Composites that balance these attributes have significant potential in various applications, including flooring and other architectural elements. Custom furniture, decorative paneling, fences, and decking. In the automotive industry, Stereolithography -printed WPCs can be used for interior components such as dashboard panels, trim, and other decorative elements(Krapež Tomec and Kariž 2022). Other areas of use can be found in art installations, prototyping, and consumer goods manufacturing(Khan et al. 2020).

Stereolithography (SLA) outperforms other 3D printing methods for WPCs when considering ease of production, print precision and build resolution (Wang et al. 2017). The print precision of SLA improves structural accuracy, making it a viable development technique for WPC (Chan et al. 2018). SLA is a vat-polymerization technique that utilizes UV light in a layer-by-layer photopolymerization process to selectively cure liquid resin, transforming it into a solid three-dimensional structure (Bártolo 2011; Schmidleithner and Kalaskar 2018), which is illustrated in Figure 1. Objects created through this approach have gained widespread popularity and are used across various industries including automotive, architecture, and medicine (Dizon et al. 2021; Schmidleithner and Kalaskar 2018). Thermoset polymers like epoxy, polyvinyl ester, polyester, polyurethanes, and phenolics are employed in SLA, and have been used for fabricating polymer composites. Epoxy resin is commonly favored for composite development due to numerous advantages including high interfacial adhesion with fillers, low viscosity, enhanced wettability, thermal stability, superior mechanical performance, minimal shrinkage after curing, and improved chemical resistance (Khan et al. 2020; Shi et al. 2017).

A variety of wood-based materials such as lignin, sawdust, and wood powder can be utilized in SLA-based 3D printing to create wood polymer composites with enhanced mechanical and physical properties. SLA allows particle reinforcements to be easily added (Yao and Hakkarainen 2023). In one study, Zhang et al. (2019) used a softwood kraft lignin as a filler in SLA 3D printing to reinforce the mechanical properties of printed products. Tensile testing revealed that adding lignin to the composite increased the tensile strength by 46−64% and the Young's modulus by 13−37% compared to the control sample (without lignin). Incorporating 0.4 wt. % softwood kraft lignin resulted in the printed composite achieving its highest tensile strength of 49.0 MPa, which represented a 60% increase in comparison to the control. Sutton et al. (2018) produced resins containing up to 15% lignin that displayed outstanding printing quality, strong layer fusion, high surface definition, and visual clarity. They reported that the ductility of printed parts rose with increased lignin concentration. Vidakis et al. (2022) also reinforced a medical-grade UV-cured resin (BioMed Clear) used in SLA 3D printing with cellulose nanofiber nanocomposites at concentrations ranging from 0.5 wt.% to 2.0 wt.%. They found improved mechanical properties, even at fractions as low as 0.5 wt.%. Tensile strength rose from 24.89 MPa (pure resin) to 50.25 MPa (Biomed Clear / cellulose nanofiber blend (CNF) 1.0 wt.%). Even greater improvements were observed for the flexural properties where the flexural strength increased by over 300% for the Biomed Clear CNF 0.5 wt.% (Vidakis et al. 2022). The incorporation of wood-derived reinforcements like wood flour/particles, lignin, and cellulose nanofibers into SLA resins can enhance tensile strength, modulus, and impart unique wood-like characteristics to the printed composites. Specific property values depend on the resin formulation and wood reinforcement type/loading, but the results show the potential for integrating wood flour into resins for fabricating wood polymer composites.

WPC properties vary depending on the type of wood, polymer, processing methods, and additives (Anish et al. 2023). Other notable factors influencing WPC properties are the shape, size and proportion of wood particles. The proportions of wood flour mixed with polymer have a considerable impact on both the processing and end-use properties. For instance, Huang et al. (2021) discovered that the tensile strength of 3D printed WPCs using fused deposition modeling (FDM) increased by 27% with the addition of wood components ranging from 19 wt.% to 29 wt.%. Kariz et al. (2018) found that up to

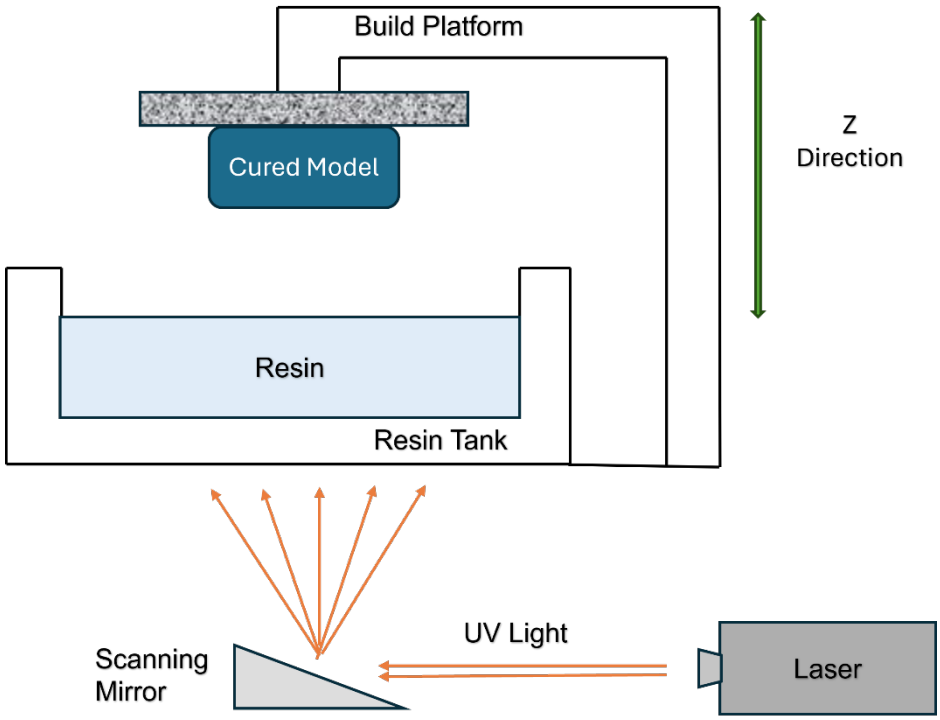

Figure 1. A schematic diagram of the process of stereolithography.

10% of wood particles slightly reinforced a WPC filament used in FDM 3D printing, but higher wood levels decreased tensile strength. Chaudemanche et al. (2018) observed that both bending strength and modulus rose with increased wood powder particle concentration. Higher wood ratios have other benefits brought about using less polymer (Sommerhuber et al. 2017). More wood enhances the physical appearance of the composite, making it resemble actual wood, and increasing its wood-like characteristics, while lowering production cost, since it is cheaper to use more wood and less resin (Fu et al. 2022; Pringle et al. 2017). Higher wood concentrations enhance hardness, while increased plastic matrix augments the toughness of the composite material (Jian et al. 2022). To maximize these benefits, it is preferable to have a high wood flour content, typically 50 wt.% or higher in traditional methods. Commercial WPC products typically utilize wood flour contents of up to 70% (Matuana and Stark 2015). However, increased filler amounts significantly raise the viscosity of the polymer melt, making flow and forming processes more challenging (Mazzanti and Mollica 2020). Wood species used for reinforcement are based on availability and ease of access rather than on characteristics (Tanaka and Ito 2013). Hemp, ramie, and kenaf are utilized as fillers in Southeast Asia due to their abundance. Conversely softwoods such as white pine, spruce, and hemlock, as well as hardwoods like aspen, oak, and maple are the primary species employed in the US as fillers (Clemons 2008; Clemons and Caulfield 2005; Pokhrel et al. 2021). Berger and Stark (1997) revealed that hardwood species offer enhanced tensile properties and superior heat deflection in comparison to softwoods.

Limited research has been done on the behavior of WPCs fabricated using SLA at high wood flour ratios (e.g., 10 wt.% or higher). Zhang et al. (2021) successfully used SLA to fabricate WPCs at ratios ranging from 1 to 10 wt.%. Their addition of 1% poplar wood flour to methacrylate resin greatly improved the tensile strength and Young's modulus of the printed WPCs. The purpose of this current study was to fabricate WPCs using SLA at ratios higher than 10 wt.% using a 1:1 oak/maple wood flour blend. Oak and maple were chosen due to their high cellulose content which improves structural properties of wood. Increased wood flour content will enhance the suitability of SLA for fabricating WPCs for commercial purposes.

Materials and methods

Wood flour (Fasco Epoxies, Fort Pierce, FL, USA), was a blend of two hardwoods, Maple, and Oak. The particle size of the wood flour was 80 mesh (177 um). The wood flour was dried at 103°C for 24 hours, resulting in a measured moisture content of 3%, as determined by a Reed dual moisture meter.

The thermoset resin used in this study was RS-F2-DUCL-02 (Formlabs Inc., Sommerville, MA USA) with a density of 1.06 g/cm^3. The resin formulation contained methacrylic acid esters, photo-initiators, proprietary pigment, and additive packages, with viscosities of 2051 and 981 cp at 25 and 35°C, respectively.

The 3D printer used was a Formlabs Form 3 printer (Formlabs Inc., Sommerville, MA USA) with a preset UV light wavelength of 405 nm. Isopropyl alcohol, utilized for washing purposes, was procured from USA Lab, (Livonia, MI, USA). Additionally, a UV curing chamber and wash basin were obtained from Formlabs Inc.

STL files containing models of ASTM D695 and ASTM D638 Type V were generated using AutoCAD Fusion 360 and sliced using Formlabs Preform slicing software before being uploaded to the 3D printer. The layer height of each print was set at 0.1 mm, and a default build orientation of 0 degrees was chosen. The wood flour and resin were manually mixed at room temperature (25°C) until a consistent blend was obtained. This method was used to prevent phase separation while being held in any containers. The resin was not diluted because its viscosity was considered an integral factor in procuring increased wood flour ratios. Hand stirring was found to be the best form of blending due to the increased viscosity of the resin. Resin (300 g) was measured for the printing process; the wood flour was divided into 2.5 wt.% increments were added to the resin to levels of 5, 7.5, 10, 12.5, 15 and 17.5 wt.%. The control samples with dimensions can be seen in Figure 2.

The wood-polymer blend was added to the resin tank and printing commenced at 35°C. Samples were fabricated based on ASTM standards D638 Type V (tensile coupon) and D695 (compression coupons). Fabrication of ten samples was attempted at each ratio for both ASTM standards. After printing, the successful samples were moved to an isopropyl alcohol wash station for 20 minutes to remove excess resin. The samples were then cured in a UV chamber for 60 minutes at 60°C. The dimensions of all samples were measured using an Insize 1114-150A digital caliper to determine accuracy. A summary of the printed samples is in Table 1. Samples were given specimen IDs for easy identification. Scanning electron microscopic imaging was performed using a Zeiss Evo LS Environmental SEM to observe the surface and microstructure of the WPCs. The dimensional accuracy of the samples was determined using a vernier caliper, as part of the study on printability, while failure modes observed during the printing process were also identified and recorded.

Mechanical testing

Tensile testing was conducted at room temperature (25°C) using an Instron 5969 universal testing machine (Instron, Norwood, MA, USA) following the guidelines outlined in ASTM D 638: Standard Test Method for Tensile Properties of Plastics.

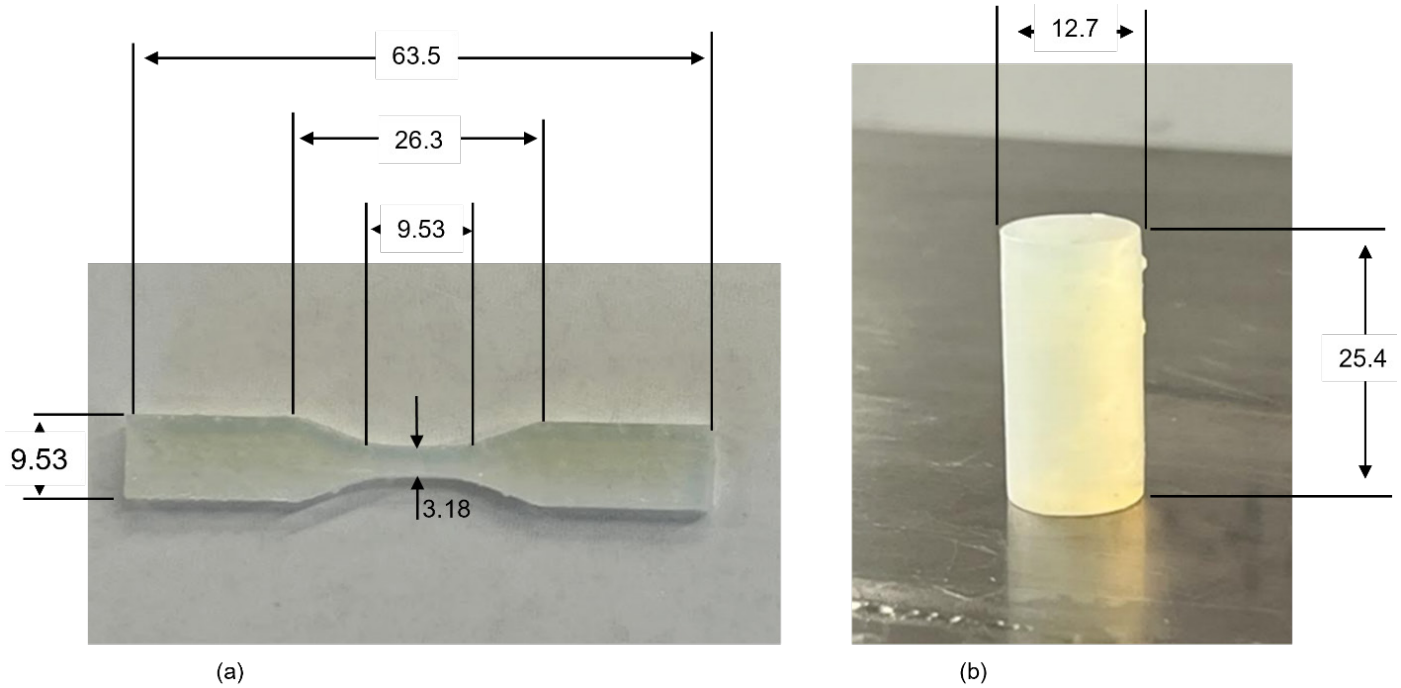

Figure 2. Examples of test specimens used for (a) WPC1 ASTM D638 and (b)WPC1 ASTM D695. Measurements in mm.

Table 1. Effect of wood flour content on ability to produce acceptable specimens for ASTM Standards D638 and D695.

wt.% Wood Content (nominal)	Specimen ID	wt.% Wood Content (measured) Ave. ± S.D	Number of Successful D638 Specimens	Number of Successful D695 Specimens
0.0	WPC1	0.00	10	10
2.5	WPC2	2.65 ± 0.11	10	10
5.0	WPC3	5.30 ± 0.21	10	8
7.5	WPC4	7.95 ± 0.32	10	8
10.0	WPC5	10.60 ± 0.42	10	9
12.5	WPC6	13.25 ± 0.53	10	8
15.0	WPC7	15.90 ± 0.64	10	9
17.5	WPC8	18.55 ± 0.74	7	4

Compression testing followed the guidelines outlined in ASTM D 695: Standard Test Method for Compressive Properties of Rigid Plastics The load cell had a capacity of 50 KN, and the crosshead speed was 1 mm/min for tensile testing and 2.5 mm/min for compression testing. Seven samples were used for tensile testing, while five samples were used for compression testing (except WPC8 with only four specimens). The reduced replication reflected printing failures that precluded testing.

Results and discussion

The ASTM D638 and D695 coupons were successfully fabricated at increased wood floor content higher than 10 wt. % when blended with epoxy resin, with both sample types peaking at 17.5 wt.% of wood flour. Samples did not fully form the intended model and did not print when 20 or 22.5% wood flour was added, at all respectively. This was attributed to decreased melt flow and increased viscosity of the resin mixture upon high wood flour addition. A reduction in UV light penetration was observed, and without the curing, laser print failure was inevitable. The wood flour darkened the printed polymer composite samples, and an increasing darkness was observed as the wood ratio increased (Figure 3). The texture of the composites was grainier at higher wood content above 12wt.%, particularly with the cylindrical shaped samples. This was attributed to the uneven shape of the wood particles and the continuous redistribution of wood flour during the printing process due to the movement of the build plate. Both sample types showed a distinct color change due to increased wood flour content. Figure 4 shows the SEM of wood flour particles suspended within the matrix of a WPC8 sample. Uniform distribution and alignment of wood fibers within the polymer matrix are critical for maximizing tensile strength. This uniform distribution was not guaranteed in this process due to the movement of the build plate.

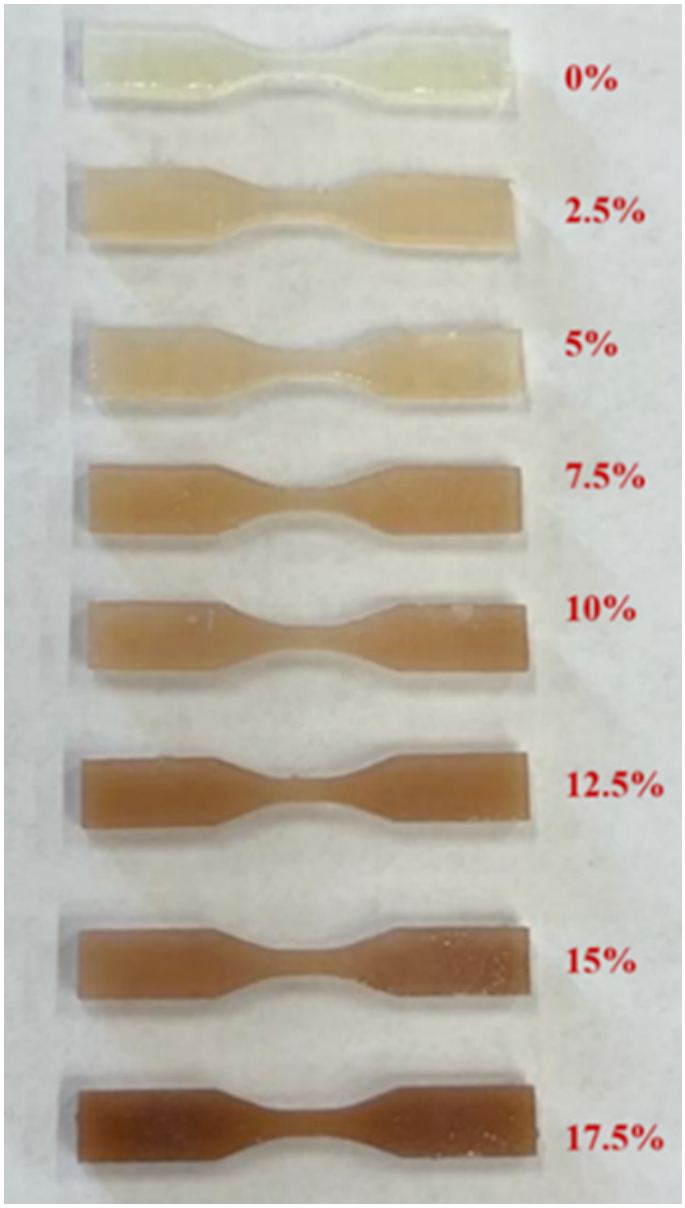

Figure 3. Color gradient changes observed in tensile coupons with increased wood flour content (wt. %).

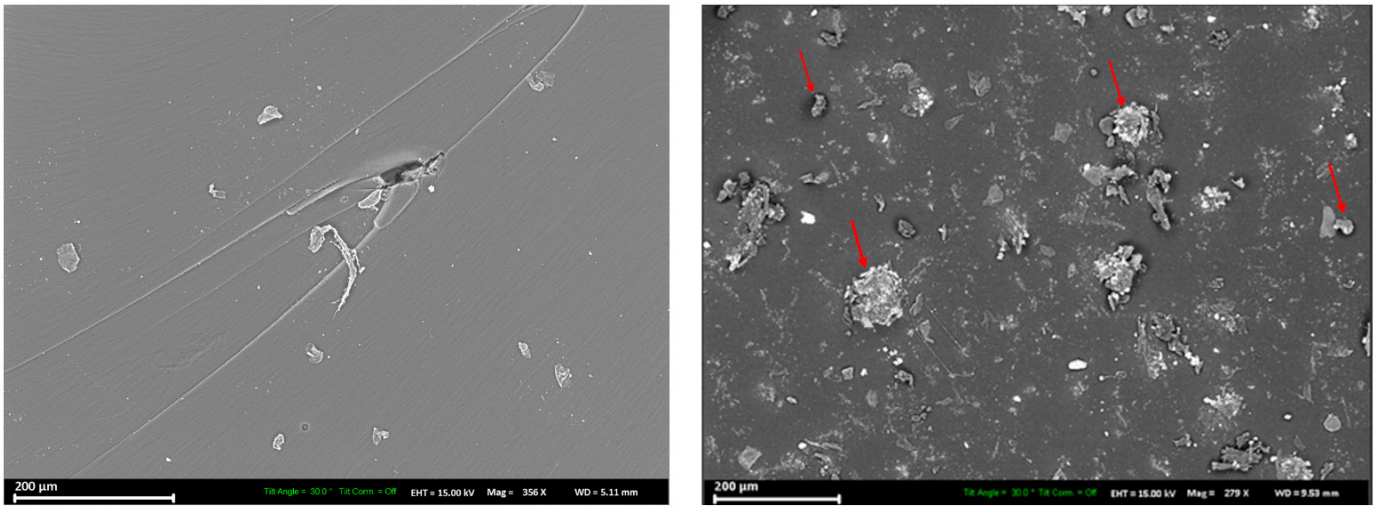

(a) (b)

Figure 4. SEM images of cross sections of tensile coupons with (a) no wood and (b) 17.5 wt.% wood showing wood flour dispersion. The white circles in image (b) are suspended wood flour.

Printability

Printability is an important consideration in various printing processes, including offset and digital printing. In 3D printing, printability pertains to the final appearance and structural accuracy of the printed materials. Good printability characteristics yield high-quality, dimensionally accurate, and visually appealing results. Considerations given to printability in this paper are important because wood polymer fabrication using SLA is less common and requires more process clarity. Printability will be discussed in terms of the success and failure of the samples and dimensional accuracy. A successful sample was categorized as one that was fully printed with accurate dimensions within allowed tolerances (measured using a vernier caliper), had little to no surface roughness and high print resolution. Failed samples were classed as samples fabricated with deformities, inaccurate dimensions, and incomplete curing (undeveloped features). As shown in Table 1, ASTM D638 coupons with 2.5 to 15 wt.% of wood flour ratio were 100% successful, while the samples with 17.5wt.% had a 70% success rate (7 of 10). The ASTM D695 coupons showed more variance in success. The 2.5 wt.% ratio was 100% successful, 10 and 15 wt.% ratios were 90% (9 of 10) successful, and 5, 7.5 and 12.5 wt.% were 80% successful (8 of 10), while 17.5 wt.% showed the lowest success rate at 40% (4 of 10). Major printing factors that affect print success in stereolithography are intensity of laser power, layer height, print speed, curing time and printing resolution (Wang et al. 2017; Mohammadizadeh and Fidan 2021)

Dimensional accuracy

Dimensions for the cylindrical (ASTM D695) and dog-bone (ASYM D638) test specimens were measured to study fabrication accuracy. All measurements were performed thrice using a digital caliper. For the cylindrical coupon, diameter and length were measured, while for the dog-bone coupon, width and thickness of the gauge section were measured. The graphs in Figure 5 show the dimensions of length and diameter of the compression coupon, as compared to the no wood control. Figure 6 shows the thickness and width measurements of the tensile coupon as compared to the control. The dimensional deviations observed in the compression samples were 0.076 mm for width and 0.154 mm for thickness. For the tensile coupons, the deviations were 0.421 mm for length and 0.145 mm for diameter. Insufficient compatibility between the polymer and wood fibers can result in weak interfaces, leading to uneven shrinkage during cooling. In addition, some polymers used in WPCs exhibit significant shrinkage during solidification, exacerbating dimensional inaccuracies. Further study of the polymer feedstock could improve our understanding of this phenomenon. Polymerization shrinkage affects the final dimensions of composites when monomers pack closer together during the polymerization process (Schricker 2017).

Printing failure modes

The failure modes observed during printing were categorized and documented for similarities; this was used to identify several types of defects present in wood polymer composite fabrication using stereolithography. Those listed here do not represent an exhaustive list but are the defects observed during this experiment.

- *Non-Adherence* is when the part partially or fully detached from the build plate before print completion.

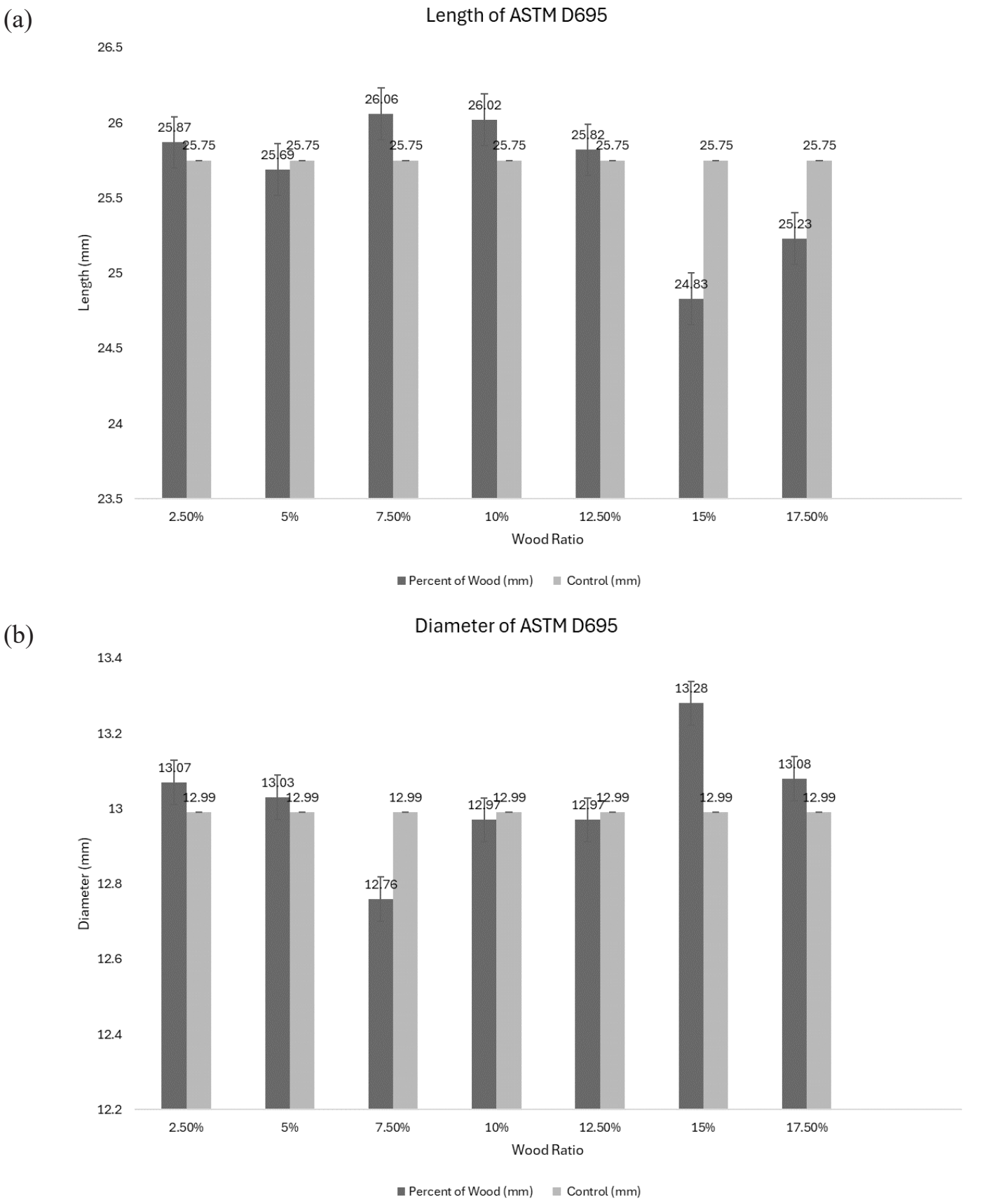

Figure 5. Effect of increased wood flour addition on (a) ASTM D695 cylinder length and (b) ASTM D695 cylinder diameter. Error bars represent one standard deviation.

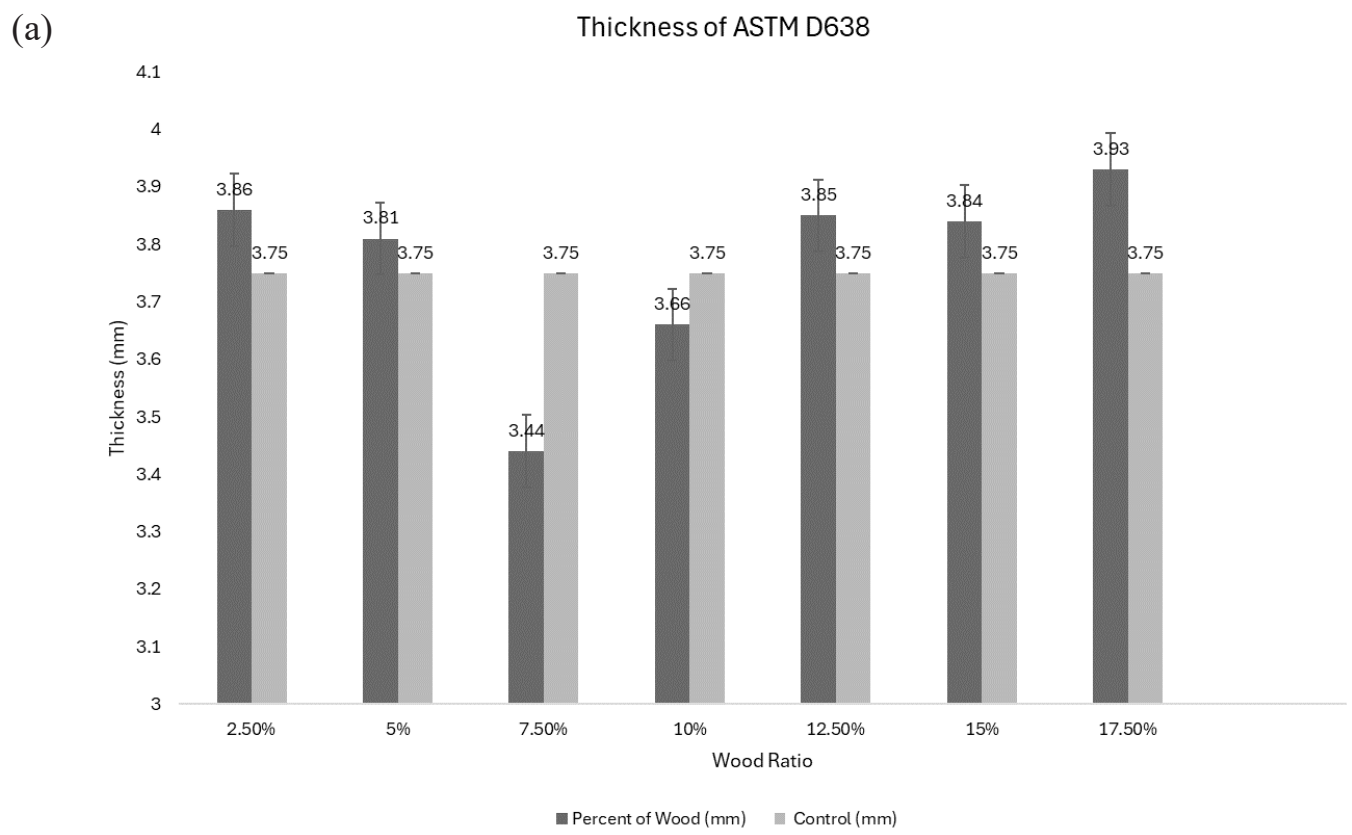

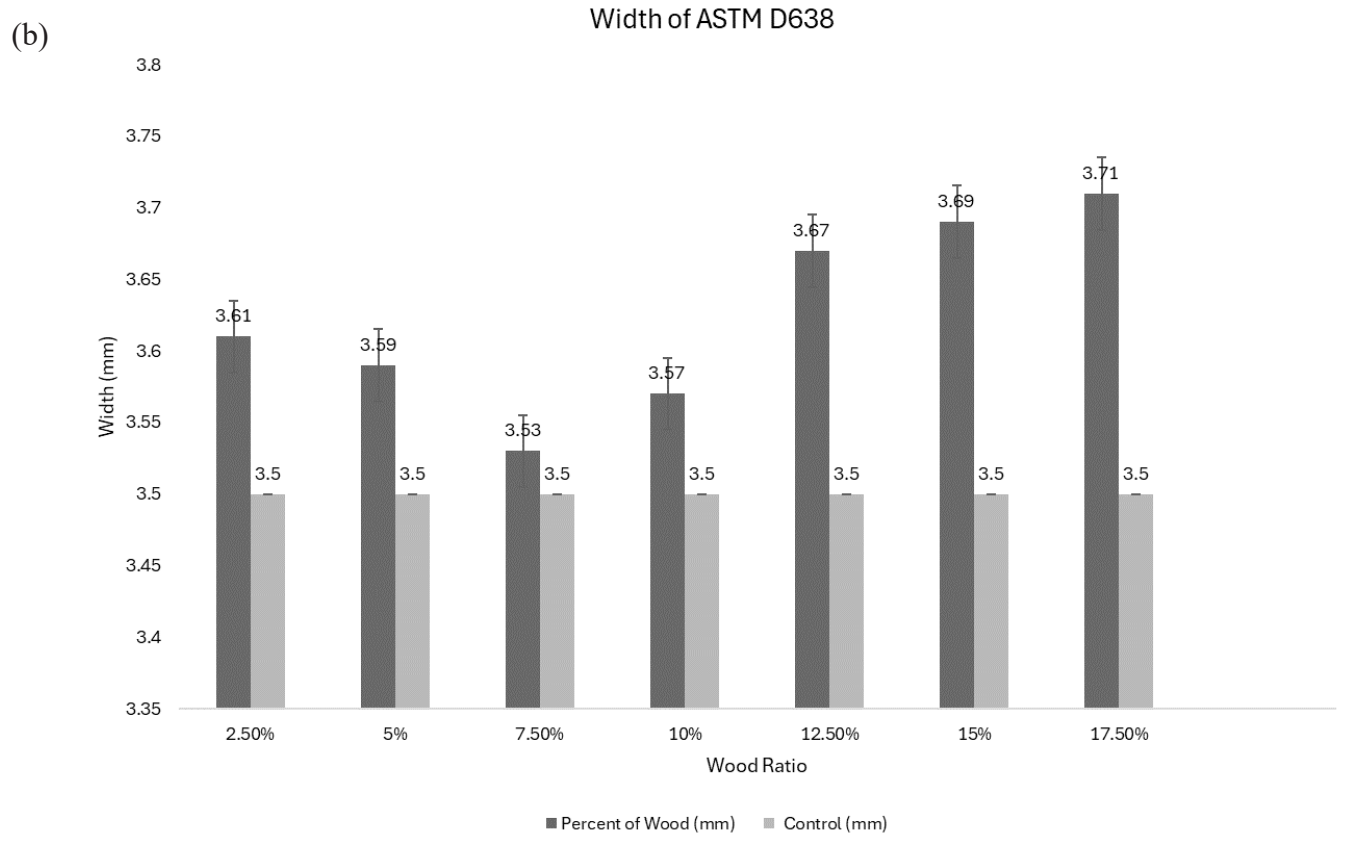

Figure 6. Effect of increased wood flour addition on (a) ASTM D638 dog-bone thickness (b) ASTM D638 dog-bone width. Error bars represent one standard deviation.

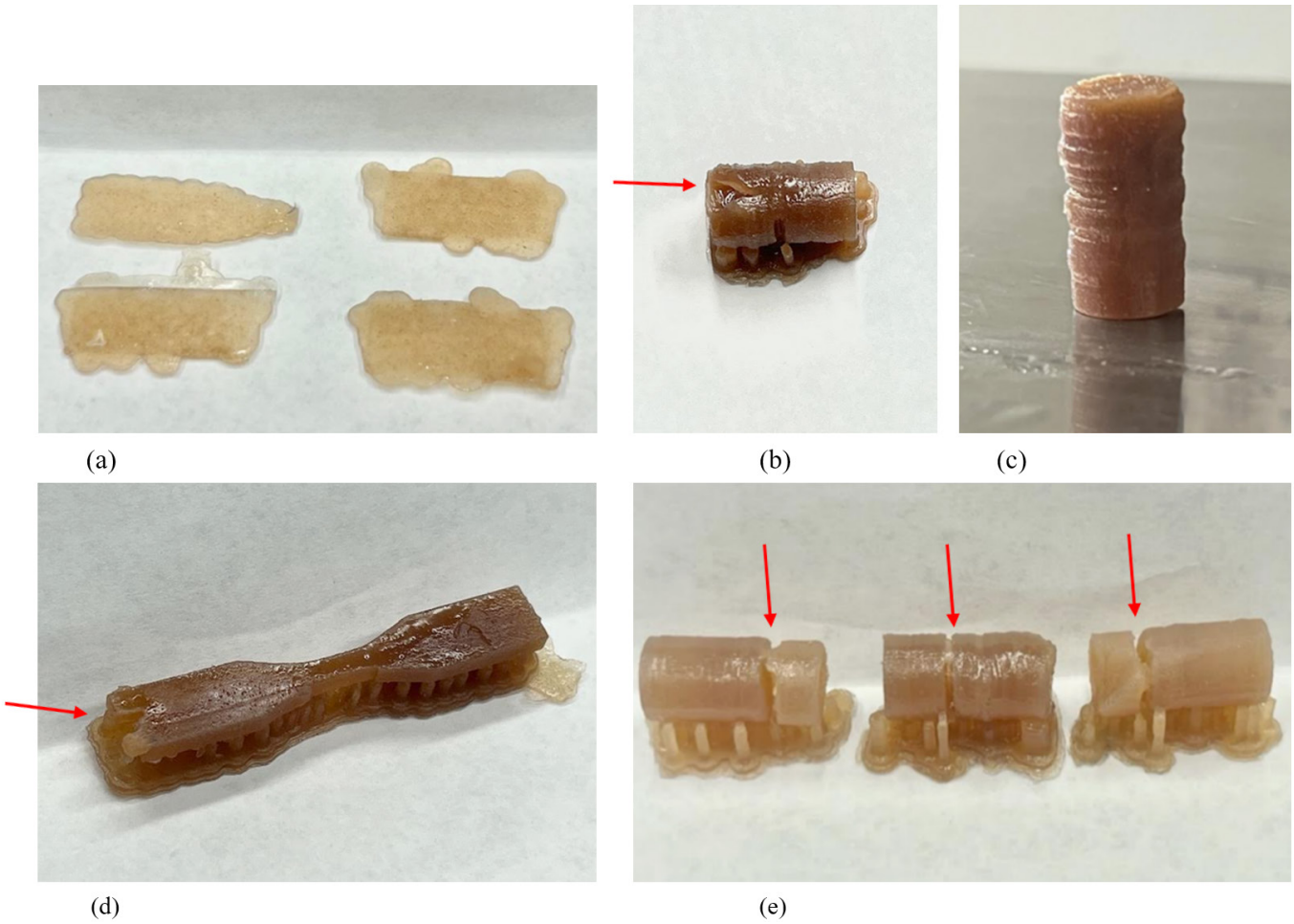

Figure 7. Examples of defects observed in the fabrication of 3D printed WPC samples. (a) Raft silhouettes observed in ASTM D695 that occur when the first printed layer sticks to the build plate but preceding layers do not adhere (b) Cuts observed in 17.5 wt.% woodflour ASTM D695 coupons (c) Surface roughness observed in 17.5 wt.% wood flour sample (d) Incomplete curing at the edge of a 17.5 wt.% wood flour ASTM D638, (e) Pinholes and cuts observed in 10.0 wt.%. and 12.5 wt.%. wood flour ASTM D695 coupons.

- *Raft Silhouetting* occurred when the first layer of the print stuck to the build plate, but the preceding layers did not adhere, resulting in a failed print for that sample. This can also occur when the first layer sticks to the base of resin tank, as in bottom-up 3D printers and the preceding layers do not adhere (Figure 7a). This was observed at higher wood flour ratios. This can be attributed to wood flour clouding the resin tank and restricting UV light penetration (Formlabs Inc 2023).
- *Incomplete Curing and Dimensional Inaccuracy* occurred when inadequate polymer curing resulted in a distortion in the sample shape resulting in undeveloped features and an incomplete print. This was due to potential variations in layer thickness and curing behavior (Figure 7d).
- *Pinholes and Cuts* occurred when a void formed around the print and can take the form of a hole, ridge or slit that extends from one side of the part to another (Formlabs Inc 2023). (Figure 7b and 7e).
- *Poor Surface Quality and Warping:* SLA-printed surfaces can exhibit roughness and layering artifacts, (Figure 7e). Samples fabricated with these defects may need post-processing to achieve a smooth finish in wood polymer composites (Figure 7c).
- *Delamination:* Layer-by-layer deposition in SLA can result in poor adhesion between the printed layers of wood-polymer composite, leading to delamination issues. This is related to increased viscosity of the resin and layer thickness (Formlabs Inc 2023).

The data showed that as the wood flour content increased the success of sample fabrication decreased for both sample types. This directly impacts printability and could be attributed to a few factors that will now be discussed.

Tensile performance

Tensile strength for each sample was identified by locating the peak stress value on the stress-strain graph. Young's modulus

was calculated by analyzing the linear segment within the designated strain interval on the same curve in the range of 0–0.2. The tensile stress and the Young's modulus for each composite were obtained from the average of five samples (Figures 8 and 9). Tensile strength of WPC1 (the control) was 22.1 MPa, and increased by 2 % to 23.1 MPa with the addition of 2.5 wt.% of wood flour, while Young's modulus decreased from 860.1 MPa to 842 MPa with the same level of wood flour addition. Tensile strength increased 8% with the addition of another 2.5 wt. % of wood flour in WPC3 coupled with an increase in Young's modulus to 895 MPa.

Further additions of wood flour resulted in decreasing tensile strength, WPC4 and WPC5 showed similar tensile strengths of 21.1 and 21.2 MPa respectively. WPC6 (12.5 wt.%) showed a further reduction in tensile strength to 20.2 MPa, while Young's modulus decreased to 663.3 MPa. However, 15 wt.% wood flour (WPC7) was associated with another increase in Young's modulus, rising to 730 MPa, albeit with a decline in tensile strength to 19.7 MPa. The final successful wood flour ratio of 17.5 wt.% experienced further reduction in tensile strength to 17.2 MPa and a Young's modulus of 501.4 MPa. The tensile performance confirmed results found by Zhang et al. (2021) and Feng et al. (2018) that low levels of wood flour can reinforce SLA fabricated polymer composites (Zhang et al. 2021). The result also shows that continuous increase in wood flour content will reduce tensile strength and Young's modulus of wood polymer composites. The moderate rise in tensile strength and Young's modulus at low levels of wood flour addition suggests that the composites have high stiffness and are resistant to (elastic) deformation when subjected to load. The tensile performance of SLA-printed WPCs was comparable to those manufactured through traditional methods, such as extrusion or compression molding (Nukala et al. 2022). Uniform distribution and alignment of wood fibers within the polymer matrix are critical for maximizing tensile strength. Ensuring fibers are well-aligned along the load direction can significantly enhance the tensile properties of WPCs.

Compression performance

The ultimate compressive strength was calculated using the equation:

$$F = P / A \quad (1)$$

where (F) is the compressive strength of the specimen in megapascals, (P) is the maximum applied load in newtons, and (A) is the cross-sectional area measured in square millimeters.

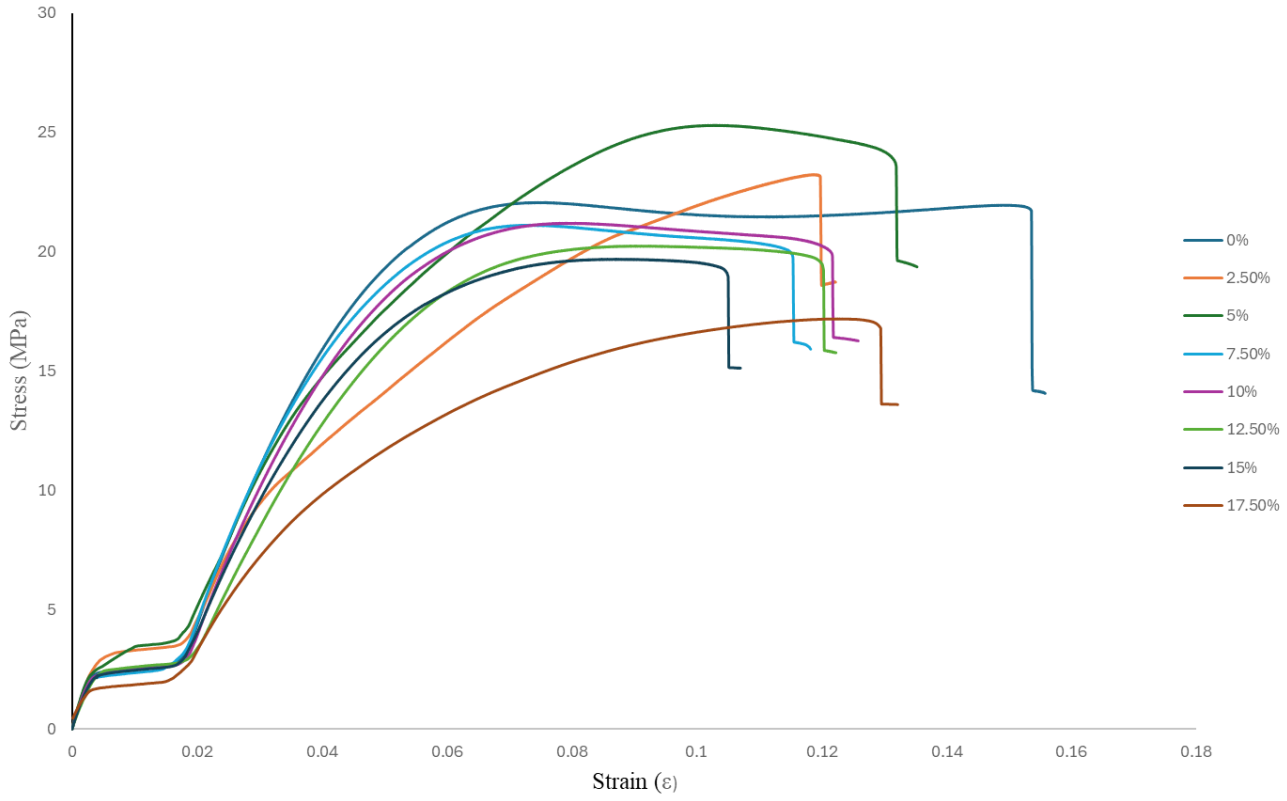

Figure 8. Examples of stress/strain plots for samples as wood flour levels increased from 0 to 17.5 wt.%.

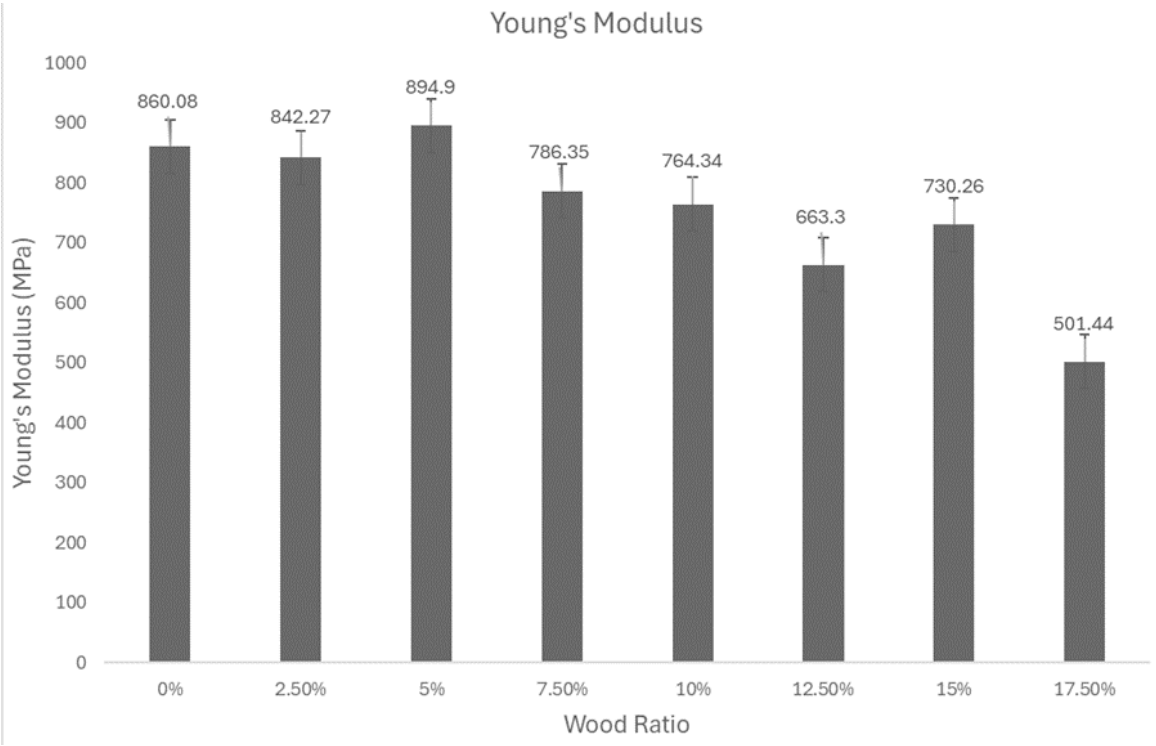

Figure 9. Effect of increasing amounts of wood flour from 0 to 17.5 % on Young's Modulus. Error bars represent one standard deviation.

WPC1 had a compressive strength of 22.3 MPa, WPC 2 was 29.8 MPa, and WPC3 increased significantly to 75.6 MPa. The increased compressive strength could be because of strain hardening, where a material becomes stronger and harder as it undergoes plastic deformation. Microstructural changes such as phase transformation or grain refinement were also likely to have occurred. WPC4 and WPC5 both experienced reduced compressive strengths, while WPC6 showed an uptick in strength to 29.3 MPa.WPC7 returned to trend with a reduction to 22.4 MPa and compressive strength of WPC8 was 15.8 MPa which was the lowest value recorded. This sample also had liquid resin within the internal structure upon fracture after extensive loading, showing signs of incomplete internal curing.

Wood flour addition was associated with increased stiffness and rigidity in the composites as evidenced by the increased elastic modulus (Table 2). WPC 2–7 showed an increase in elastic modulus, with WPC3 being the highest recorded at 320.8 MPa. These levels would make them suitable for applications where stiffness is desired such as bridge construction and furniture. The following samples showed an increase in compressive strength compared to the control at 2.5 wt.%, 5 wt.% 7 wt.% 12.5 wt.% and 15wt.%. All of the treatments except WPC5 and WPC8 experienced increased tensile strength. Increased compressive strength showed that the materials had good load bearing capacity and could maintain their shape under substantial compressive force. The wood flour amended WPCs

Table 2. Effect of wood concentration on tensile and compression strength of a 3D printed composite.

Wood Content (wt.%, nominal)	Tensile Strength (MPa)	Compressive Strength (MPa)	Compressive Strain (mm/mm)	Elastic Modulus (MPa)
0.0	22.1 ± 0.60	22.3 ± 5.31	24.8 ± 0.49	215.0 ± 21.93
2.5	23.2 ± 1.38	29.8 ± 0.01	25.8 ± 0.22	282.1 ± 25.52
5.0	25.3 ± 2.86	75.6 ± 32.38	25.8 ± 0.22	320.8 ± 52.88
7.5	21.2 ± 0.04	23.5 ± 4.46	26.1 ± 0.43	264.3 ± 12.93
10.0	21.1 ± 0.11	20.4 ± 6.65	26.0 ± 0.36	289.7 ± 30.89
12.5	20.2 ± 0.74	29.3 ± 0.36	25.4 ± 0.06	244.9 ± 0.78
15.0	19.7 ± 1.10	22.4 ± 5.24	24.8 ± 0.49	216.0 ± 21.22
17.5	17.2 ± 2.86	15.2 ± 10.33	25.2 ± 0.21	135.3 ± 78.28

Values represent means of 7 to 10 replicates while +/- figures represent one standard deviation.

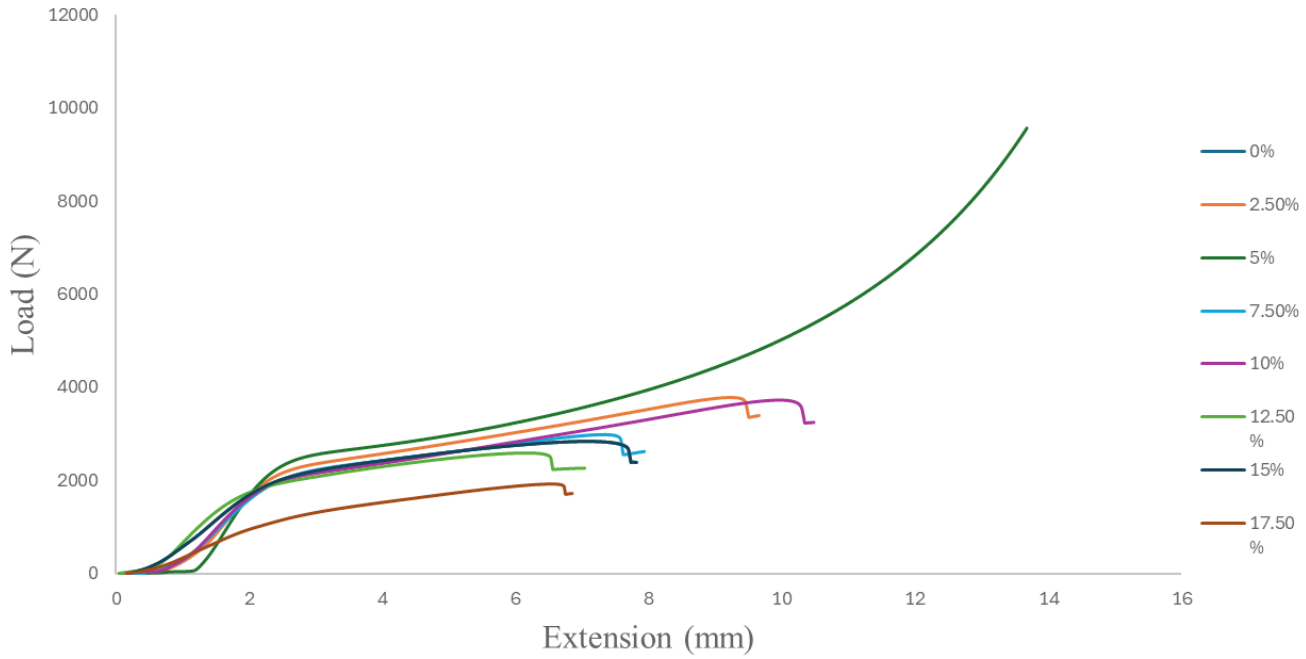

Figure 10. Compressive behavior of WPC with increased wood content.

exhibited superior compressive strength and stiffness compared to epoxy polymer at certain ratios (Figure 10). Strong interfacial bonding ensured efficient stress transfer from the matrix to the fibers, maximizing composite strength.

Conclusions

This study demonstrated printability and mechanical properties of WPC manufactured using stereolithography at wood content levels higher than 10%. Tensile and compressive mechanical tests were performed using printed WPC samples. The following statements summarize the main findings from the current study.

1. A limit of 17.5 wt.% wood flour content was determined to be the peak for the WPC using stereolithography when considering wood species, particle shape and size, density, resin viscosity and 3D printing capability.
2. Addition of 2.5 and 5.0 wt.% of wood flour increased the tensile strength of the composite before both properties declined with increasing wood flour content. WPCs exhibited enhanced tensile strength and stiffness due to the uniform dispersion of wood fibers within the polymer matrix and the ability to control layer-by-layer construction.
3. Young's modulus of the tensile samples increased at low wood flour ratios signifying reinforcement then decreased with increased wood content. A slight increase was observed at 15.0 wt.% before further reductions were noted at 17.5wt. %. Material stiffness was improved with 2.5 wt.% and 7.5 wt.% of wood flour, showing increased resistance to deformation and stiffness at those ratios.
4. Compressive strength increased at every ratio except 10 wt.% and 17.5 wt.%, indicating that the material had good load bearing capacity and could maintain its shape under substantial compressive forces. Elastic modulus also increased at all ratios except 17.5wt.%, indicating an increase in stiffness and rigidity when wood flour was used to reinforce epoxy polymer.

Applications of SLA printed WPCs are diverse and span across various industries, from consumer products to advanced industrial components. Enhancing this method opens new opportunities for innovative and sustainable manufacturing solutions. Future research may focus on the printability of WPC using biodegradable resin as an alternative to petroleum-based feedstocks, the impact of particle size on printability and mechanical properties, and the dimensional accuracy of different print orientations.

References

Anish MC, Pandey KK, Kumar R (2023) Transparent wood composite prepared from two commercially important tropical timber species. Sci Rep 13(1). https://doi.org/10.1038/s41598-023-42242-7

Baley C (2002) Analysis of the flax fibres tensile behaviour and analysis of the tensile stiffness increase. Compos Part A Appl Sci Manuf 33(7):939–948. https://doi.org/10.1016/S1359-835X(02)00040-4

Bártolo PJ (2011) Stereolithography. Springer US. https://doi.org/10.1007/978-0-387-92904-0

Berger MJ, Stark NM (1997) Investigations of species effects in an injection-molding-grade, wood-filled polypropylene. *In*: Proceedings of the Fourth International Conference on Wood Fiber-Plastic Composites, 12–14 May; Madison, WI. pp. 19–25.

Bledzki A (1999) Composites reinforced with cellulose-based fibres. Prog Polym Sci 24(2):221–274. https://doi.org/10.1016/S0079-6700(98)00018-5

Bledzki AK, Letman M, Viksne A, Rence L (2005) A comparison of compounding processes and wood type for wood fibre-PP composites. Compos Part A Appl Sci Manuf 36(6):789–797. https://doi.org/10.1016/j.compositesa.2004.10.029

Chan CM, Vandi LJ, Pratt S, Halley P, Richardson D, Werker A, Laycock B (2018) Composites of wood and biodegradable thermoplastics: a review. Polym Rev 58(3):444–494. https://doi.org/10.1080/15583724.2017.1380039

Chaudemanche S, Perrot A, Pimbert S, Lecompte T, Faure F (2018) Properties of an industrial extruded HDPE-WPC: the effect of the size distribution of wood flour particles. Constr Build Mater 162:543–552. https://doi.org/10.1016/j.conbuildmat.2017.12.061

Clemons C (2008) Raw materials for wood-polymer composites.

Clemons CM, Caulfield DF (2005) Wood flour. *In*: Functional Fillers for Plastics. Wiley. pp. 249–270. https://doi.org/10.1002/3527605096.ch15

Dizon JRC, Gache CCL, Cascolan HMS, Cancino LT, Advincula RC (2021) Post-processing of 3D-printed polymers. Technologies 9(3). https://doi.org/10.3390/technologies9030061

Faruk O, Bledzki AK, Fink HP, Sain M (2012) Biocomposites reinforced with natural fibers: 2000-2010. Prog Polym Sci 37(11):1552–1596. https://doi.org/10.1016/j.progpolymsci.2012.04.003

Feng C, Li Z, Wang H (2018) The effect of epoxy resin on wood-plastic composites. Pigm Resin Technol 47(5):369–376.

Formlabs Inc. (2023) Diagnosing a print failure (SLA). https://support.formlabs.com/s/article/Diagnosing-a-print-failure?language=en_US

Fu H, Dun M, Wang H, Zou C, Wang L, Zhou Z, Wang W, Xie Y, Wang Q (2022) Characterization of the structural rheological properties of wood flour-polyethylene composites with ultrahigh filling on the basis of uniaxial cyclic compression method. Compos Part A Appl Sci Manuf 153. https://doi.org/10.1016/j.compositesa.2021.106724

Gardner DJ, Han Y, Wang L (2015) Wood-plastic composite technology. Curr For Rep 1(3):139–150. https://doi.org/10.1007/s40725-015-0016-6

Huang Y, Löschke S, Proust G (2021) In the mix: the effect of wood composition on the 3D printability and mechanical performance of wood-plastic composites. Compos Part C Open Access 5. https://doi.org/10.1016/j.jcomc.2021.100140

Jian B, Mohrmann S, Li H, Li Y, Ashraf M, Zhou J, Zheng X (2022) A review on flexural properties of wood-plastic composites. Polymers 14(19). https://doi.org/10.3390/polym14193942

Kariz M, Sernek M, Obućina M, Kuzman MK (2018) Effect of wood content in FDM filament on properties of 3D printed parts. Mater Today Commun 14:135–140. https://doi.org/10.1016/j.mtcomm.2017.12.016

Khan MZR, Srivastava SK, Gupta MK (2020) A state-of-the-art review on particulate wood polymer composites: processing, properties and applications. Polym Test 89. https://doi.org/10.1016/j.polymertesting.2020.106721

Krapež Tomec D, Kariž M (2022) Use of wood in additive manufacturing: review and future prospects. Polymers 14(6). https://doi.org/10.3390/polym14061174

Matuana LM, Stark NM (2015) The use of wood fibers as reinforcements in composites. *In*: Biofiber Reinforcements in Composite Materials. Elsevier Inc. p. 648–688. https://doi.org/10.1533/9781782421276.5.648

Mazzanti V, Mollica F (2020) A review of wood polymer composites rheology and its implications for processing. Polymers 12(10):2304. https://doi.org/10.3390/polym12102304

Mohammadizadeh M, Fidan I (2021) Tensile performance of 3D-printed continuous fiber-reinforced nylon composites. J Manuf Mater Process 5(3). https://doi.org/10.3390/jmmp5030068

Nachtigall SMB, Cerveira GS, Rosa SML (2007) New polymeric-coupling agent for polypropylene/wood-flour composites. Polym Test 26(5):619–628. https://doi.org/10.1016/j.polymertesting.2007.03.007

Nukala SG, Kong I, Kakarla AB, Tshai KY, Kong W (2022) Preparation and characterisation of wood polymer composites using sustainable raw materials. Polymers 14(15):3183. https://doi.org/10.3390/polym14153183

Oksman K, Skrifvars M, Selin JF (2003) Natural fibres as reinforcement in polylactic acid (PLA) composites. Compos Sci Technol 63(9):1317–1324. https://doi.org/10.1016/S0266-3538(03)00103-9

Peltola H, Pääkkönen E, Jetsu P, Heinemann S (2014) Wood based PLA and PP composites: effect of fibre type and matrix polymer on fibre morphology, dispersion and composite properties. Compos Part A Appl Sci Manuf 61:13–22. https://doi.org/10.1016/j.compositesa.2014.02.002

Pokhrel G, Gardner DJ, Han Y (2021) Properties of wood-plastic composites manufactured from two different wood feedstocks: wood flour and wood pellets. Polymers 13(16). https://doi.org/10.3390/polym13162769

Pringle AM, Rudnicki M, Pearce J, Wood JP, Pearce JM (2017) Furniture waste-based recycled 3D printing filament. For Prod J 68(1):10. https://doi.org/10.13073/FPJ-D-17-00042

Schmidleithner C, Kalaskar DM (2018) Stereolithography. In: 3D Printing. InTech. https://doi.org/10.5772/intechopen.78147

Schricker SR (2017) Composite resin polymerization and relevant parameters. In: Orthodontic Applications of Biomaterials. Elsevier. pp. 153–170. https://doi.org/10.1016/B978-0-08-100383-1.00009-6

Schwarzkopf MJ, Burnard MD (2016) Wood-plastic composites—performance and environmental impacts. *In*: Environmental Footprints and Eco-Design of Products and Processes. Springer. pp. 19–43. https://doi.org/10.1007/978-981-10-0655-5_2

Shi Q, Yu K, Kuang X, Mu X, Dunn CK, Dunn ML, Wang T, Qi HJ (2017) Recyclable 3D printing of vitrimer epoxy. Mater Horiz 4(4):598–607. https://doi.org/10.1039/c7mh00043j

Sommerhuber PF, Wenker JL, Rüter S, Krause A (2017) Life cycle assessment of wood-plastic composites: analysing alternative materials and identifying an environmentally sound end-of-life option. Resour Conserv Recycl 117:235–248. https://doi.org/10.1016/j.resconrec.2016.10.012

Sutton JT, Rajan K, Harper DP, Chmely SC (2018) Lignin-containing photoactive resins for 3D printing by stereolithography. ACS Appl Mater Interfaces 10(42):36456–36463. https://doi.org/10.1021/acsami.8b13031

Tanaka T, Ito H (2013) Manufacturing and processing methods of biocomposites. *In*: Polymer Composites. Wiley. pp. 179–211. https://doi.org/10.1002/9783527674220.ch5

van Voorn B, Smit HHG, Sinke RJ, de Klerk B (2001) Natural fibre reinforced sheet moulding compound. Compos Part A Appl Sci Manuf 32(9):1271-1279. https://doi.org/10.1016/S1359-835X(01)00085-9

Vidakis N, Petousis M, Michailidis N, Kechagias JD, Mountakis N, Argyros A, Boura O, Grammatikos S (2022) High-performance medical-grade resin radically reinforced with cellulose nanofibers for 3D printing. J Mech Behav Biomed Mater 134:105408. https://doi.org/10.1016/j.jmbbm.2022.105408

Wang X, Jiang M, Zhou Z, Gou J, Hui D (2017) 3D printing of polymer matrix composites: a review and prospective. Compos Part B Eng 110:442–458.

https://doi.org/10.1016/j.compositesb.2016.11.034

Yang TH, Leu SY, Yang TH, Lo SF (2012) Optimized material composition to improve the physical and mechanical properties of extruded wood-plastic composites (WPCs). Constr Build Mater 29:120-127. https://doi.org/10.1016/j.conbuildmat.2011.09.013

Yao J, Hakkarainen M (2023) Methacrylated wood flour-reinforced "all-wood" derived resin for digital light processing (DLP) 3D printing. Compos Commun 38. https://doi.org/10.1016/j.coco.2023.101506

Youngquist JA, Myers GE, Muehl JH, Krzysik AM, Clemens CM (1994) Project summary: composites from recycled wood and plastics.

Zhang S, Bhagia S, Li M, Meng X, Ragauskas AJ (2021) Wood-reinforced composites by stereolithography with the stress whitening behavior. Mater Des 206. https://doi.org/10.1016/j.matdes.2021.109773

Zhang S, Li M, Hao N, Ragauskas AJ (2019) Stereolithography 3D printing of lignin-reinforced composites with enhanced mechanical properties. ACS Omega 4(23):20197–20204. https://doi.org/10.1021/acsomega.9b02455

Time-temperature effects on early-stage primary thermal creep of plywood and oriented strand board (OSB) at elevated temperatures

Byrne T. Miyamoto†
Structural Testing Coordinator
TallWood Design Institute
Oregon State University
Email: byrne.miyamoto@oregonstate.edu

*Arijit Sinha**†
Professor and JELD-WEN Chair
Department of Wood Science and Engineering
Oregon State University, Corvallis, OR 97331
Email: Arijit.sinha@oregonstate.edu

(Received 2 February 2025)

Abstract. This study examined the effects of elevated temperatures on plywood and Oriented Strand Board (OSB) subjected to a constant load. Due to the short duration and the absence of a steady-state, this behavior was classified as "Early-Stage Primary Thermal Creep." Deflections at each elevated temperature, ranging from 120°C to 200°C, were analyzed to assess the thermal effects. Statistical analysis of the maximum deflections indicated the onset of thermal degradation at around 170°C for both plywood and OSB. Notably, a significant increase in deflection was observed between 180°C and 190°C for OSB, suggesting adhesive thermal decay. In addition to the statistical analysis, a numerical model was fitted to the experimental data to create temperature-dependent deflection curves, revealing an exponential trend. To understand the combined effects of temperature and time on early-stage primary thermal creep, two models were evaluated: a modified rational function model and a modified power model. The temperature-dependent power-exponential creep model provided a superior fit for both plywood and OSB, as indicated by higher R^2 values and lower root mean square errors.

Keywords: Wood sheathing, Primary creep, Elevated temperatures, Power Law Model, Thermal degradation

Introduction

According to the U.S. Fire Administration (2021), an estimated average of 230,500 fires occur annually in one-family and two-family residential buildings. Ensuring structural stability during a fire is critical to allow occupants sufficient time for safe egress. Therefore, building materials must be able to withstand not only the direct impact of fire but also the elevated temperatures associated with such events. Fires within a house typically progress through several stages before fully engulfing a structure. Once fully developed, temperatures within a room can reach up to 1200°C (Kerber 2012). In order to prevent flame spreading to flammable building materials, such as sheathing materials like plywood and OSB, fire-resistant materials, such as drywall and gypsum board, as well as insulation, are often installed over or around these vulnerable components.

When exposed to extreme temperatures, such as in the case of a fully developed fire, even if shielded from direct flames, sheathing materials like plywood and OSB can be affected by elevated temperatures. Understanding how these materials behave under such conditions is critical, as these sheathing materials are designed to provide structural support by distributing loads from floors and joists to the foundation. For example, in wall systems, the sheathing covers framing members and transfers loads to the wall studs, playing a key role in maintaining the overall stability of the structure (APA 2020).

The thermal degradation of wood products has been extensively studied due to wood's inherent flammability. Two key factors influencing this degradation are temperature severity and exposure duration. Research indicates that the breakdown of wood compounds begins at temperatures between 80°C and

* Corresponding author
† Society of Wood Science & Technology member

150°C (Sebio-Puñal et al. 2012; Paál et al. 2023). Additionally, prolonged exposure to lower temperatures (65**°C** to 70**°C**) can lead to significant deterioration of wood properties over 1 to 3 years in both untreated and fire-retardant-treated lumber and clear wood (Green et al. 2003; Lebow and Winandy 1999). Studies on plywood at lower elevated temperatures reveal similar degradation patterns, with both untreated and fire-retardant-treated specimens showing mechanical property loss when exposed to temperatures between 54°C and 77°C over 140 days (Winandy et al. 1991).

For solid sawn lumber, both temperature and exposure time have been widely investigated and are accounted for in building codes and guidelines. For example, the National Design Specification (NDS) includes a temperature effect factor, Ct, for temperatures between 38°C and 67°C. This factor helps engineers determine potential strength losses in lumber when designing structures exposed to elevated temperatures. However, there is a lack of comprehensive studies on the combined effects of temperature severity and exposure time on plywood and OSB, particularly when these materials are subjected to constant loads, as they would be in real-world structural applications.

Research on the long-term effects of constant loading falls under the category of thermal creep studies, which focus on how materials deform over time under constant stress. Studies examining the effects of temperature exposure typically analyze the loss of strength in materials after being subjected to various temperature conditions. However, the intersection of these two areas, prolonged loading (creep) and temperature-induced strength degradation, has been relatively unexplored for plywood and OSB. While some research has examined these effects on wood-plastic composites, comprehensive studies specifically addressing plywood and OSB under these conditions remain limited (Wei and Zhao 2023; Chang et al. 2014).

The strength of wood and wood-based composites decreases as temperature increases, a behavior well-documented in numerous studies examining both the fire performance of wood and its properties at elevated temperatures without direct flame exposure (Sinha et al. 2011; Sinha 2013, 2009; Rammer et al. 2018; Kuronen et al. 2021). Wood products used in structural applications require a fire rating, indicating the duration a product can withstand fire before reaching a set failure criterion (American Wood Council 2021). Research on plywood and OSB at elevated temperatures typically examine both the immediate and residual effects on strength (Miyamoto et al. 2024). These studies often assess strength properties, such as flexural performance, comparing the modulus of elasticity (MOE) and modulus of rupture (MOR). Findings suggest that elevated temperatures have a more significant impact on MOR than on MOE (Sinha et al. 2011; Zhong et al 2015).

Creep behavior, which is critical to understanding long-term material performance, occurs when a material is subjected to a constant load over time. This process can be broken down into three distinct phases: primary, secondary, and tertiary (Granello and Palemo 2019). The primary creep phase occurs immediately after load application, characterized by a relatively high rate of deformation that gradually decreases as the material adapts to the applied stress (Madsen 1992). The secondary creep phase follows, marked by a steady, low creep rate that forms a plateau and represents an equilibrium state. Finally, the tertiary creep phase begins when the material's structural integrity starts to deteriorate under sustained loading, leading to a rapid acceleration of deformation and eventual failure (Granello and Palemo 2019). Accurately modeling these phases, especially with temperature effects, is essential for predicting the long-term safety and performance of plywood and OSB in structural applications.

In this study, the authors investigate the effects of time and temperature on the creep behavior of plywood and OSB under a constant load to better understand their mechanical response to thermal stress. Due to the short loading duration, the full creep behavior could not be observed, and it is likely that the materials did not reach the complete primary creep phase. Therefore, the observed behavior is referred to as " Early-Stage Primary Thermal Creep." This term describes the stage where the material is subjected to a load sufficient to begin primary creep, but unloading occurs while the initial creep rate remains high, without reaching a steady-state plateau.

To simulate the behavior of these materials in a protected system during a fire scenario, they were exposed to elevated temperatures ranging from 120°C to 200°C. The objectives of this study were to:

- Compare the maximum Early-Stage Primary Thermal Creep deflections of plywood and OSB after 50 minutes of exposure to elevated temperatures,
- Analyze and compare the Early-Stage Primary Thermal Creep behavior of plywood and OSB as a function of time and temperature,
- Compare two common creep models used for wood products to predict the effects of time and temperature on these materials.

Materials

Two wood composites, oriented strand board (OSB) and plywood, were selected for testing under elevated temperatures in an environmental chamber. Both OSB and plywood are among the most commonly used sheathing materials in the United States, and the selected thicknesses represent typical sheathing dimensions (International Code Council 2018). Samples were prepared from 11.1 mm-thick Aspen OSB structural sheathing classified as Exposure 1 and 12.7 mm-thick Douglas-fir CDX plywood structural sheathing. A total of 56 specimens were prepared for each composite type, with each specimen measuring 50.8 mm in width and 508 mm in length. Prior to testing, the specimens were conditioned to approximately 10% to 12% moisture content (MC) in a controlled environment at 65% relative humidity (RH) and 20°C for four weeks.

Methods

Testing procedure

Specimens were tested at 10 different temperatures, with 25°C serving as the control and the remaining temperatures ranging from 120°C to 200°C in 10°C increments. Both plywood and OSB specimens were randomly selected for testing to ensure unbiased sampling. Additionally, six specimens of each material underwent three-point bending tests to determine the peak deflection at failure and the proportional limit. The peak deflection at failure provided a baseline for comparing creep deflections, and the proportional limit was used to define the constant load applied during testing. As shown in Figure 1, load-deflection curves for plywood and OSB illustrate the process of identifying the proportional limit. Fifty percent of the proportional limit was selected to establish the constant load applied to the specimens.

Prior to testing, the specimens were pre-heated in an oven. Two specimens were placed in the oven, one as the test specimen and the other as the thermocouple specimen. The thermocouple specimen was equipped with two thermocouples, one positioned at the center and another near the surface, to monitor the temperature, as shown in Figure 2C. Once the test specimens reached the target temperature, they were removed from the oven for testing.

Testing was conducted using a BEMCO environmental chamber integrated within an INSTRON 5589 testing frame, as shown in Figure 2A. The chamber featured openings for both the testing base (bottom) and load head (top). The test supports had a 457 mm span for the specimen and a secondary support for the thermocouple, as illustrated in Figure 2B. A 5 kN load cell was connected to a loading extension arm, allowing it to extend into the chamber without damaging any electrical components due to temperature. A high-temperature Linear Variable Differential Transformer (LVDT) was used to record the center deflection. The specimen was loaded in a 3-point bending configuration as shown in Figure 2B.

The testing procedure was comprised of three phases: loading, holding, and unloading. The entire loading protocol, including all phases, is illustrated in Figure 3, with red lines marking

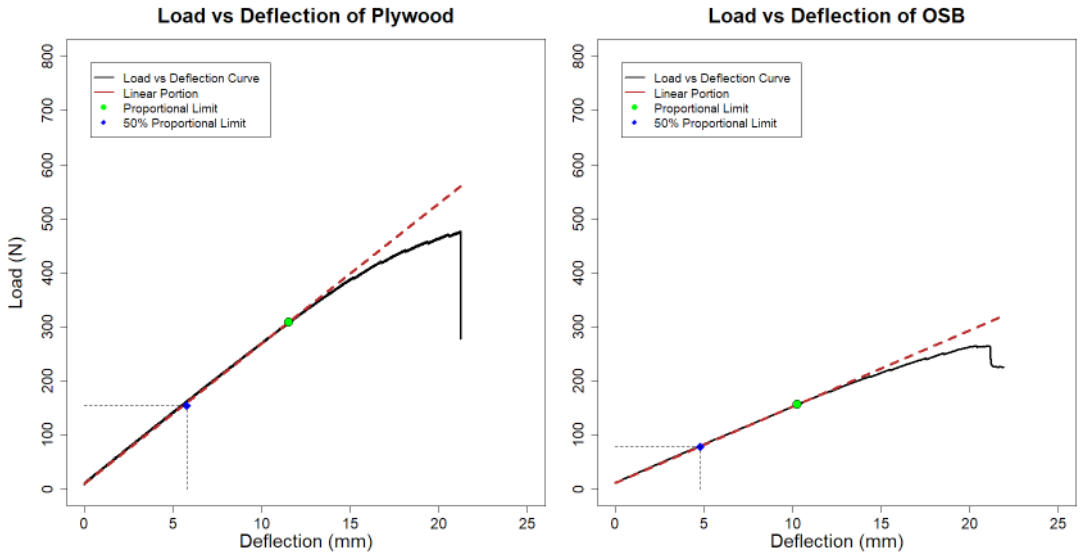

Figure 1. Load Deflection curves of OSB and Plywood Bending tests to determine the applied constant load.

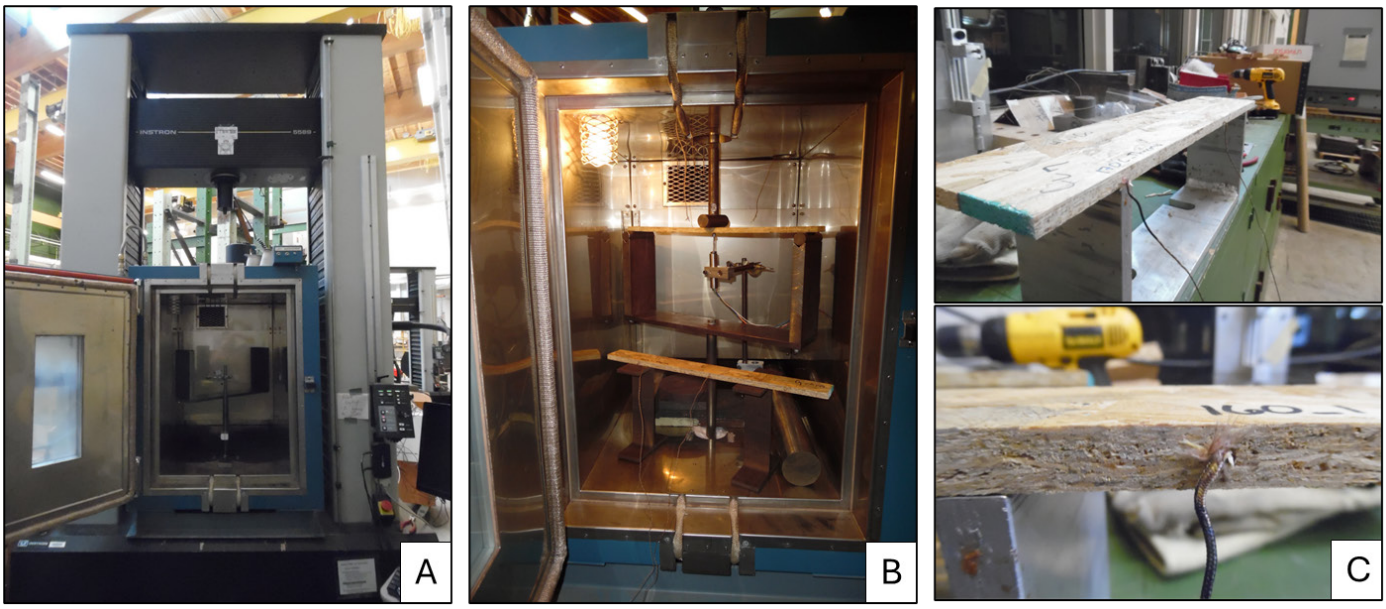

Figure 2. (A) BEMCO chamber installed within Instron 5589 Testing Frame, (B) Test setup with both testing and thermal couple specimens installed, and (C) Top: Thermal couple specimen with both thermocouples installed, Bottom: close up of installed thermocouple.

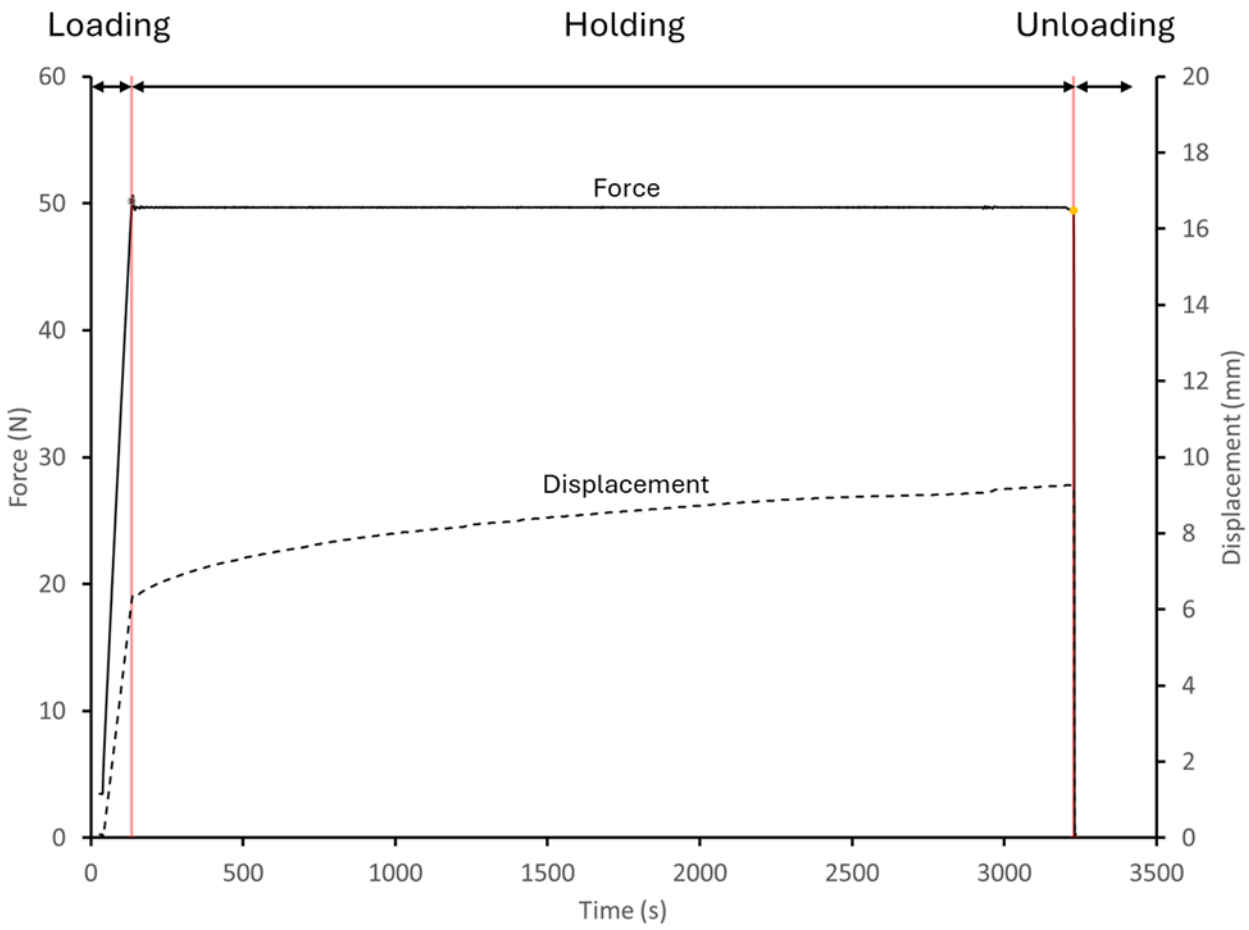

Figure 3. Testing procedure depicting applied force, and recoded displacement.

each phase. During the loading phase, the load head applied force at a rate of 6 mm/min to the center of the specimen until the target loads of 50 N for OSB and 160 N for plywood were reached, as shown in Figure 1. The time required to reach the target force ranged from 40 to 80 seconds for both plywood and OSB.

Following the initial loading, the specimen entered the holding phase, during which the load was maintained for 3,000 seconds. This duration was based on findings from a study by Kerber (2012), which investigated structural collapse times and firefighter response during house fires. The study reported that protected floor systems (e.g., gypsum board, plaster, or lath) experienced collapse times ranging from 26 to 79 minutes, while unprotected floor systems could fail as early as 18 minutes. A duration of 50 minutes was chosen for this experiment as a midpoint within the range of protected system collapse times.

After the holding phase, the specimens were unloaded and removed, along with the thermocouple specimen. To ensure the analysis focused on the creep behavior for both material, specimens that had failed before completing the holding phase were excluded from the data. By analyzing only specimens that sustained the entire loading protocol, the study provides a more accurate representation of the early stage primary creep. During testing, force (N), displacement (mm), time (s), and temperature (°C) were recorded at a frequency of 1 Hz.

To isolate material behavior during the holding phase, the initial deflection at the prescribed load for both materials was recorded and subtracted from the total deflection data for each specimen. The resulting value, referred to as creep deflection, is calculated using the formula in Equation 1.

$$D_{cr} = D_t - D_i \tag{1}$$

Where, D_{cr} is the creep deflection, D_t is the deflection at a given time, and D_i is the initial deflection after loading. Additionally, the time was adjusted to represent the starting point at the zero-deflection mark.

Statistical analysis

A statistical analysis was conducted to evaluate differences in maximum creep deflections across the tested temperatures for both plywood and OSB. The Fligner test ($\alpha = 0.05$) and the Shapiro-Wilk test ($\alpha = 0.05$) were used to assess the assumptions of equal variance and normality, respectively. A violation of the normality assumption was indicated by the Shapiro-Wilk test (p-value < 0.05), necessitating the use of the non-parametric Kruskal-Wallis test ($\alpha = 0.05$), which is more suitable for non-normally distributed data. When significant differences between temperatures were found, a post-hoc Kruskal multiple comparison test ($\alpha = 0.05$) was used to identify specific differences between individual temperatures.

Modeling

Three models were constructed to investigate the effects of temperature and time on the creep deflection properties of plywood and OSB. The first model utilized an analytical exponential approach, focusing only on the temperature effect on the two wood composites. This model followed a modified exponential equation that incorporated temperature (T) as the independent variable. The temperature-dependent deflection curve, following an exponential trend, was fitted using an equation derived from the study by Chang et al. (2023), which examined the creep behavior of wood-plastic composites at elevated temperatures. The equation is expressed as:

$$D_{cr}(T) = a * \exp\left({}^{T}/_{m}\right) + b \tag{2}$$

where T is the temperature in Celsius, and (a), (b), and (m) are parameters determined by fitting the model. The parameter (a) within the equation represented the scaling factor for deflection sensitivity to temperature, while parameter (m) represented the temperature scaling factor. Parameter (b) accounted for the baseline deflection, corresponding to the initial deflection observed at lower temperatures, including the control specimens.

The other two models, a rational function and a power model, were constructed to investigate the combined effects of temperature and time on the material's primary creep behavior. The rational function model, one of the earliest and simplest models, used to characterize polymers and food properties, was originally proposed by Peleg (1979) and later refined by Smulski (1987). This function is expressed as:

$$D_{cr} = \frac{t}{c + dt} \tag{3}$$

where Dcr represents the creep deflection, (t) is time in seconds, and (c) and (d) are constants. Smulski (1987) further rearranged the equation to enable linear regression by plotting t/Dcr against (t), facilitating the estimation of the constants (c) and (d) using the slope intercept form. The linearized equation is:

$$\frac{t}{D_{cr}} = c + dt \tag{4}$$

To incorporate the effect of temperature, linear relationships between the parameters (c) and (d) with temperature were introduced. These linear regressions were incorporated into the model, resulting in the function expressed as:

$$D_{cr}(t,T) = \frac{t}{(eT+f)+(gT+j)t} = \frac{1}{gT+j+\frac{eT+f}{t}} \quad (5)$$

In this equation, (c) was replaced with (eT+f) and (d) with (gT+j), reflecting the temperature dependency of these parameters. Where *t* is time in seconds, *T* is temperature in Celsius, and (*e)* and (*g)* are coefficients while *(f)* and *(j)* are constants. Both *(e)* and *(g)* are negative coefficients, with *(e)* representing the rate of change in the initial stiffness at a given temperature, and *(g)* indicating the creep rate at that temperature. The constant *(f)* characterizes the baseline creep resistance at 0°C, representing the resistance to creep when temperature effects are minimal, while *(j)* reflects the initial creep rate at 0°C, providing a baseline rate for the model.

The third model developed was the power law model or power model. This model is widely used to describe viscoelastic behavior in materials subjected to moderate loads. Both Chang et al. (2023) and Hoyle et al. (1985) used this model to determine the creed properties of wood products along with Clouser (1959), Moosavi (2016), and Hsieh and Chang (2018). The Power model is a simple model and has an exponential form, with the model shown below in equation 6:

$$D_{cr} = k * t^n \quad (6)$$

Where (*k)* is a coefficient of time-dependent displacement, (*t)* is time in seconds, and (*n)* is the exponential material constant. To incorporate the effect of temperature, the exponential function from the first model was integrated, resulting in the following combined equation:

$$D_{cr} = d * t^n * \exp\left(\frac{T}{m}\right) + j \quad (7)$$

All models were fitted to the experimental data using the Levenberg-Marquardt nonlinear algorithm in R (RStudio Team, 2023).

Results and discussion

Early-stage primary thermal creep deflection analysis

For all 100 specimens, the maximum deflections for plywood and OSB were 6.09 mm and 8.15 mm, respectively, both observed at 200°C. The average maximum creep deflection results are presented in Table 1.

Plywood exhibited lower deflections compared to the OSB tested specimens but demonstrated greater variability and a higher number of failures. For both materials, higher temperatures resulted in increased creep deflections over time. Failures in plywood occurred at three specific temperatures: 130°C, 180°C, and 200°C. At 130°C, a failure was observed after 1,300 seconds of loading, while at 180°C, failure occurred after 1,200 seconds. The two failures at 200°C happened within 1,000 seconds. Upon inspection, the specimen that failed at 130°C had an open knot near its center, whereas the others contained only minor, non-substantial defects. In contrast, OSB specimens exhibited higher deflections than plywood but showed lower variability and experienced only one failure. This failure occurred after maintaining a constant load for 1,900 seconds at 200°C. To illustrate the differences in creep deflections, the average deflection curves for each temperature were calculated and are presented in Figure 4.

A comparison of the average deflection curves for plywood and OSB reveals distinct differences in their creep behavior at each tested temperature. Plywood showed a gradual increase in creep deflection across the tested temperature range. However, OSB displayed a significant increase in creep deflection between 180°C and 190°C, where the maximum average deflection rose from 3.69 mm to 6.37 mm, nearly doubling. This pronounced increase in OSB's deflection can be attributed to differences in adhesives and wood species.

Plywood uses phenol-formaldehyde (PF) adhesive to bond the veneers, which begins to degrade around 250°C (Alonso et al. 2011, Huang et al. 2024). In contrast, OSB typically uses polymeric methylene diphenyl diisocyanate (PMDI) adhesive, which can start to degrade at approximately 185°C and above at prolonged exposure (Desai and O'Dell 1989; Yang et al. 1985). The degradation of the PMDI adhesive at these temperatures, combined with time-dependent creep behavior, likely explains the sharp deflection increase in OSB at elevated temperatures.

The results from the Kruskal multiple comparisons test are presented in Figure 5, with the fitted exponential equation (2) overlaid on the boxplots. In these boxplots, the letters above each box represent statistically significant differences between temperatures as determined by the Kruskal multiple comparisons test. Boxes labeled with the same letter(s) do not differ significantly. The red dashed line in each plot represents the fitted exponential equation, with its specific parameters incorporated and the R^2 values displayed at the top left corner of each plot.

For both plywood and OSB, the results indicate that temperatures above 170°C become significantly different from

Table 1. Table 1. Average maximum creep deflections for plywood and OSB.

Temp. (°C)	Plywood (mm)				OSB (mm)			
	Average	StaDev	COV (%)	N (#)	Average	StaDev	COV (%)	N (#)
*20	0.47	0.22	47%	5	0.45	0.15	34%	5
120	1.90	0.60	32%	5	1.28	0.50	39%	5
130	1.32	0.41	31%	4	1.71	0.82	48%	5
140	1.72	1.04	61%	5	1.59	0.53	33%	5
150	2.13	0.72	34%	5	1.79	0.63	35%	5
160	1.86	0.68	36%	5	1.90	0.89	47%	5
170	2.91	0.75	26%	5	2.98	0.66	22%	5
180	2.83	0.44	16%	4	3.69	0.90	24%	5
190	3.68	1.17	32%	5	6.37	1.30	20%	5
200	4.76	1.35	28%	3	7.57	0.49	6%	4
**Control	20.07	4.81	24%	6	21.49	3.75	17%	6

* Testing temperature was at room temperature, but categorized for plotting as 20.

** Specimens used for calculating the constant load, and used as a baseline for maximum deflection at peak load.

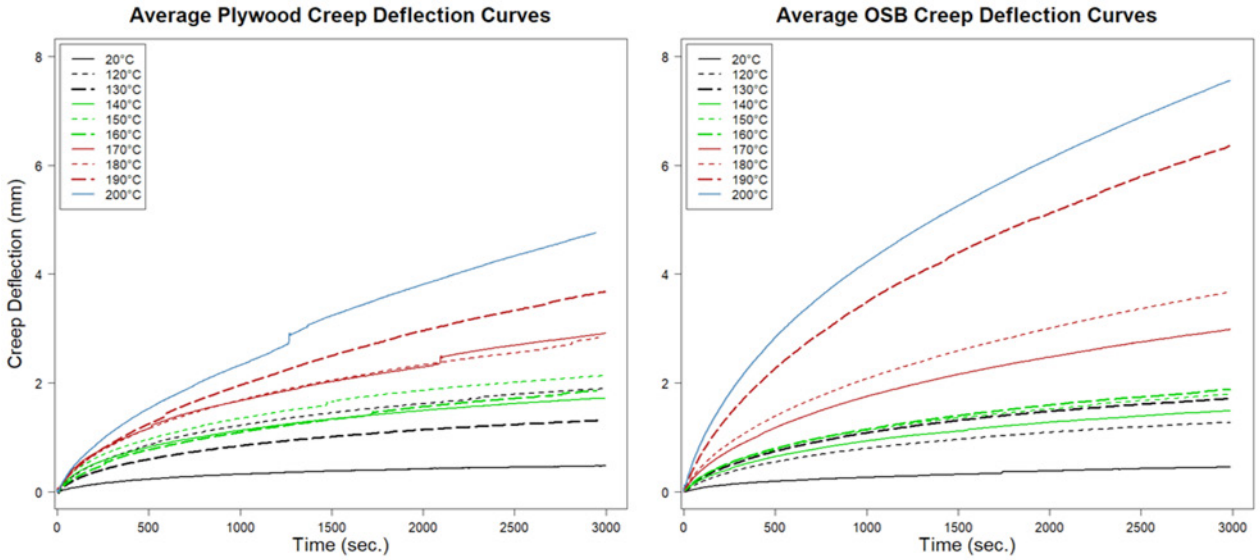

Figure 4. Average creep deflection curves for plywood and OSB at each temperature.

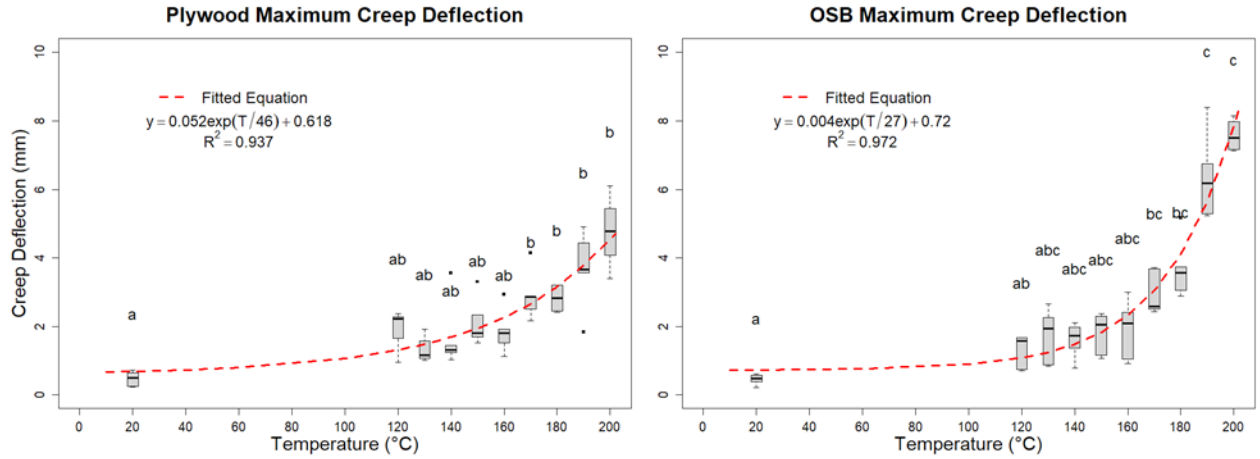

Figure 5. Boxplots for plywood (left) and OSB (right) of the creep defection indicating the results of the Kruskal multiple comparisons tests and a dashed line of the fitted equation 2.

the room temperature deflections. This aligns with findings by Miyamoto et al. (2024), who observed similar behavior in plywood, noting that temperatures around 170°C trigger chemical changes in wood. Around 150°C, wood extractives begin to decompose, and in dry conditions, lignin transitions from a hard, glassy state to a softer, rubbery state (Fengel and Wegnener 1989). As temperatures increase to approximately 180°C to 220°C, hemicellulose, the most thermally sensitive component of wood, begins to degrade (Dietenberger and Hasburgh 2016).

Because OSB is manufactured from Aspen, a hardwood with higher hemicellulose content than Douglas-fir, it shows greater deflection at elevated temperatures. The earlier degradation of the PMDI adhesive used in OSB further amplifies this deflection. Together, the combined effects of hemicellulose content and adhesive degradation explain the more pronounced creep behavior of OSB compared to plywood at high temperatures.

The exponential model provided a strong fit for both plywood and OSB data, with R^2 values of 0.937 and 0.972, respectively. These high R^2 values indicate that the exponential trend effectively captures the temperature-dependent creep behavior of both materials, demonstrating that the model used by Chang et al. (2023) is effective at predicting the initial primary thermal creep at elevated temperatures.

Effects of time and temperature on early-stage primary thermal creep

To understand and predict the early-stage primary thermal creep behavior of plywood and OSB at elevated temperatures, the rational function and power models were fitted to the data, represented by equations 3 and 6, respectively.

Temperature-dependent rational creep model

The rational function from equation 3 was rearranged to plot t/Dcr against (t) for each temperature, enabling a simple linear regression to fit the data into equation 4 and calculate the constants (c) and (d). An example of this process for plywood and OSB at 170°C is shown in Figure 6, with the calculated constants listed in Table 2.

A linear relationship between temperature and the constants (c) and (d) was identified from the values in Table 2. Simple linear regression was used to predict the values of (c) and (d) at each temperature, excluding 20°C, as it did not accurately represent the behavior of the material, as seen in Figure 7. The regression data for OSB showed stronger correlations, with R^2 values of 0.92 and 0.93, compared to plywood. The (c) constant for plywood exhibited a weaker correlation, indicated by an R^2 value of 0.48. These regression equations were incorporated into secondary regression formulas, resulting in the development of a second-order function (Equation 5).

Table 2. The calculated constant a and b for plywood and OSB.

Temperature (°C)	Plywood		OSB	
	*c	**d	*c	**d
20	1332.40	1.70	1845.00	1.69
120	378.96	0.42	604.81	0.61
130	534.72	0.60	435.46	0.45
140	380.08	0.47	510.24	0.52
150	335.01	0.37	412.50	0.44
160	465.64	0.40	415.47	0.41
170	294.09	0.26	293.56	0.25
180	297.67	0.27	258.58	0.20
190	305.91	0.18	164.63	0.11
200	266.13	0.13	129.25	0.10

* Initial creep resistance.
** Creep rate.

The function (Equation 5) was developed by incorporating the regression equations for (c) and (d) into the model. As shown in Figure 7, the regression equations for (c) are plotted in panels (I) and (II) for OSB and plywood, respectively, while the regression equations for (d) are presented in panels (III) and (IV) for the corresponding materials. These regression formulas were integrated into the model to form Equation 5, a temperature-dependent rational creep model. The combined effects of temperature and time on creep deflection are visualized in Figure 8 for both OSB and plywood. The fitted parameters, root mean square errors, and R^2 values are summarized in Table 3.

The temperature-dependent rational creep model was evaluated using statistical analysis of the Root Mean Square Error (RMSE) and R^2 values. The results indicated that the model demonstrated strong predictive potential for OSB, with an R^2 of 0.957, suggesting a high correlation between the model and the observed data. The relatively low RMSE of 0.347 for OSB indicates only a small deviation between the predicted and actual values. In contrast, the model's fit for plywood was less accurate, with an R^2 of 0.729, showing a moderate correlation. The RMSE for plywood was 0.501, indicating a higher level of prediction error. These results suggest that the temperature-dependent rational creep model is more suitable for predicting the behavior of OSB than plywood.

Temperature-dependent power-exponential creep model

The final model constructed was the power model (Equation 6), which was combined with the exponential function (Equation

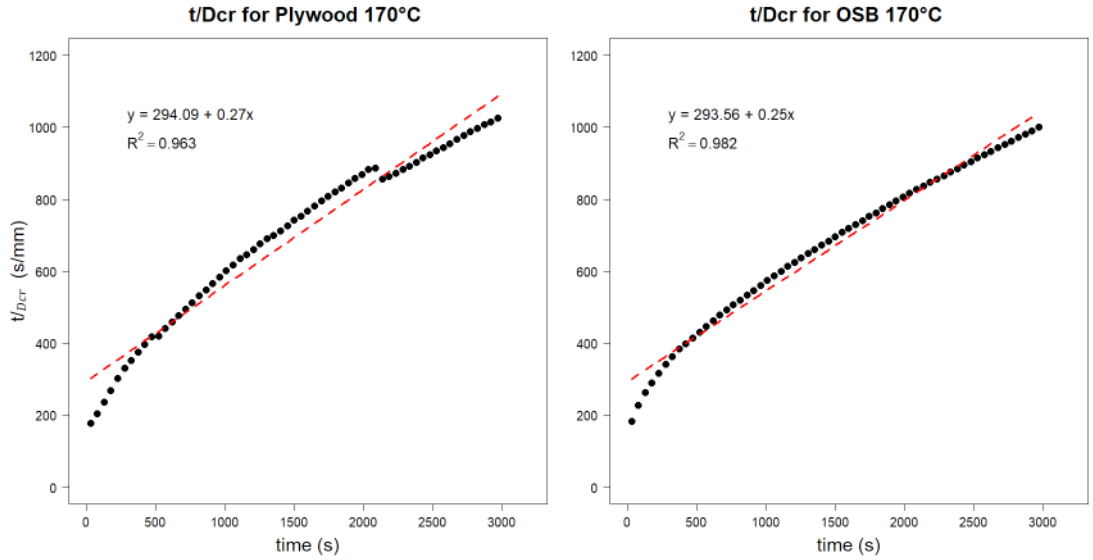

Figure 6. Example of the linear regression fit for the (time/deflection) vs time to obtain (c) and (d).

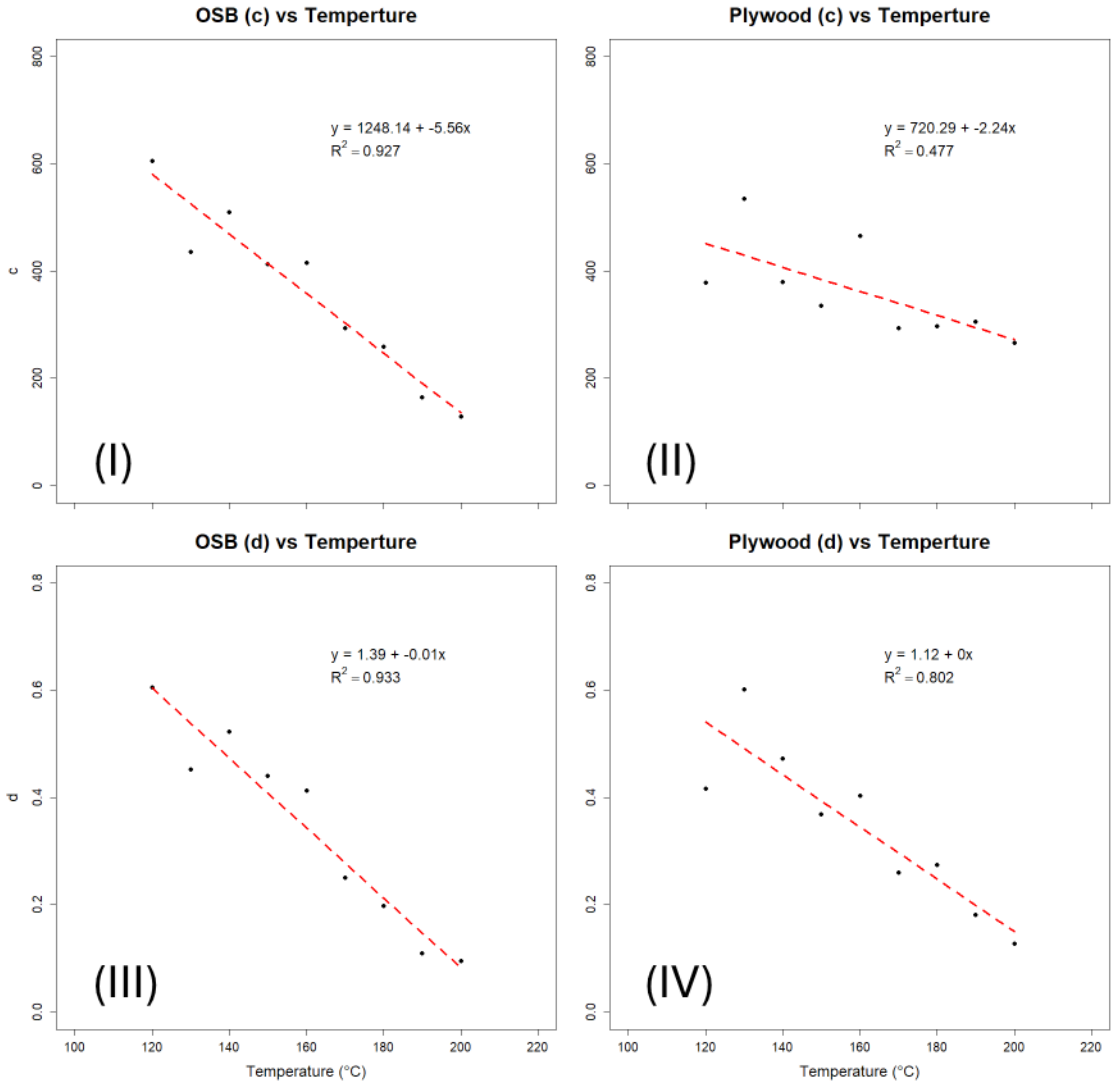

Figure 7. Calculate constants a and b plotted against temperature with a simple linear regression performed.

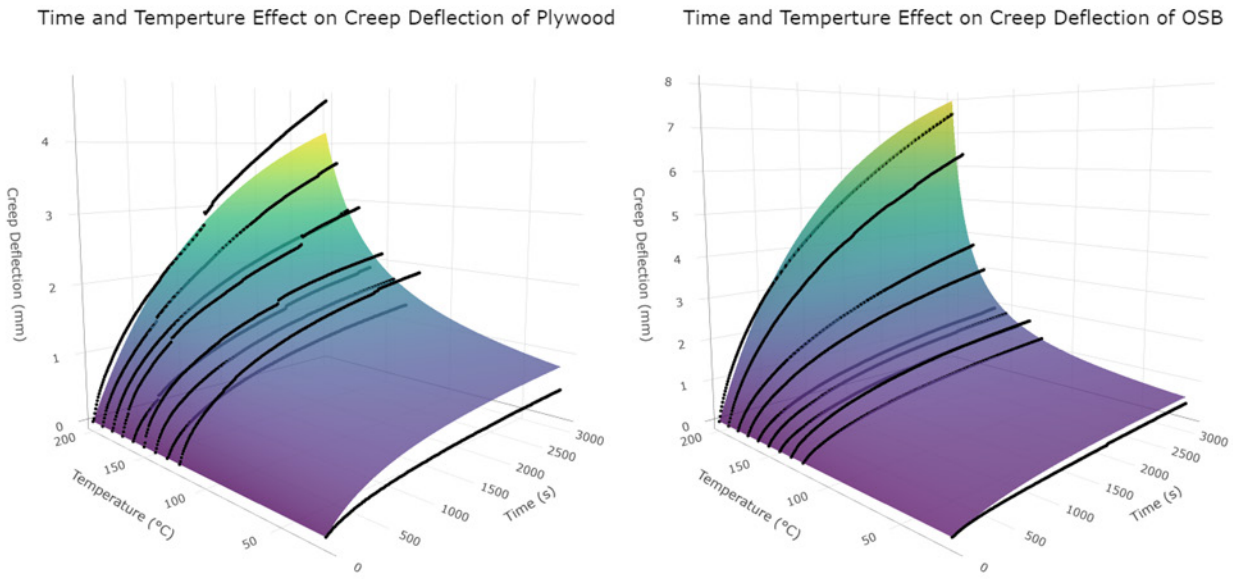

Figure 8. The fitted the temperature-dependent rational creep model from equation 5 for plywood and OSB.

Table 3. Parameters for the temperature-dependent rational creep model.

Material	Parameters				R^2	RMSE
	*e	**f	***g	****j		
Plywood	-2.24	720.29	-0.005	1.12	0.729	0.501
OSB	-5.56	1248.14	-0.010	1.39	0.957	0.347

* Rate of change of the initial stiffness at a given temperature.
** Creep rate at a given temperature.
*** Baseline creep resistance at 0°C.
**** Initial creep rate at 0°C.

Table 4. The calculated parameters (k and n) for each temperature for plywood and OSB.

Temp. (°C)	Plywood			OSB		
	*k	**n	R^2	*k	**n	R^2
20	0.016	0.427	0.986	0.008	0.508	0.997
120	0.051	0.457	0.993	0.028	0.482	0.993
130	0.036	0.453	0.993	0.040	0.474	0.993
140	0.057	0.430	0.995	0.033	0.478	0.994
150	0.057	0.456	0.996	0.043	0.470	0.994
160	0.032	0.510	0.997	0.039	0.486	0.996
170	0.046	0.518	0.997	0.046	0.523	0.997
180	0.054	0.496	0.996	0.047	0.546	0.998
190	0.032	0.596	0.999	0.064	0.576	0.998
200	0.028	0.647	0.998	0.091	0.554	0.999

* Coefficient of time-dependent displacement.
** Exponential material constant.

2) to capture both time and temperature effects on the creep behavior of plywood and OSB. This combination resulted in a unified equation (Equation 7) that reflects the interaction between time-dependent deflection and temperature-induced degradation, similar to the temperature-dependent rational creep model. Before constructing Equation 7, the parameters (k) and (n) of the power model were estimated by fitting Equation 6 to the data, ensuring that the model adequately captured the time-dependent deflection behavior. These parameter values are presented in Table 4 for all 10 tested temperatures, alongside the corresponding R^2 values, which indicate how well the model fits the observed data.

The high R^2 values indicated that the power model fitted the creep deflection data effectively across all temperatures for both plywood and OSB, suggesting that this model accurately captured the time-dependent creep behavior. Given the strong correlations observed in Equations 2 and 6, these equations can be combined to develop a comprehensive governing model. A similar modeling approach was employed by Chang et al. (2023) to predict the time-temperature behavior of wood-plastic composites at temperatures ranging from -45 to 45°C, with stress included in Chang ‘s model. The newly formulated combined equation 7 is referred to as the temperature-dependent power-exponential creep model.

The fitted data for both plywood and OSB can be seen in Figure 9. The parameters and correlation values for the temperature-dependent power-exponential creep model are provided in Table 5. Both plywood and OSB exhibited a high correlation between the model and the observed values, along with relatively low RMSE, indicating minimal deviation between

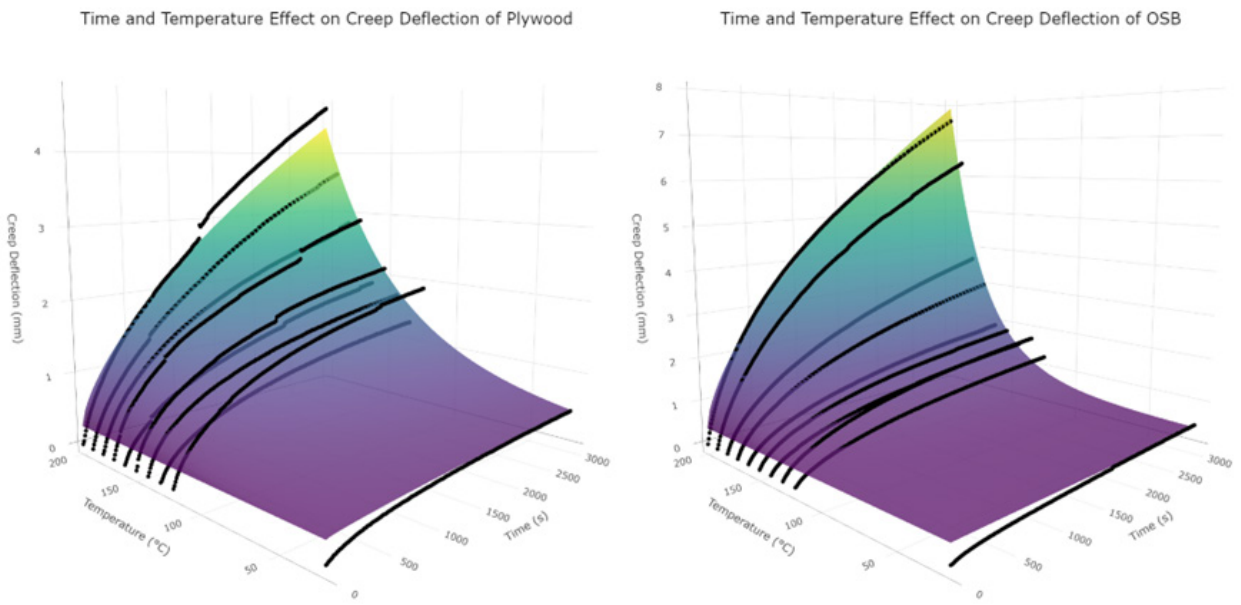

Figure 9. The fitted the temperature-dependent power-exponential creep model from equation 7 for plywood and OSB.

Table 5. Parameters for the temperature dependent power model.

Material	Parameters				R^2	RMSE
	*d	**n	***m	****j		
Plywood	0.0009	0.652	60.693	0.257	0.946	0.222
OSB	0.0003	0.635	30.232	0.380	0.972	0.281

* Coefficient of time-dependent displacement.
** Exponential material constant.
*** Temperature scaling factor .
**** Baseline deflection corresponding to the initial deflection observed at lower temperatures.

the predicted and actual values. Compared to the temperature-dependent rational creep model (5), these results suggest that the temperature-dependent power-exponential creep model (7) is best suited for describing the behavior of both plywood and OSB under constant loading at various elevated temperatures over different time durations.

Conclusion

This study investigated the early-stage primary thermal creep of two common sheathing products, plywood and OSB. Mechanical testing for flexural creep was conducted by applying a constant load at elevated temperatures ranging from 120°C to 200°C for 50 minutes. Deflections were measured continuously to generate average deflection curves for each material at each temperature. These observations revealed that OSB exhibited a substantial increase in deflection between 180°C and 190°C, potentially indicating the onset of adhesive degradation.

Analysis of the maximum deflections after 50 minutes showed that both plywood and OSB began to exhibit increased deflection around 170°C, a temperature associated with the degradation of chemical compounds in wood. An exponential function was used to model the temperature-dependent behavior, providing a good fit to the experimental data and effectively illustrating the effects of temperature on the thermal creep of plywood and OSB.

To incorporate both time and temperature effects on the creep behavior of plywood and OSB, two models were developed and compared: a time-dependent rational function integrated with temperature to create a temperature-dependent rational creep model, and a power law model combined with the exponential function to form a temperature-dependent power-exponential creep model. The temperature-dependent rational creep model worked well for OSB, with an R^2 of 0.95, but performed less effectively for plywood (R^2 of 0.75). In contrast, the temperature-dependent power-exponential creep model demonstrated the

best performance for both plywood and OSB, with R^2 values of 0.94 and 0.97, respectively. The superior performance of the power model aligns with the findings of Chang et al. (2023), who validated its effectiveness for wood-plastic composites at lower temperatures.

Acknowledgements

The authors would like to acknowledge the support of the Wood based Composites Center and the NSF INTERN program for funding this project.

References

American Plywood Association (2020) Engineered wood construction guide. APA Publ No. E30. APA – The Engineered Wood Association.

American Wood Council (2018) National design specification (NDS) for wood construction. American Wood Council.

American Wood Council (2021) Fire performance of wood products awareness guide. https://awc.org/wp-content/uploads/2021/11/fireperformance.pdf

Alonso MV, Oliet M, Domínguez JC, Rojo E, Rodríguez F (2011) Thermal degradation of lignin–phenol–formaldehyde and phenol–formaldehyde resol resins: structural changes, thermal stability, and kinetics. J Therm Anal Calorim 105(1):349-356. https://doi.org/10.1007/s10973-011-1405-0

Clouser WS (1959) Creep of small wood beams under constant bending load. Rep No (2150. US Dept Agric, For Prod Lab.

Chang FC, Lam F, Kadla JF (2014) The effect of temperature on creep behavior of wood-plastic composites. J Reinf Plast Compos 33(9):883-892. https://doi.org/10.1177/0731684414523691

Chang FC, Lam F (2018) Effects of temperature-induced strain on creep behavior of wood–plastic composites. Wood Sci Technol 52(5):1213-1227. https://doi.org/10.1007/s00226-018-1033-y

Desai HP, O'Dell JL (1989) Thermal stability and combustion characteristics of isocyanates in fire-retardant applications. Fire Mater 14(2):65-72.

Dietenberger MA, Hasburgh LE (2016) Wood products: thermal degradation and fire. In: Reference Module in Materials Science and Materials Engineering. Elsevier. https://doi.org/10.1016/B978-0-12-803581-8.03338-5

Fengel D, Wegener G (1989) Wood: chemistry, ultrastructure, reactions. de Gruyter.

Granello G, Palermo A (2019) Creep in timber: research overview and comparison between code provisions. N Z Timber Des J 27(1):6-22.

Green DW, Evans JW, Craig BA (2003) Durability of structural lumber products at high temperatures. Part I. 66°C at 75%RH and 82°C at 30%RH. Wood Fiber Sci 499-523.

Huang Q, Zhao Z, Cai J, Chen H, Niu B, Fang F, Quan D, Zhang Y, Long D (2024) New insights into phenolic resin decomposition under oxidative conditions of high temperature. Ind Eng Chem Res. 63(6):2642-2656. https://doi.org/10.1021/acs.iecr.3c03573

Hoyle RJ, Griffith MC (1985) Primary creep in Douglas-Fir beams of commercial size and quality. Wood Fiber Sci 17(3):300-314.

Hsieh TY, Chang FC (2018) Effects of moisture content and temperature on wood creep. Holzforschung 72(10):1071-1078. https://doi.org/10.1515/hf-2018-0056

International Code Council (2018) International residential code. Falls Church, VA.

Kerber S (2012) Analysis of changing residential fire dynamics and its implications on firefighter operational timeframes. Fire Technol 48(4):865-891. https://doi.org/10.1007/s10694-011-0249-2

Lebow PK, Winandy JE (1999) Verification of a kinetics-based model for long-term effects of fire retardants on bending strength at elevated temperatures. Wood Fiber Sci. 31(1):49-61.

Madsen B (1992) Structural behaviour of timber. Timber Engineering Ltd.

Moosavi V, Eslam HK, Bazyar B, Najafi A, Talaeepoor M (2017) Bending creep behavior of hornbeam wood. Drvna Ind 67(4):341-350. https://doi.org/10.5552/drind.2016.1609

Paál M, Rychlý J, Vykydalová A, Šurina I, Lisý A, Brezová V, Nemčeková K, Labuda J (2023) Burning and thermal degradation of wood under defined conditions: a route of preparation of carbonaceous char and its characterization for potential applicability in evaluation of real fire. Fire Technol 59(5):2733-2749. https://doi.org/10.1007/s10694-023-01422-7

Peleg M (1979) A model for creep and early failure. Mater Sci Eng 40:197-205.

Rammer DR, Zelinka SL, Hasburgh LE, Craft ST (2018) Ability of finger-jointed lumber to maintain load at elevated temperatures. Wood Fiber Sci 50(1).

RStudio Team (2023) RStudio: integrated development for R. RStudio, PBC. https://www.rstudio.com/

Sebio-Puñal T, Naya S, López-Beceiro J, Tarrío-Saavedra J, Artiaga R (2012) Thermogravimetric analysis of wood, holocellulose, and lignin from five wood species. J Therm Anal Calorim. 109(3):1163-1167. https://doi.org/10.1007/s10973-011-2133-1

Siimer K, Kaljuvee T, Pehk T, Lasn I (2010) Thermal behaviour of melamine-modified urea–formaldehyde resins. J Therm Anal Calorim 99(3):755-762. https://doi.org/10.1007/s10973-009-0617-z

Sinha A, Gupta R, Nairn JA (2011) Thermal degradation of bending properties of structural wood and wood-based composites. Holzforschung 65(2). https://doi.org/10.1515/hf.2011.001

Sinha A (2013) Thermal degradation modeling of flexural strength of wood after exposure to elevated temperatures. Wood Mater Sci Eng 8(2):111-118. https://doi.org/10.1080/17480272.2012.753950

Smulski SJ (1989) Creep functions for wood composite materials. Wood Fiber Sci. 21(1):45-54.

US Fire Administration (2021) One- and two-family residential building fires (2017-2019). Topical Fire Rep Ser. 21(6). https://www.usfa.fema.gov/statistics/reports/where-fires-occur/1-2-family-residential-building-fires-v21i6.html

Wei Y, Zhao L (2023) Effect of temperature on the bending and creep properties of wood-plastic composites. Polym Compos 44(8):4612-4622. https://doi.org/10.1002/

Winandy JE, LeVan R, Ross RJ, Hoffman M, McIntyre CR (1991) Thermal degradation of fire-retardant-treated plywood: development and evaluation of a test protocol. USDA For Serv Res Pap FPL501, Madison, WI.

Yang WP, Macosko CW, Wellinghoff ST (1986) Thermal degradation of urethanes based on 4,4′-diphenylmethane diisocyanate and 1,4-butanediol (MDI/BDO). Polymer 27(8):1235-1240. https://doi.org/10.1016/0032-3861(86)90012-1

Zhong Y, Zhou H, Wen L (2015) The effect of elevated temperature on bending properties of normal wood inside Chinese larch wood during fire events. BioResources 10(2):2926-2935. https://doi.org/10.15376/biores.10.2.2926-2935

Effect of graphene oxide addition on the characteristics of nanocomposite films made of graphene oxide and nanocellulose obtained from recycled pulp

Hirsa Jouya
hirsa.jouya@srbiau.ac.ir

*Mohammad Talaeipour**
E-mail: m.talaeipoor@srbiau.ac.ir

Amir Hooman Hemmasi
h_hemmasi@srbiau.ac.ir

Behzad Bazyar
Department of Wood and Paper Science, Faculty of Natural Resources and Environment, Science and Research Branch, Islamic Azad university, Tehran, Iran
bazyar@srbiau.ac.ir

Alain Dufresne
Université Grenoble Alpes, CNRS, Grenoble INP, LGP2, F-38000 Grenoble, France
alain.dufresne@pagora.grenoble-inp.fr

(Received 7 February 2024)

Abstract. Films consisting of 6,6,2,2-tetramethylpiperidine-N-oxyl (TEMPO) oxidized cellulose nanofibers (TOCNFs) prepared from recycled pulp and graphene oxide (GO) were produced by the solution molding method. Electrical conductivity titration and FTIR spectra showed that recycled fibers and cellulose nanofibers were successfully oxidized and the number of carboxyl groups increased. Mechanical properties, thermal stability, crystallinity index, and morphological structure of the nanocomposite films of TOCNFs and GO were characterized by tensile strength tests, thermal gravimetric analysis (TGA), X-ray diffraction (XRD), and scanning electron microscopy (SEM). Tensile strength of films made of TOCNFs with 1.5% GO was 61% higher than those without GO, while tensile strength TOCNF films with 3% GO decreased by 2%. The values did not differ statistically from the non-amended TOCNF. Addition of up to 3% GO did not markedly affect thermal stability of nanocomposite films. Recycled pulp had 83% crystallinity, while the crystallinity index of TEMPO-oxidized cellulose nanofibers decreased to 65.5%. SEM observations showed that TOCNFs and small amounts of GO formed nanocomposite films with a homogeneous structure. This research provides an approach for effective utilization of recycled pulp as a feedstock for cellulose nanofibers and TOCNFs/GO nanocomposite films.

Keywords: Bio-nanocomposite; Cellulose nanofibers; TEMPO-oxidation; Recycled Pulp; Graphene oxide

Introduction

Nanocomposites based on biopolymers, and Nano-scale fillers are of scientific and industrial interest in terms of their biological efficiency and potential for significant performance improvements (Sellinger et al. 1998). Biodegradable nanocomposites are made from biopolymers such as polysaccharides, proteins, and fats. As a renewable, biodegradable, and non-toxic material, cellulose is the most abundant natural polymer on earth. It is produced via photosynthesis at the rate of 10^{11} - 10^{12} t/year (Klemm et al. 2002) and has been used to produce nanocellulose (Turbak et al. 1983). Cellulose nanofibers have attracted a lot of attention in Europe and their cost-effective production is a priority to address a number of environmental issues (Rol et al. 2019). Cellulose nanofibers have distinct features in comparison to cellulose fibers rendering them advantageous for a range of applications including packaging (Lavoine et al. 2012; Saini et al. 2016), printed electronics (Hoeng et al. 2016), papermaking (Bardet et al. 2014; Brodin et al. 2014), composites (Mariano et al. 2014; Oksman et al. 2016), and medicines (Jorfi and Foster 2015).

Cellulose nanofibers have at least one dimension in the nanoscale, have a high specific surface area, and behave like a gel in water. They are transparent and compatible with the

* Corresponding author

environment while retaining unique mechanical and barrier properties. Production of cellulose nanofibers on an industrial scale is possible due to the discovery of methods for reducing energy consumption during mechanical treatment. The energy consumption associated with the manufacturing of cellulose nanofibers utilizing homogenizers, microfluidizers, and grinders is considerable, mostly attributable to the abundance of surface hydroxyl groups that facilitate substantial hydrogen bond interactions among nanofibrils. Over the last decade, several studies have been conducted to decrease energy consumption and enhance the nanofibrillation process (Rol et al. 2019). Two methods have been proposed: new mechanical processes and/or chemical modification of cellulosic fibers. The most common pretreatment method for preparing cellulose microfibrils is TEMPO-oxidation. Oxidation using a 6,6,2,2-tetramethylpiperidine-N-oxyl (TEMPO) mediator includes the conversion of hydroxyl groups into aldehyde and carboxyl functional groups in an aqueous environment at room temperature (Rol et al. 2019).

The main weakness of biopolymer films is their poor mechanical properties and research has been conducted to improve the mechanical properties of polysaccharide-based films (Gontard et al. 1993; Hagenmaier and Shaw 1990; Maftoonazad et al. 2008; Park et al. 1993; Yang and Paulson 2000). Modification of polymers with minerals has been shown to improve polymer properties, including their mechanical strength (Colemanet al. 2006; Han et al. 2011a; Han et al. 2011b). On the other hand, the use of graphene and graphene oxide (GO) in materials research has attracted tremendous attention in various fields, including biomedicine (Feng et al. 2012; Li et al. 2008; Li et al. 2011).

Graphene is an allotrope of carbon consisting of a two-dimensional sheet with SP2 hybridization and a hexagonal lattice structure. Graphene has a variety of mechanical and electrical characteristics that render it well-suited for enhancing the strength of polymer matrices. Several studies have used GO nanosheets or reduced GO to enhance the mechanical or electrical properties of polymers (Salavagione et al. 2009; Steurer et al. 2009; Wu and Liu 2010; Xu et al. 2010). These studies showed that uniform distribution of graphene in the polymer matrix was necessary to obtain the best characteristics.

The large specific surface area of GO has -OH, -COOH, -O- and -C=O functional groups that make it hydrophilic and easily dispersible in water and some organic solvents (Paredes et al. 2008). This makes it simple to fabricate GO sheets using the solution molding technique. Research has shown that GO may be evenly disseminated in a chosen polymer matrix to create graphene oxide-based nanocomposites with superior mechanical and thermal characteristics (Fang et al. 2009; Liang et al. 2009; Villar-Rodil et al. 2009).

Since GO is prepared from inexpensive graphite, it has a tremendous cost advantage over carbon nanotubes, which has encouraged research on polymer/GO composites (He et al. 2012; Rana et al. 2011; Yang et al. 2010).

Feng et al. (2012) produced flexible nanocomposite films consisting of GO and bacterial cellulose and used scanning electron microscopy and X-ray diffraction to show that GO nanosheets were uniformly dispersed in the bacterial cellulose matrix. Furthermore, they found a 10% increase in Young's modulus and a 20% increase in tensile strength in films containing bacterial cellulose, and 5% (wt/wt) gain of GO compared to bacterial cellulose film.

Han et al. (2011) showed that chitosan and GO composite films could be mixed uniformly and that mechanical properties of the composite films, especially in the wet state, increased significantly compared to the chitosan film. These composite films showed a high storage modulus of up to 200°C.

The link between the dispersion state and the reinforcing effect of GO in composite films containing microcrystalline cellulose was examined by Wang et al. (2012) who found that mechanical qualities of composite films were much better than those of the microcrystalline cellulose film and that the strengthening impact of GO and its state of dispersion were closely related.

Yadav et al. (2013) showed that nanocomposite films consisting of sodium carboxymethyl cellulose and 1% GO had had significantly higher tensile strength and Young's modulus than sodium carboxymethylcellulose film alone. Nanocomposite films also showed storage moduli up to 250°C.

Xu et al. (2015) studied the effect of GO on the properties of cellulose nanofibers extracted from banana petiole fibers. They showed that the tensile strength and thermal properties of nanocomposite films were improved when less than 4.4% GO was added.

Zhang et al. (2019) studied the effect of GO and black phosphorus on the physical properties of regenerated cellulose films synthesized from agricultural corn stalk waste. They demonstrated that parenchyma cells derived from maize stem pith could be used to produce regenerated cellulose. Addition of small quantities of GO and black phosphorus to the regenerated cellulose base material improved the performance of regenerated cellulose composite films.

Wang et al. (2018) prepared a composite of GO, chitosan, and cellulose by the phase transfer method. They showed that GO improved the thermal stability of films containing chitosan and cellulose while tensile strength and elongation at break increased in films with low loading levels of GO.

GO has been used as a reinforcement in polysaccharide base materials such as sodium carboxymethyl cellulose (Yadav et al. 2013), bacterial cellulose (Feng et al. 2012), chitosan (Wang et al. 2018), microcrystalline cellulose (Wang et al. 2012) and cellulose nanofibers extracted from banana petiole fibers (Xu et al. 2015). Although a number of studies have been performed on production of cellulose nanofibers from paper pulp, few reports are available on the production of cellulose nanofibers from recycled pulp. The use of TEMPO-oxidized cellulose nanofibers obtained from recycled pulp and their use in the production of nanocomposite films reinforced with GO has not been fully researched.

The objective of this study was to examine the effects of 0.5, 1.5 or 3.0% GO addition on the properties of TOCNFs as the base material to produce nanocomposite films. The mechanical properties and thermal stability of the nanocomposite films of TOCNFs and GO were studied by tensile strength tests and thermogravimetric analysis (TGA).

Materials and methods

Greenfield94 recycled pulp was obtained from the Polytechnic Institute of Grenoble, France, with the specifications listed in Table 1 as cellulose raw material. 6,6,2,2-tetramethylpiperidine-N-oxyl (TEMPO), sodium bromide, sodium hypochlorite solution (15%), hydrochloric acid, and sodium hydroxide were purchased from Sigma-Aldrich and used without further purification. Graphene oxide dry sheets (particle size: 0.2-2 microns) were purchased from Graphene Laboratories (Ronkonkoma, NY, USA). Deionized water was used in all experiments.

TEMPO oxidation of cellulose fibers

Saito's method was used for TEMPO oxidation of cellulose fibers (Saito et al. 2007). Two hundred g of recycled pulp (based on dry weight) was soaked in 10 L of water for 4 hours and then stirred for 5 minutes with an electric stirrer (suspension concentration 0.02 g/mL). TEMPO (1.6 g, with 98% purity) was added and softened with a mortar; 10.3 g sodium bromide (99.5% purity) was added. A 10-15% solution of sodium hypochlorite adjusted to pH 10 with hydrochloric acid and 286.3 g of it was added to the mixture. The suspension was placed in a flask at 25°C with stirring at 200 revolutions per minute for 5 minutes after TEMPO and sodium bromide were added. Sodium hypochlorite was added to the mixture, and 10 L of deionized water were added to produce a concentration to 0.01 g of cellulose/mL. The suspension pH was maintained at 10 by dropwise addition of sodium hydroxide until no reduction was observed, indicating that carboxyl groups were no longer formed and the sodium hypochlorite was completely consumed. The reaction was quenched by lowering the pH to 7 using hydrochloric acid. The suspension was washed with deionized water on a Büchner funnel and a nylon mesh with a hole diameter of 0.65 µm. Figure 1 shows the general pathway of the TEMPO oxidation reaction. The material was resuspended and diluted to 0.02 g/mL using deionized water to produce cellulose nanofibers. The suspension was passed through a grinding machine several times and at certain angles among the disc plates.

Table 1. Specifications of recycled pulp

Mean length-weighted fiber length	859 µm
Mean fiber width	23.7 µm
Macro fibrillation index	0.603%
Fine content, % in length	30.88%

Electrical conductivity titration

The number of carboxyl groups in TEMPO-oxidized cellulose fibers was determined via electrical conductivity titration. Fifteen mg of TEMPO oxidized cellulose fibers were mixed in 200 mL of deionized water in a 500 mL beaker in an ultrasonic bath for 5 minutes. The pH of the suspension was adjusted to 3 using 0.1 M hydrochloric acid (replacing sodium ions with protons). The suspension was titrated by adding 0.2 mL of 0.01 M sodium hydroxide solution. The amount of grafting was calculated in µmol/g with the following formula (da Silva Perez et al. 2003):

$$X = \frac{C \times (V_2 - V_1)}{w} \quad (1)$$

Where X was the amount of carboxyl groups (µmol/g), C was the concentration of sodium hydroxide solution (µmol/L), V_1 corresponded to the presence of an excess amount of strong hydrochloric acid (L), V_2 corresponded to the amount of weak carboxylic acid (L), and was the dry weight of the sample (g).

Production of cellulose nanofibers

After TEMPO-oxidized pre-treatment, the 2% suspension of TEMPO fibers in water was ground in a Matsuko Ultra-fine

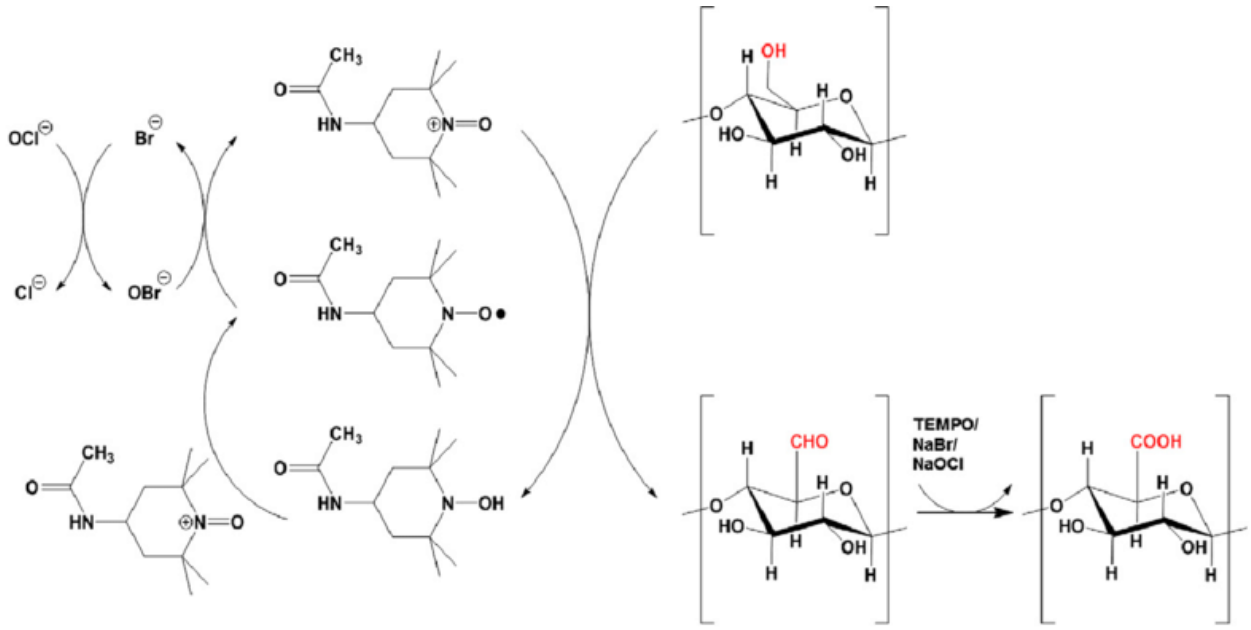

Figure 1. General schematic of TEMPO oxidation (Paquin, Loranger, Hannaux, Chabot, & Daneault, 2013)

friction grinder (Matsuko Sangyo, Honcho, Japan) at 1500 rpm and 32 passes through the grinder (10, 10, 10 and 2 passes, respectively, with the distance between the two discs set between "0", "-5", "-10" and "-20"). This device uses a vertically stacked pair of stone discs. The bottom disk rotates while the top disk remains stationary. The distance between the two discs was modified to a value of -100 µm relative to the initial location of zero displacement prior to the application of the dough. The zero-movement position was determined as the contact position between the two grinder discs before loading the dough. There was no direct contact between two grinding stones, even in the negative setting of the disc position. The resulting suspension of cellulose nanofibers is shown in Figure 2a.

Preparation of TOCNFs/GO nanocomposite films

Nanocomposite films based on TOCNFs containing 0.5, 1.5, and 3 wt% of GO were produced by the solution molding method (Wang et al. 2005). The appropriate amount of suspension of cellulose nanofibers needed to obtain 0.25 g of cellulose nanofibers (based on dry weight) was diluted in deionized water then, 0.000125, 0.00375, and 0.0075 g of GO were mixed in deionized water to prepare films containing 0.5, 1.5, and 3 wt% of GO. The mixtures were subjected to ultrasonic waves in an ultrasonic bath for 15 minutes. Subsequently, the cellulose nanofiber solution was combined with the GO suspension, and 50 ml of deionized water was added. The mixture was blended in an IKA ULTRA-TURRAX homogenizer (IKA Works, Wilmington, NC, USA) for 3 minutes at 7200 rpm, then stirred for 10 minutes while the pH was adjusted to 7 using 0.1 M hydrochloric acid. The mixture was stirred for 1 hr then placed in an ultrasonic bath for 3 minutes to remove the bubbles. The suspension was poured into a Petri dish and oven-dried at 40°C for 24 hr. The thin films of nanocomposite of TOCNFs and GO with an average thickness of 40 µm were characterized (Figure 2b).

Fourier transform infrared spectroscopy (FTIR)

Functional groups of recycled pulp, TEMPO-oxidized cellulose nanofibers, TOCNF/GO nanocomposite films, and graphene oxide were examined using a Bruker Model Vertex 80 FTIR spectrometer (Bruker Inc, Bellerica, MA, USA) equipped with an attenuated total reflection system was used. All sample spectra were collected by accumulating 32 scans from 500 to 4000 cm^{-1}. The background spectrum was collected and subtracted from the original spectrum for each sample.

X-ray diffraction (XRD)

The effects of TEMPO-oxidation pretreatment and mechanical grinding treatment on the crystallinity index of cellulose fibers were investigated by XRD. Recycled pulp, TEMPO-oxidized cellulose nanofibers, TOCNF-GO films and graphene oxide were separately oven-dried at 40°C for 24 hours and powder was prepared from them. Recycled pulp was used as a reference sample. X-ray diffraction spectra were prepared using an XPERT-MDP diffractometer (Malvern Panalytical, Malvern,

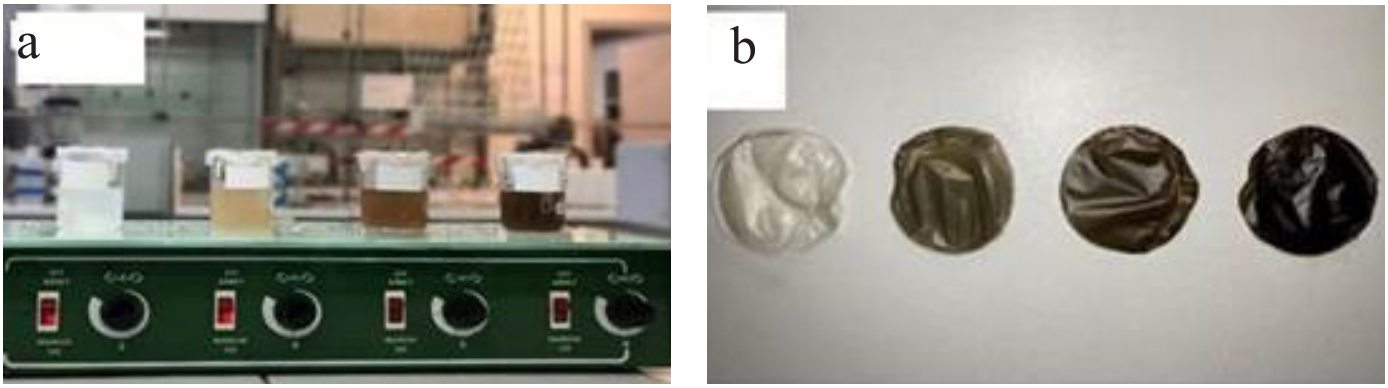

Figure 2. Examples of (a) TOCNFs and TOCNFs/GO suspensions where beaker on the left is TOCNF alone and those to the right containing increasing amounts of GO and (b) TOCNFs/GO nanocomposite films containing 0, 0.5, 1.5 and 3 wt% GO (from left to right, respectively).

United Kingdom) with Cu-Kα radiation at 40 kV and 30 mA at a scan rate of 0.02° s^{-1} over a 2θ scan in the range 10-60°. The crystallinity indices (C.I.) for recycled pulp and TEMPO-oxidized cellulose nanofibers were calculated based on Segal's experimental method (Segal et al. 1959):

$$CI = \frac{I_{002} - I_{AM}}{I_{002}} \times 100 \quad (2)$$

Where I_{002} was the intensity of 002 reflection (2θ between 22° and 23°) and I_{AM} was the minimum value at 2θ between 18° and 19°, which represented the reflection intensity of the amorphous phase.

Scanning electron microscopy (SEM)

Scanning electron microscopic images of oxidized TEMPO nanofibers, and fracture sections of TOCNF/GO nanocomposite films were taken using Field Emission Gun (FEG) SEM, and FEI ESEM QUANTA 200 (Hillsboro, OR USA), respectively. The fracture surface of the films was sputter-coated with gold for better viewing. A drop of a suspension of oxidized TEMPO cellulose nanofibers with a very low solid content, about 10^{-5} %, was placed on a carbon-coated grid and sputter-coated with gold.

Atomic force microscopy (AFM)

A VEECO Nanoscope MultiMode IIIA atomic force microscope (AFM) was used to examine graphene oxide nanosheets. The samples were prepared by depositing a dilute mixture of graphene oxide on the surface of mica and examining the resulting surface.

Transmission electron microscope (TEM)

A Philips Tecnai G2 F20 Transmission electron microscope (TEM) (Philips, Grenoble, France) operating at 200 kV was used to examine graphene oxide nanosheets. GO nanosheets were deposited on a nickel/SiO_2/Si wafer via CVD.

Tensile test

The tensile strength of TOCNF/GO nanocomposite films (5 by 15 mm by nominal thickness of 40 μm) was determined using a SANTAM STM-50 tensile tester (Santam, Teheran, Iran) at a speed of 1 mm/min and a force of 100 N. All the samples were conditioned for 24 hours at 23 ± 5°C and a relative humidity of 50% ± 1% prior to testing. Three samples were evaluated for each film type and values were averaged. The data were subjected to an analysis of variance and means were compared using Duncan's modified least significance test at α = 0.05.

Thermal Gravimetric Analysis (TGA)

Thermal gravimetric analysis (TGA) was performed using a NETSCZH STA 449 C Jupiter simultaneous TG-DSC analyzer (Selb, German). The temperature was increased from room temperature to about 900°C in a nitrogen atmosphere at a rate of 10°C/min. A 10 mg sample was used for each run and the resulting curves were analysed.

Results and discussion

Electrical conductivity titration curves for recycled pulp, TEMPO-oxidized recycled pulp, and TEMPO-oxidized cellulose nanofibers

Electrical conductivity titration curves for recycled pulp, TEMPO-oxidized recycled pulp and TEMPO-oxidized cellulose nanofibers exhibited three separate phases (Figure 3). In the first phase, electrical conductivity decreased in terms of the neutralization of protons (H^+) by hydroxyl ions (OH^-), and the increase of ions (Na^+) which have little mobility. The second phase involved neutralization of carboxylic groups, during which electrical conductivity remained basically unchanged. Sodium ions (Na^+) are absorbed by carboxylic acid groups,

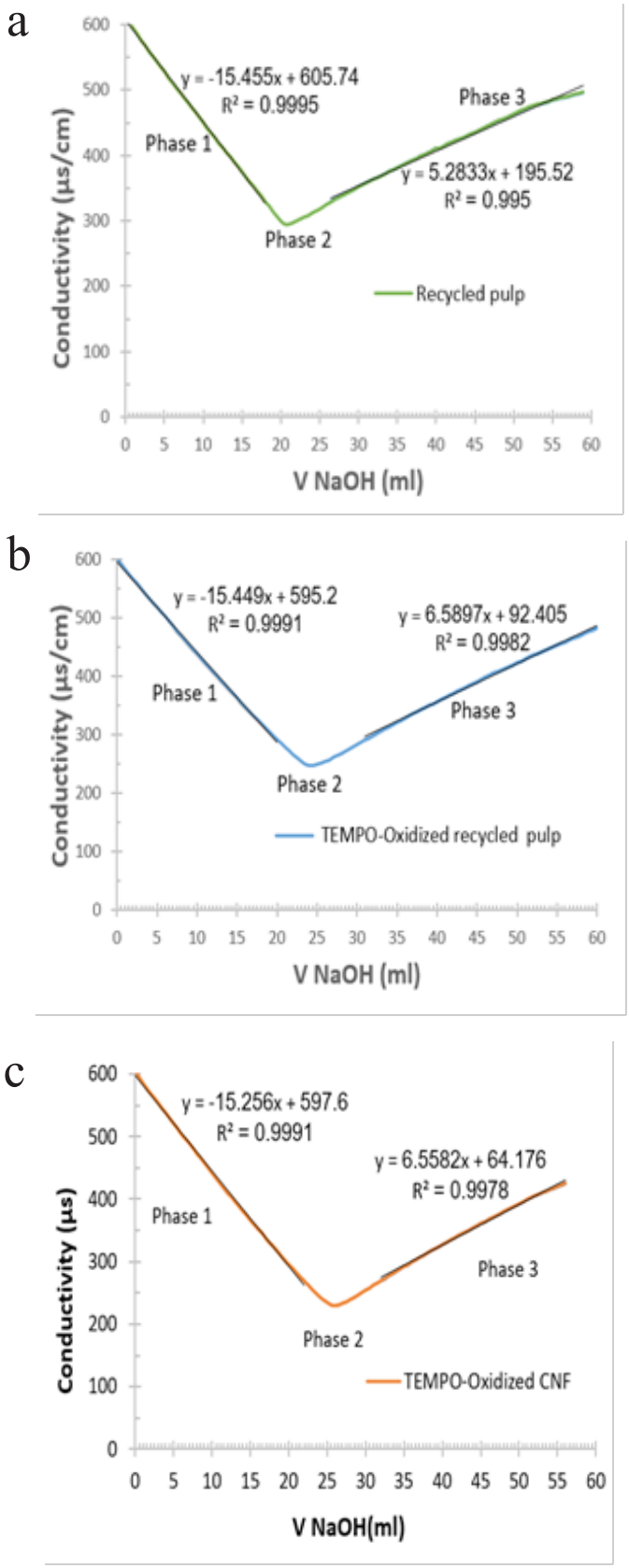

Figure 3. Electrical conductivity titration curves for (a) the recycled pulp, (b) TEMPO-oxidized recycled pulp and (c) TEMPO-oxidized CNF.

and protons (H^+) are neutralized by hydroxyl ions (OH^-). In the third stage, there was an overabundance of sodium hydroxide which increased electrical conductivity. A carboxyl group concentration of around 300 µmol/g is required to create a cellulose nanofiber gel, which may greatly minimize the number of mechanical treatment procedures (Besbes et al. 2011a; Wang et al. 2005). The amounts of carboxylic groups for recycled pulp, TEMPO-oxidized recycled pulp, and TEMPO-oxidized cellulose nanofibers, respectively, were calculated as 117, 975, and 890 µmol/g. The increase in the number of carboxyl groups of TEMPO-oxidized recycled pulp compared to recycled pulp without oxidation confirmed the oxidation of cellulose fibers.

FTIR spectra for recycled pulp, TOCNFs/GO0% film, TOCNFs/GO3% film and graphene oxide

FTIR measurements were used to qualitatively confirm the oxidation level of TEMPO-oxidized cellulose nanofibers. Figure 4 shows the FTIR spectra for recycled pulp, TOCNF/GO0% film, TOCNF/GO3% film, and GO. The absorption peak near 1600 cm^{-1} is related to the C=O stretching vibration of COO^- group. As expected, since the amount of COO^- group in recycled pulp was very low, the absorption peak of 1600 cm^{-1} was more obvious for oxidized cellulose nanofibers than recycled pulp and confirmed the oxidation of cellulose fibers (Benhamou et al. 2014).

Oxygen atoms in GO exist in the form of $-COOH$, $-CO=O$, $-OH$, and $-C-O-C$ groups on the surface or edge of GO sheets and play an important role for improving compatibility between GO and cellulose nanofibers (Wang et al. 2012). Peaks at 1059, 1374.3, 1719.3, 3383.9 and 1621.1 cm^{-1}, respectively, in the GO spectra were attributed to $C-O$ (epoxy or alkoxy functional group), $O-H$ (from carboxyl functional group), C=O (carboxyl and carbonyl functional group), O-H (hydroxyl functional group) and $-C=C-$ functional group (Wang et al. 2012). The absorption peak resulting from the stretching vibration of $O-H$ at 3348 cm^{-1} in nanocomposite films containing 0% or 3% GO decreased compared to recycled pulp. Absorption peaks were also observed at 1600 and 1719 cm^{-1} and are related to stretching vibration of C=O for both TOCNF/GO0%, and TOCNF/GO3%. The reduction of hydroxyl groups appeared to be related to their replacement with carboxyl groups as a result of TEMPO-oxidation. Many oxygen-containing functional groups make GO sheets highly hydrophilic and improve their miscibility in water.

Mechanical properties of TOCNFs/GO nanocomposite films

The mechanical properties of TOCNFs/GO nanocomposite films depend on the uniform distribution of GO in the base

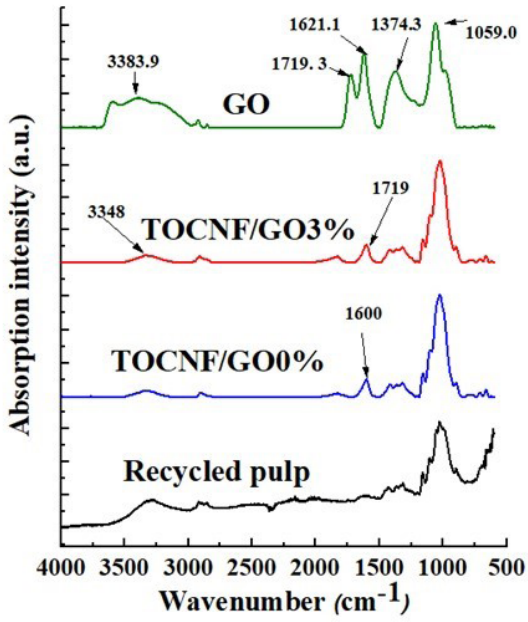

Figure 4. FTIR spectra for recycled pulp, TOCNFs/GO0%, TOCNFs/GO3% and GO.

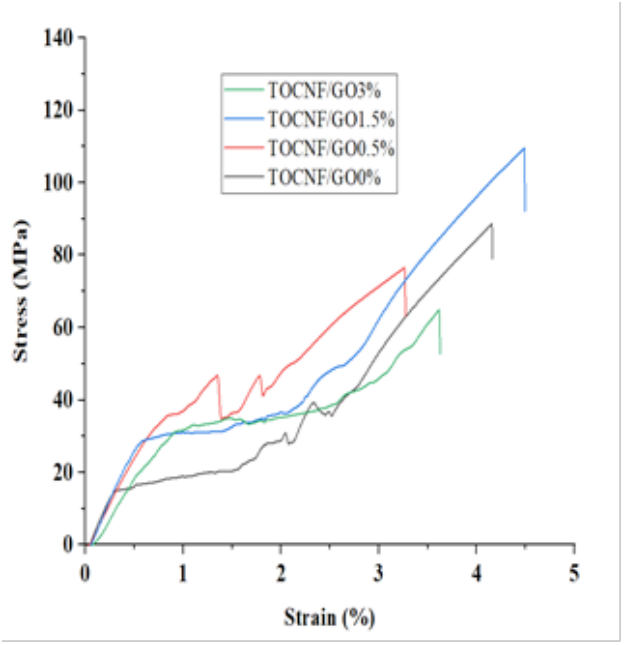

Figure 5. Typical stress-strain curves for TOCNF nanocomposite films with increasing levels of GO.

material of TEMPO-oxidized cellulose nanofibers and the degree of reaction between GO and TOCNFs. Figure 5 shows the stress-strain curves for TOCNFs/GO nanocomposite films. The mechanical properties of TOCNFs/GO nanocomposite films are summarized in Table 2.

Average Young's modulus and tensile strength of TOCNFs/GO0.5%, and TOCNFs/GO1.5% nanocomposite films increased compared to the non-GO amended film (Table 2). The average Young's modulus and average tensile strength of TOCNFs films amended with 1.5% GO were 24% and 61% higher than those obtained for TOCNFs/GO0% film, respectively. The results indicated that proper GO distribution of GO in TOCNFs and the compatibility between TOCNFs and GO contributed to increased film mechanical properties. Oxygen-containing groups in GO can react with TOCNFs through hydrogen. Average Young's modulus and tensile strength for TOCNF/GO3% film were, respectively, 24% and 2% less than those obtained for the none-GO containing TOCNF film. An ANOVA of the data indicated that the addition of GO had no significant effect on either tensile strength or Young's modulus (Table 3).

Table 2. Effect of different levels of GO on mechanical properties TOCNFs/GO nanocomposite films.[a]

GO loading (wt%)	Young's modulus (GPa)	Tensile strength (N)	Elongation at break (%)
0	1.79 (1.11)[a]	10.72 (7.10)	3.80 (0.47)
0.5	2.76 (0.68)	11.08 (3.58)	4.20 (1.85)
1.5	2.22 (0.21)	17.29 (4.29)	5.30 (1.62)
3	1.35 (0.06)	10.50 (2.83)	3.90 (0.91)

a. Values represent means of three replicates while figures in parentheses are one standard deviation.

Table 3. Analysis of variance examining the effect of GO addition on the mechanical strength of nanocomposite films.

	Sum of squares	df	Mean square	F	Sig.
Between Groups	96.348	3	32.116	1.432	0.304
Within Groups	179.481	8	22.435		
Total	275.829	11			

Thermal gravimetric analysis

The thermal stability of nanocomposite films without GO (TOCNFs/GO0%) up to about 300°C was higher than the that of GO (Figure 6). The process of thermal degradation was reversed above 300°C. Thermal degradation of GO slowed above that temperature, but continued for nanocomposite films with or without GO up to 800°C. TGA tests showed that thermal stability of nanocomposite films was better up to 300°C. This could be due to the presence of cellulose nanofibers in the nanocomposite films that imparted TOCNFs with intrinsic resistance to heat. However, thermal degradation of TOCNFs was initiated above 300°C. The addition of up to 3% GO did not greatly affect the thermal stability of the nanocomposite

films. The carbonaceous residue after thermal degradation at 800°C for TOCNFs/GO0%, TOCNFs/GO0.5%, TOCNFs/GO1.5%, and TOCNFs/GO3% nanocomposite films were respectively 12.8%, 15.45%, 15.53%, and 16.35% (Figure 6-c). These observations are consistent with the results of Wang et al. (He et al. 2012), who synthesized composite films consisting of microcrystalline cellulose and GO. They showed that the thermal degradation temperature for the GO films was lower than the pure microcrystalline cellulose film and the amount of carbonaceous residue at 700°C increased compared to the pure microcrystalline cellulose film.

X-ray Diffraction (XRD) Analysis for recycled pulp, TOCNFs, and TOCNFs/GO Nanocomposite Films

XRD spectra for recycled pulp and TOCNFs are shown in Figure 7-a. Compared to the recycled pulp with 83% crystallinity, the crystallinity value of TOCNFs decreased to 65.5%, indicating that the mechanical defibrillation disrupted the crystallites through the breaking effect or peeling-off mechanism of the cellulose chains (Besbes et al. 2011b). Figure 7-b shows the XRD spectra for GO, TOCNFs, and TOCNFs/GO nanocomposite films. The analysis of the XRD spectrum for GO showed an interlayer distance of 0.76 nm, which was within the range of previously reported values (Besbes et al. 2011b; Dubin et al. 2010; Liao et al. 2011). All the XRD spectra for TOCNFs/GO nanocomposite films showed three distinct peaks at $2\Theta = 15.8°$, 22.74°, and 35.0° which were assigned to the $(\bar{1}10)$, (200), and (003) planes, respectively, that indicated the characterization of cellulose I. The XRD spectra for TOCNFs/GO0.5%, TOCNFs/GO1.5%, and TOCNFs/GO3% nanocomposite films were very similar to those of TOCNFs/GO0%, and the diffraction peak corresponding to GO was not

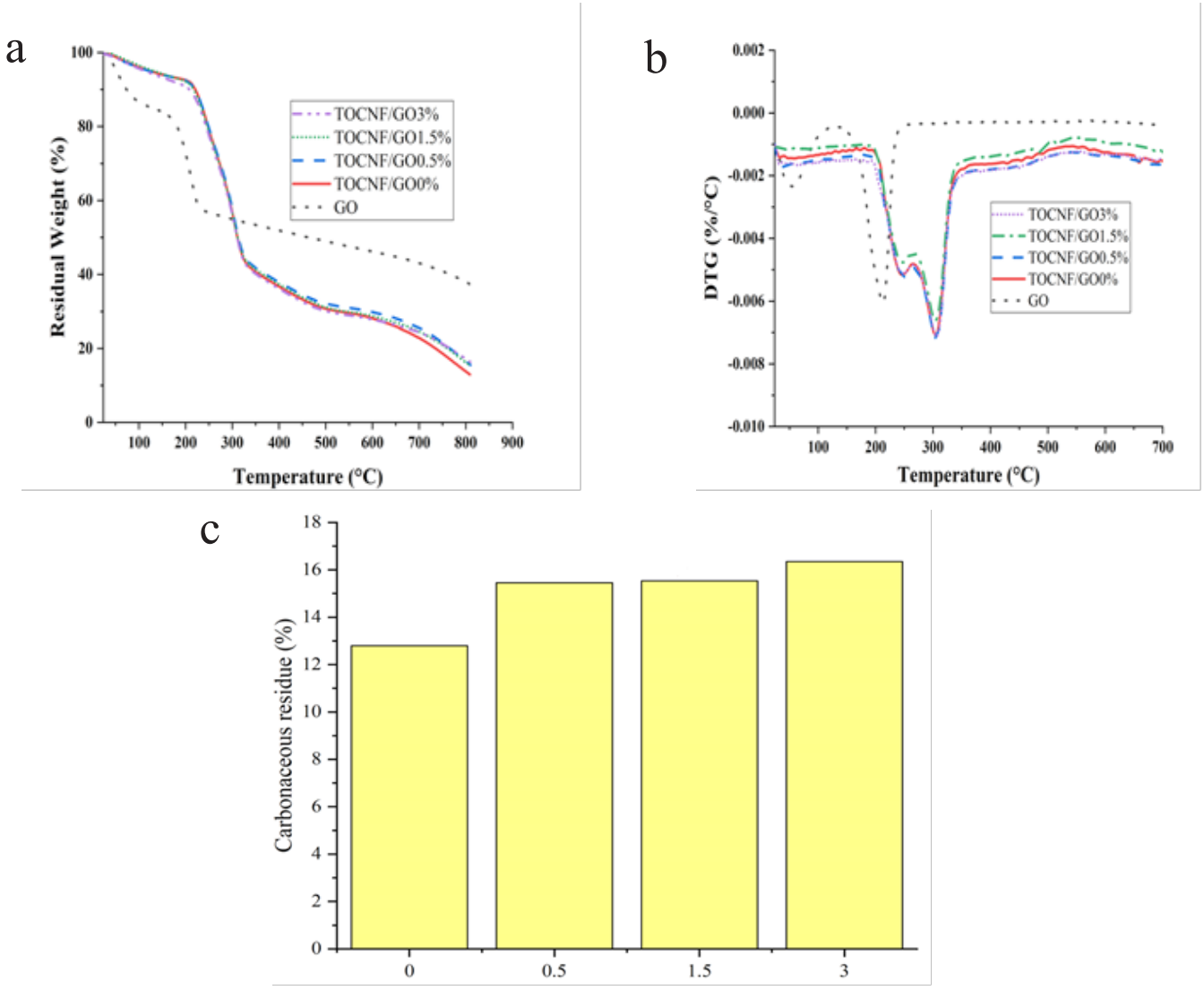

Figure 6. (a) TGA and (b) DTG curves for TOCNFs and TOCNFs/GO nanocomposite films, and (c) carbonaceous residue at 800°C for different levels of GO in the TOCNFs.

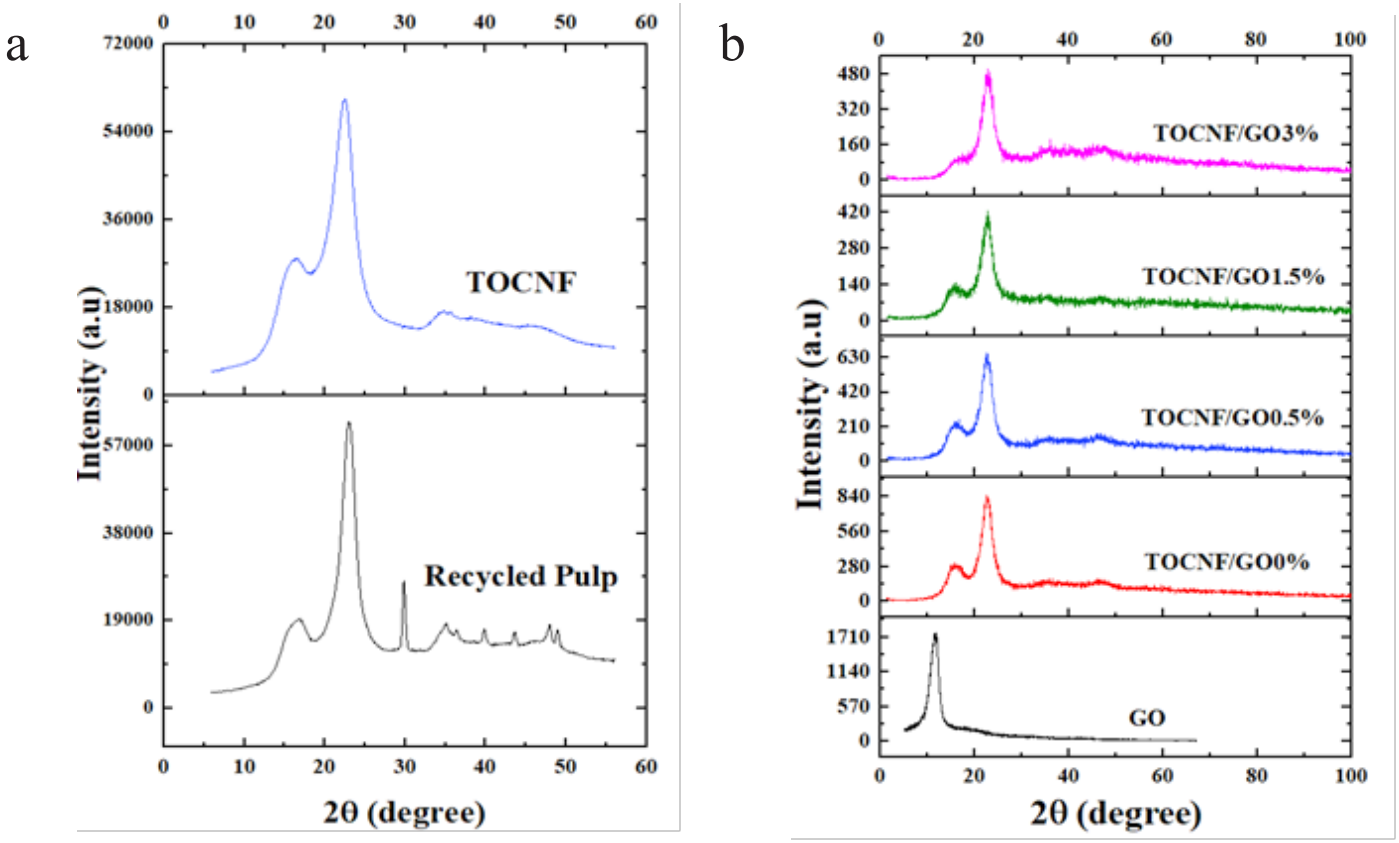

Figure 7. XRD patterns for recycled pulp and TOCNFs (a) and GO, TOCNFs/GO0%, TOCNFs/GO0.5%, TOCNFs/GO1.5%, and TOCNFs/GO3% (b).

observed. The absence of this peak may reflect its low content or possibly efficient exfoliation of GO (Han et al. 2011b) during TOCNFs/GO nanocomposites fabrication.

Morphological analysis

AFM and TEM images from the GO solution confirmed that the purchased GO was almost completely formed into single sheets in the aqueous suspension. Figure 8-a_1, a_2 shows the AFM image of GO and its corresponding height profile on a mica substrate. It shows single sheets of GO with diameters of several hundreds of nanometers and a thickness of 1.1 ± 0.2 nm. A carbon grid was submerged in an aqueous GO solution to create the TEM sample. Figure 8-b shows a TEM image of individual wrinkled GO sheets. Individual GO sheets are important for uniform dispersion in the base material of TOCNFs.

Figure 9a and 9b show FEG-SEM images of TOCNFs produced by TEMPO-oxidization followed by mechanical grinding treatment. SEM images of the cross-section of TOCNFs/GO nanocomposite films are shown in Figure 8c-j. SEM images were taken from the broken surface of samples after the tensile strength test. The fracture surface of the TOCNFs/GO0% film (Figure 9c and 9d) was uniform from the inside to the surface, which indicates a dense and homogeneous texture. However, the fracture surface for TOCNFs/GO 0.5% and TOCNFs/GO 1.5% nanocomposite films (Figure 9-e,f and 9-g,h, respectively) was rougher and without any accumulation of GO, which showed that the GO was uniformly distributed in the TOCNFs matrix. The link between the GO sheets and the TOCNFs was strong enough to allow tension to be transferred between the two components. Furthermore, while GO sheets and TOCNFs had adequate mechanical characteristics on their own, creating a link between them increased the qualities of the resultant composite (Luong et al. 2011). GO sheets and TOCNFs were uniformly mixed in TOCNFs/GO0.5% and TOCNFs/GO1.5% nanocomposite films, and a strong hydrogen bond formed among them. This bonding led to the improvement of mechanical properties of the films. On the other hand, the TOCNFs/GO3% film (Figure 9i and 9j) showed a high accumulation of GO and poor bonding between GO and TOCNFs. This agglomeration led to slippage of the GO sheets and resulted in the lack of stress transfer from the cellulose matrix to the GO sheets. Consequently, this significantly reduced the strengthening ability of the GO (He et al. 2012; B. Wang et al. 2012; Yadav et al. 2013).

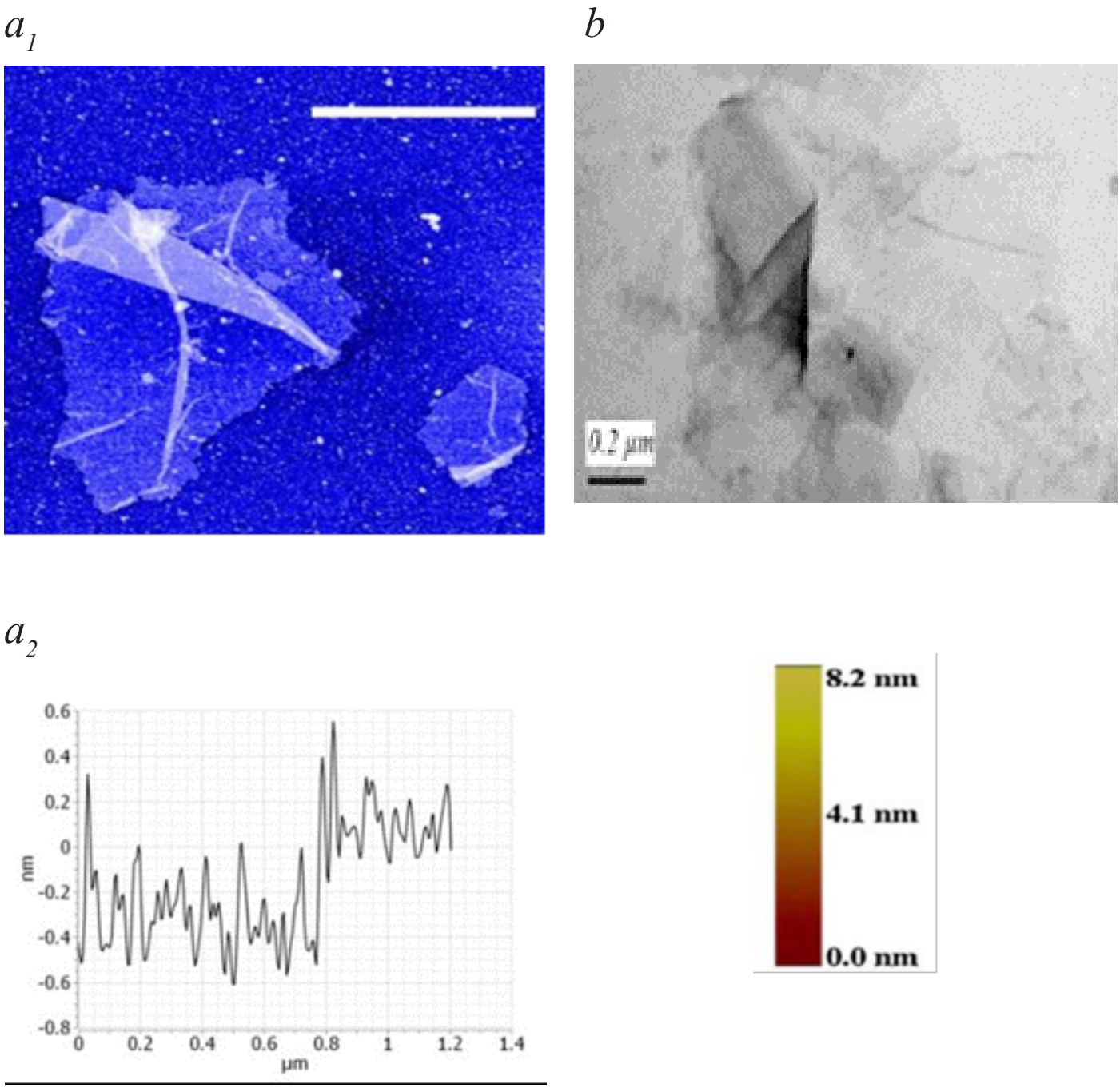

Figure 8. GO sheets shown by (a_1, a_2) AFM with a 1.4 µm scale bar and corresponding height profile and (b) TEM image showing the inclusions of GO sheets, scale bar = 0.2 µm.

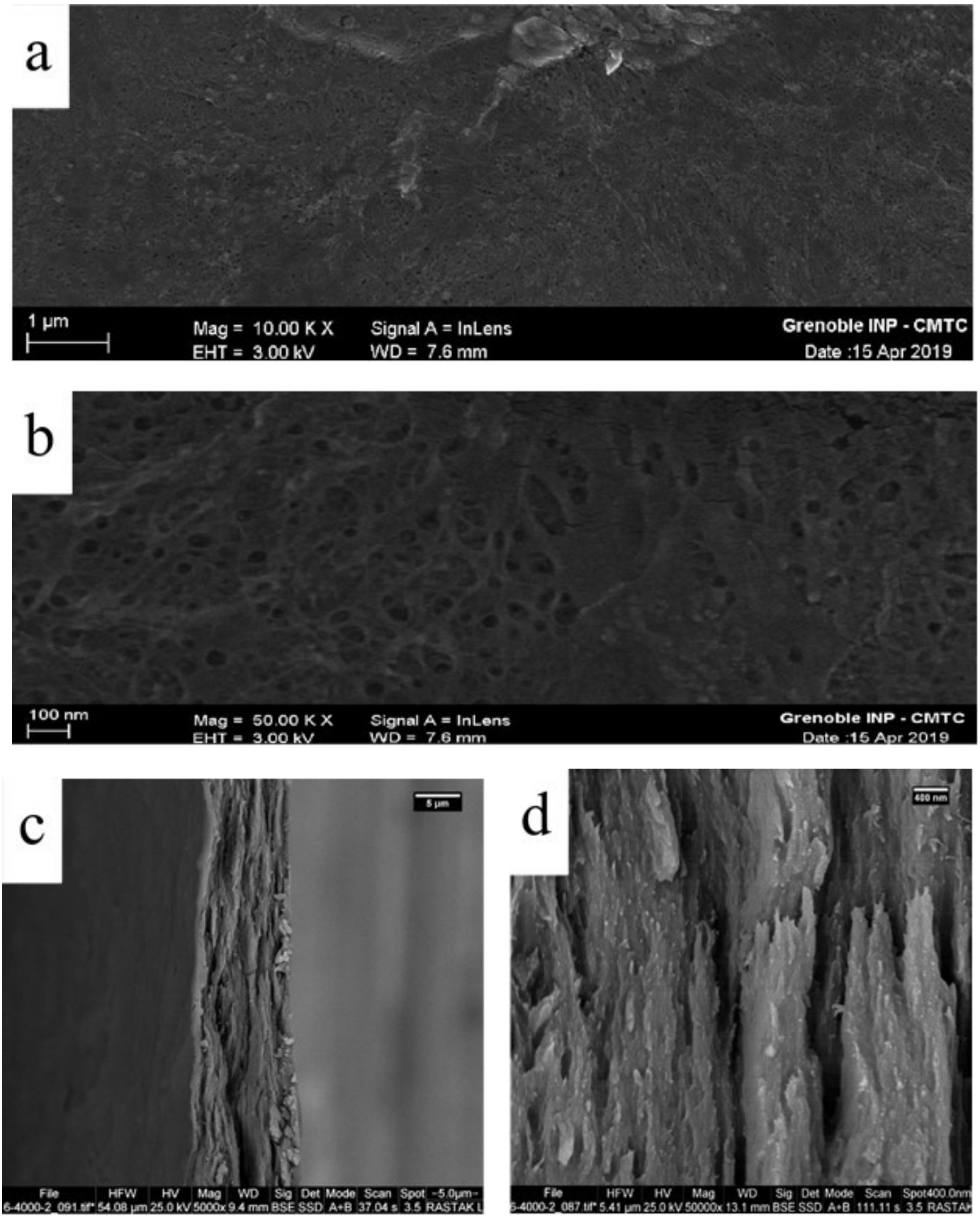

Figure 9. Low and high magnification FEG-SEM images for (a,b) TOCNFs and cross-section SEM images for (c,d) TOCNFs/GO0% composite films, (e,f) TOCNFs/GO0.5%, (g,h) TOCNFs/GO1.5% and (i,j) TOCNFs/GO3% [see following page].

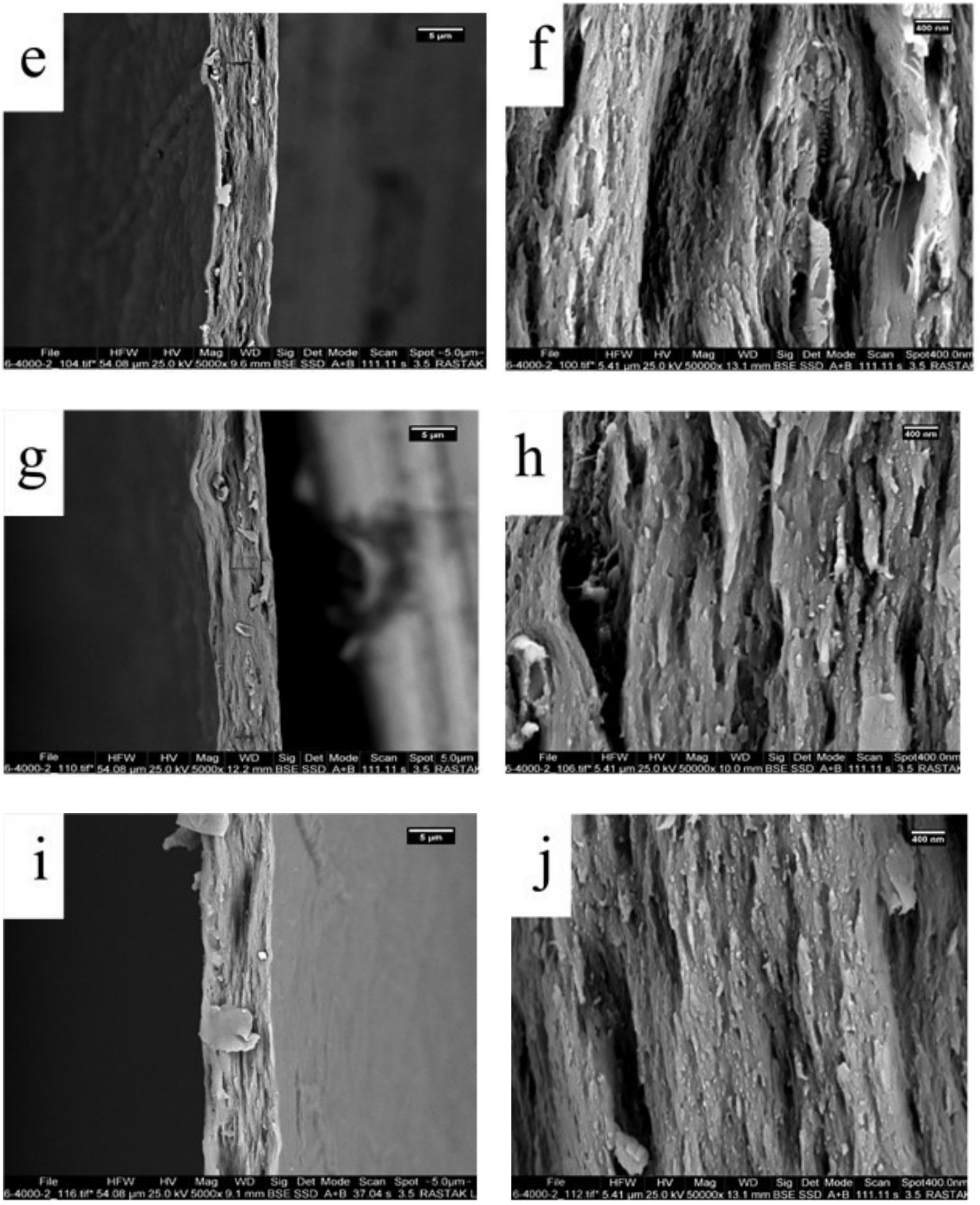

Figure 9 [continued]. Low and high magnification FEG-SEM images for (a,b) TOCNFs and cross-section SEM images for (c,d) TOCNFs/GO0% composite films, (e,f) TOCNFs/GO0.5%, (g,h) TOCNFs/GO1.5% and (i,j) TOCNFs/GO3% .

Conclusion

Nanocomposite films consisting of TOCNFs prepared from recycled pulp, and GO were synthesized via the solution molding method. Electrical conductivity titration and FTIR analysis confirmed that recycled pulp fibers, and cellulose nanofibers were successfully TEMPO-oxidized and the number of carboxyl groups increased. Integration of 1.5% GO resulted in 24% and 61% increases in average Young's modulus and average tensile strength of the TOCNFs/GO films, respectively, compared to a on amended film, but these differences were not significant. Addition of 3% GO resulted in 24% and 2% decreases in average Young's modulus and tensile strength of the TOCNFs/GO films, respectively. TGA results suggested that addition of up to 3% GO did not greatly affect the thermal stability of nanocomposite films. XRD spectrum showed that crystallinity of TOCNFs decreased from 83 to 65.5% compared to the recycled pulp. XRD spectrum of TOCNFs/GO nanocomposite films showed that the GO sheets were exfoliated in the TOCNFs matrix. SEM images illustrated reasonable dispersion of GO in the TOCNFs matrix of TOCNF/GO0.5% and TOCNF/GO1.5% films.

Acknowledgments

The authors would like to thank the Polytechnic Institute of Grenoble, France, and Mr. Naceur Belgacem, the institute's director, for providing the laboratory equipment to conduct the research.

References

Bardet R, Bras J, Belgacem N, Agut P, Dumas J (2014) Method for making paper. WO201411846. 21p.

Benhamou K, Dufresne A, Magnin A, Mortha G, Kaddami H (2014) Control of size and viscoelastic properties of nanofibrillated cellulose from palm tree by varying the TEMPO-mediated oxidation time. Carbohydr Polym 99:74–83.

Besbes I, Alila S, Boufi S (2011a) Nanofibrillated cellulose from TEMPO-oxidized eucalyptus fibres: effect of the carboxyl content. Carbohydr Polym 84(3):975–983.

Besbes I, Vilar MR, Boufi S (2011b) Nanofibrillated cellulose from alfa, eucalyptus and pine fibres: preparation, characteristics and reinforcing potential. Carbohydr Polym 86(3):1198–1206.

Brodin FW, Gregersen ØW, Syverud K (2014) Cellulose nanofibrils: challenges and possibilities as a paper additive or coating material–a review. Nord Pulp Pap Res J 29(1):156–166.

Coleman JN, Khan U, Blau WJ, Gun'ko YK (2006) Small but strong: a review of the mechanical properties of carbon nanotube–polymer composites. Carbon 44(9):1624–1652.

da Silva Perez D, Montanari S, Vignon MR (2003) TEMPO-mediated oxidation of cellulose III. Biomacromolecules 4(5):1417–1425.

Dubin S, Gilje S, Wang K, Tung VC, Cha K, Hall AS, Kaner RB (2010) A one-step, solvothermal reduction method for producing reduced graphene oxide dispersions in organic solvents. ACS Nano 4(7):3845–3852.

Fang M, Wang K, Lu H, Yang Y, Nutt S (2009) Covalent polymer functionalization of graphene nanosheets and mechanical properties of composites. J Mater Chem 19(38):7098–7105.

Feng Y, Zhang X, Shen Y, Yoshino K, Feng W (2012) A mechanically strong, flexible and conductive film based on bacterial cellulose/graphene nanocomposite. Carbohydr Polym 87(1):644–649.

Gontard N, Guilbert S, CUQ JL (1993) Water and glycerol as plasticizers affect mechanical and water vapor barrier properties of an edible wheat gluten film. J Food Sci 58(1):206–211.

Hagenmaier RD, Shaw PE (1990) Moisture permeability of edible films made with fatty acid and hydroxypropyl methyl cellulose. J Agric Food Chem 38(9):1799–1803.

Han D, Yan L, Chen W, Li W (2011a) Preparation of chitosan/graphene oxide composite film with enhanced mechanical strength in the wet state. Carbohydr Polym 83(2):653–658.

Han D, Yan L, Chen W, Li W, Bangal P (2011b) Cellulose/graphite oxide composite films with improved mechanical properties over a wide range of temperature. Carbohydr Polym 83(2):966–972.

He Y, Zhang N, Gong Q, Qiu H, Wang W, Liu Y, Gao J (2012) Alginate/graphene oxide fibers with enhanced mechanical strength prepared by wet spinning. Carbohydr Polym 88(3):1100-1108.

Hoeng F, Denneulin A, Bras J (2016) Use of nanocellulose in printed electronics: a review. Nanoscale 8(27):13131–13154.

Jorfi M, Foster EJ (2015) Recent advances in nanocellulose for biomedical applications. J Appl Polym Sci. 132(14).

Klemm D, Schmauder H, Heinze T, Vandamme E, Steinbuchel A (2002) Polysaccharides II. Polysaccharides from Eukaryotes. Biopolymers 6:275–287.

Lavoine N, Desloges I, Dufresne A, Bras J (2012) Microfibrillated cellulose–its barrier properties and applications in cellulosic materials: a review. Carbohydr Polym 90(2):735–764.

Li D, Müller MB, Gilje S, Kaner RB, Wallace GG (2008) Processable aqueous dispersions of graphene nanosheets. Nat Nanotechnol 3(2):101–105.

Li R, Liu C, Ma J (2011) Studies on the properties of graphene oxide-reinforced starch biocomposites. Carbohydr Polym 84(1):631–637.

Liang J, Huang Y, Zhang L, Wang Y, Ma Y, Guo T, Chen Y (2009) Molecular-level dispersion of graphene into poly(vinyl alcohol) and effective reinforcement of their nanocomposites. Adv Funct Mater 19(14):2297–2302.

Liao KH, Mittal A, Bose S, Leighton C, Mkhoyan KA, Macosko CW (2011) Aqueous only route toward graphene from graphite oxide. ACS Nano 5(2):1253–1258.

Luong ND, Pahimanolis N, Hippi U, Korhonen JT, Ruokolainen J, Johansson LS, Seppälä J (2011) Graphene/cellulose nanocomposite paper with high electrical and mechanical performances. J Mater Chem 21(36):13991–13998.

Maftoonazad N, Ramaswamy HS, Marcotte M (2008) Shelf-life extension of peaches through sodium alginate and methyl cellulose edible coatings. IJFST 43(6):951–957.

Mariano M, El Kissi N, Dufresne A (2014) Cellulose nanocrystals and related nanocomposites: review of some properties and challenges. J Polym Sci B Polym Phys 52(12):791–806.

Nechyporchuk O, Belgacem MN, Bras J (2016) Production of cellulose nanofibrils: a review of recent advances. Ind Crops Prod 93:2–25.

Oksman K, Aitomäki Y, Mathew AP, Siqueira G, Zhou Q, Butylina S, Hooshmand S (2016) Review of the recent developments in cellulose nanocomposite processing. Compos Part A Appl Sci Manuf 83:2–18.

Paquin, M, Loranger É, Hannaux V, Chabot B, Daneault C (2013) The use of Weissler method for scale-up a Kraft pulp oxidation by TEMPO-mediated system from a batch mode to a continuous flow-through sonoreactor. Ultrason Sonochem 20(1):103–108. doi:https://doi.org/10.1016/j.ultsonch.2012.08.007

Paredes JI, Villar-Rodil S, Martínez-Alonso A, Tascon JM (2008) Graphene oxide dispersions in organic solvents. Langmuir 24(19):10560-10564.

Park H, Weller C, Vergano P, Testin R (1993) Permeability and mechanical properties of cellulose-based edible films. J Food Sci 58(6):1361–1364.

Rana VK, Choi MC, Kong JY, Kim GY, Kim MJ, Kim SH . . . Ha CS (2011). Synthesis and drug-delivery behavior of chitosan-functionalized graphene oxide hybrid nanosheets. Macromol Mater Eng 296(2):131–140.

Rol F, Belgacem MN, Gandini A, Bras J (2019) Recent advances in surface-modified cellulose nanofibrils. Prog Polym Sci 88:241–264.

Saini S, Falco ÇY, Belgacem MN, Bras J (2016) Surface cationized cellulose nanofibrils for the production of contact active antimicrobial surfaces. Carbohydr Polym 135:239–247.

Saito T, Kimura S, Nishiyama Y, Isogai A (2007) Cellulose nanofibers prepared by TEMPO-mediated oxidation of native cellulose. Biomacromolecules 8(8):2485–2491.

Salavagione HJ, Gomez MA, Martínez G (2009) Polymeric modification of graphene through esterification of graphite oxide and poly (vinyl alcohol). Macromolecules 42(17):6331–6334.

Segal L, Creely JJ, Martin Jr A, Conrad C (1959) An empirical method for estimating the degree of crystallinity of native cellulose using the X-ray diffractometer. Text Res J 29(10):786–794.

Sellinger A, Weiss PM, Nguyen A, Lu Y, Assink RA, Gong W, Brinker CJ (1998) Continuous self-assembly of organic–inorganic nanocomposite coatings that mimic nacre. Nature 394(6690):256–260.

Steurer P, Wissert R, Thomann R, Mülhaupt R (2009) Functionalized graphenes and thermoplastic nanocomposites based upon expanded graphite oxide. Macromol Rapid Commun 30(4-5):316–327.

Turbak, AF, Snyder FW, Sandberg KR (1983) Microfibrillated cellulose, a new cellulose product: properties, uses, and commercial potential. Paper presented at the J Appl Polym Sci Appl Polym Symp.

Villar-Rodil S, Paredes JI, Martínez-Alonso A, Tascón JM (2009) Preparation of graphene dispersions and graphene-polymer composites in organic media. J Mater Chem 19(22):3591–3593.

Wang B, Lou W, Wang X, Hao J (2012) Relationship between dispersion state and reinforcement effect of graphene oxide in microcrystalline cellulose–graphene oxide composite films. J Mater Chem 22(25):12859–12866.

Wang S-F, Shen L, Zhang W-D, Tong Y-J (2005) Preparation and mechanical properties of chitosan/carbon nanotubes composites. Biomacromolecules 6(6):3067–3072.

Wang S, Gang L, Pu J (2018) Enhancement of the strength of biocomposite films via graphene oxide modification. BioResources 13:6311–6321.

Wu X, Liu P (2010) Facile preparation and characterization of graphene nanosheets/polystyrene composites. Macromol Res 18:1008–1012.

Xu C, Wang G, Xing C, Matuana LM, Zhou H (2015) Effect of graphene oxide treatment on the properties of cellulose nanofibril films made of banana petiole fibers. BioResources 10(2).

Xu J, Wang K, Zu S-Z, Han B-H, Wei Z (2010). Hierarchical nanocomposites of polyaniline nanowire arrays on graphene oxide sheets with synergistic effect for energy storage. ACS Nano 4(9):5019–5026.

Yadav M, Rhee K, Jung I, Park S (2013) Eco-friendly synthesis, characterization and properties of a sodium carboxymethyl cellulose/graphene oxide nanocomposite film. Cellulose 20:687–698.

Yang L, Paulson A (2000) Effects of lipids on mechanical and moisture barrier properties of edible gellan film. Food Res Int 33(7):571–578.

Yang X, Tu Y, Li L, Shang S, Tao X-m (2010) Well-dispersed chitosan/graphene oxide nanocomposites. ACS Appl Mater Interfaces 2(6):1707–1713.

Evaluation of connection performance of various mixed species CLTs for furniture-style joinery

Chih-Cheng Chen†
Ph.D. Candidate
Department of Forestry and Natural Resources
Purdue University
West Lafayette, IN 47906
E-mail: chen3871@purdue.edu

Daniel P. Hindman†
Associate Professor
Department of Sustainable Biomaterials
Virginia Tech
1650 Research Center Dr.
Blacksburg, VA, 24061
E-mail: dhindman@vt.edu

Henry J. Quesada†
Professor
E-mail: quesada@purdue.edu

Ting-Ho Tsai
Master's Student
E-mail: tsai181@purdue.edu

*Eva Haviarova**†
Professor
Department of Forestry and Natural Resources
Purdue University
West Lafayette, IN 47906
E-mail: ehaviar@purdue.edu

(Received 24 September 2024)

Abstract. This study investigated the connection performance of various mixed-species cross-laminated timber (CLT) panels used in furniture-style joinery. A combination of yellow-poplar and southern pine were used to assesses the mechanical performance of L-shaped dowel and lap joints under compression and tension loads. Mechanical testing was conducted to evaluate the connection moment resistance of each joint configuration. Dowel joints generally exhibited higher connection moment resistance, particularly under compression, which was attributed to superior mechanical interlocking and load distribution. Conversely, lap joints demonstrated higher variability in performance, with some configurations showing inconsistency, particularly under tension. Failure modes, such as delamination and rolling shear, were observed, highlighting the need for improved adhesion and joint design. These findings suggest that dowel joints are the preferred joinery method due to higher compressive strength. In contrast, lap joints may benefit from optimization in adhesive bonding techniques to enhance performance under tension. This research provides valuable insights into the structural integrity and durability of CLT joinery, guiding future improvements in design and application for engineered wood products.

Keywords: Mixed species CLTs, Furniture joinery, Joinery performance, Joint strength

Introduction

The growing demand for timber in cross-laminated timber (CLT) construction necessitates sustainable resource management strategies. Utilizing materials efficiently during CLT processing and from deconstructed CLT buildings offers compelling end-of-life solutions (for example, the production of CLT furniture). This approach directly addresses the principles of the circular economy by ensuring materials are repurposed or recycled at the end of their lifecycle. While first-generation CLT buildings rarely require dismantling and planning for their eventual decommissioning, recycling is essential for maintaining environmental responsibility and circular economy principles. Recycling these materials minimizes waste and reduces the built environment's carbon footprint (Chúláin et al. 2023).

* Corresponding author
† Society of Wood Science & Technology member

CLT is typically manufactured from softwood species (Sciomenta et al. 2021), but with the increase in consumption of softwood lumber, incorporating hardwood lumber into CLT production could present a valuable opportunity for the construction industry (Adhikari et al. 2020). Hardwoods are finding new applications in mass timber due to their density and high mechanical strength, and some manufacturers view hardwood CLT as a new market opportunity (Hassler et al. 2022; Thomas and Buehlmann 2017). Da Rosa Azambuja et al. (2022) focused on the potential of utilizing low-grade yellow-poplar (*Liriodendron tulipifera*) lumber for CLT production. NHLA-graded No. 2A and below-grade yellow-poplar lumber were evaluated for structural suitability in CLT panels. Results suggested that a significant portion of low-grade yellow-poplar lumber regraded for structural use, met or exceeded the required grade values for CLT production, offering the potential to enhance CLT manufacturing with cost-effective, reclaimed feedstock. Similarly, Ma et al. (2021) studied the performance of hybrid CLT panels combining sugar maple (*Acer saccharum*) and white spruce (*Picea glauca*) bonded with melamine adhesive. The findings indicated that sugar maple improved bending strength, with notable shear properties. This hybrid CLT met PRG-320 mechanical standards and offered enhanced structural capabilities.

Incorporating CLT (softwood, hardwood, or hybrid) into furniture products represents an innovative approach that enhances the durability and functionality of wooden structures. This technique exploits the structural benefits of CLT, such as its dimensional stability and load-bearing capacity, which surpass those of traditional wood products. By utilizing the inherent strengths of CLT, furniture designers can create robust, long-lasting, and environmentally friendly furniture due to CLT's ability to be sourced from sustainable forestry practices. Furthermore, the flexibility of CLT allows for innovative design choices, such as integrating cutouts from CLT construction projects like windows and door openings into unique furniture products or repurposing leftover CLT materials, thereby promoting a circular economy. The potential for recycling CLT also contributes to environmental sustainability, making it a compelling choice for modern furniture design.

This integrated process is facilitated by computer numerical control (CNC) technology, where building smaller products from recycled CLT panels (new or old) could be a simple design process. CNC machines enable complex cuts and patterns, significantly simplifying the design process while ensuring minimal material waste and promoting sustainable practices. However, despite the design flexibility and waste reduction benefits offered by CNC, the structural integrity of CLT joinery is also critical. Addressing this ensures the development of durable and stronger products, thereby maximizing the functional and environmental benefits of CNC-facilitated CLT applications in furniture design. As noted by Eckelman (2003), joints in furniture are common points of failure. The durability of furniture, particularly plate construction type furniture, largely depends on the strength of corner joints (Altinok et al. 2009). Material selection, joint strength, and end-use are crucial in determining joinery methods, affecting the longevity and performance of the structure (Nicholls and Crisan 2002). Standard techniques like butt and miter joints, alongside dowels, a favored fastener for ease and strength, are integral to the quality of wooden furniture (Altinok et al. 2009; Chen and Lyu 2018; Maleki et al. 2012).

This investigation focused on measuring the structural performance of different furniture-style joints using CLT panels made from repurposed recycled/salvaged yellow-poplar (*Liriodendron tulipifera*) and southern pine (*Pinus* spp.). The study assessed the connection moment resistance of lap and dowel joinery in compression and tension and explored the potential of various complex joinery types. The research analyzed the strength and stiffness of variable hybrid CLT joints and observed their failure modes. The findings were expected to validate the practicality of utilizing recycled/salvaged CLT materials for robust furniture and to innovate stronger and more durable joinery methods for other engineered wood products.

Materials and methods

The specimens utilized in this study, sourced from Satir et al. (2024), were constructed from salvaged CLTs made of yellow-poplar (*Liriodendron tulipifera*) and southern pine (*Pinus* spp.), with undamaged portions cut to size after prior bending and shear tests. Three types of CLT were examined: entirely yellow-poplar (YYY), hybrid panels with yellow-poplar face layers and southern pine cores (YPY), and hybrid panels with southern pine outer layers and yellow-poplar cores (PYP). All CLT panels were produced at Texas CLT (Magnolia, AR). The manufacturing process involved nominal 2 x 6 pieces, planed to a width of 34.9 mm. Number 2 southern pine lumber was obtained on-site at Texas CLT, while yellow-poplar lumber, upgraded from No. 2 Common to at least No. 2 yellow-poplar, was sourced from various sawmills in Virginia and transported to the production facility. The CLT panels were face-glued using a one-component polyurethane adhesive and assembled in a cold press for 60 min under a pressure of 620 kPa.

Yellow-poplar (*Liriodendron tulipifera*) dowels sourced from Madison Mill Co (Ashland City, TN) were employed in the

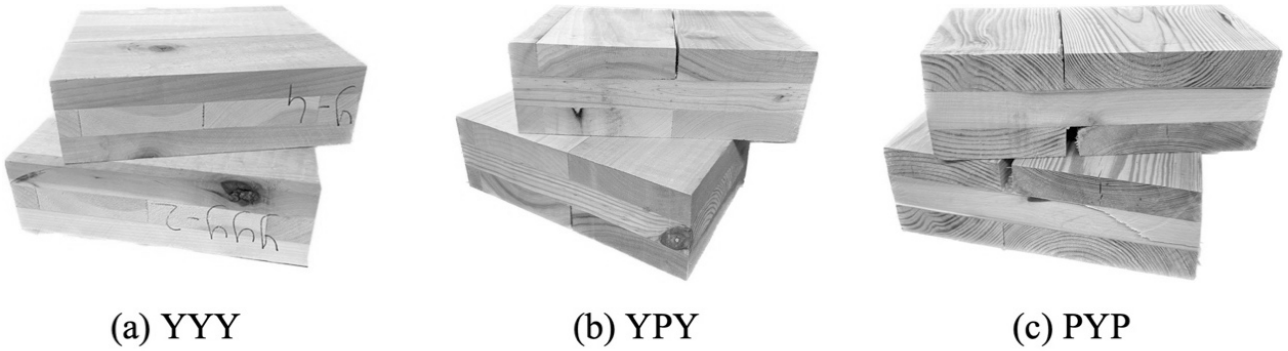

Figure 1. Examples of CLTs composed of yellow-poplar (Y) or southern pine (P).

construction of dowel joints. These 19.05 mm plain dowels featured a straight grain pattern that offered dimensional stability, with chamfering on both ends to facilitate easy insertion and secure fit in the drilled holes. For adhesive, Titebond III wood glue (Franklin International, Columbus, OH) was utilized, characterized by a solid content of 48-52% and a viscosity of 4200 cps. This waterproof adhesive is known for its strong, permanent bond suitable for woodworking, with a longer open time allowing adjustments during assembly. It is recommended to be spread at a rate of 6.1335 m²/L, ensuring adequate coverage. All specimens were clamped for a minimum of 24 h post-assembly to allow for complete curing.

Selected Joinery and Construction

The experimental design incorporated L-shaped lap and dowel joints, as depicted in Figure 2. The lap joint, a prevalent choice in woodworking due to its strength and ease of fabrication, was precisely crafted using computer numerical control (CNC) machinery. The lap joint consisted of a face member measuring 304.8 × 304.8 × 101.6 mm and a butt member measuring 254.0 × 304.8 × 101.6 mm. Each member was machined with a corresponding 50.8 mm deep notch, resulting in a precisely mated, flush connection when assembled. The joint was then secured with clamps for at least 24 h after adhesive application to ensure a durable bond.

Similarly, the dowel joint assembly involved a face and a butt members, measuring 304.8 × 304.8 × 101.6 mm and 203.2 × 304.8 × 101.6 mm, respectively, both constructed from the same CLT material. A three-dowel system was used in this study to construct the corner joints because it is widely employed in the construction of bookcases and cabinets. This design choice aligns with the recommendations of Zhang and Eckelman (1993), who demonstrated that spacing dowels 76.2 mm apart optimized joint strength in multi-dowel assemblies. The dowels utilized in this study were 19.05 mm in diameter, selected for their ability to provide adequate dimensional stability within the joint. To accommodate potential variations in dowel size and facilitate the application of adhesive, the corresponding holes in both the face and butt members were drilled slightly larger, with a diameter of approximately 20.64 mm. This provided a clearance of 1.6 mm, ensuring a precise fit. Additionally, the

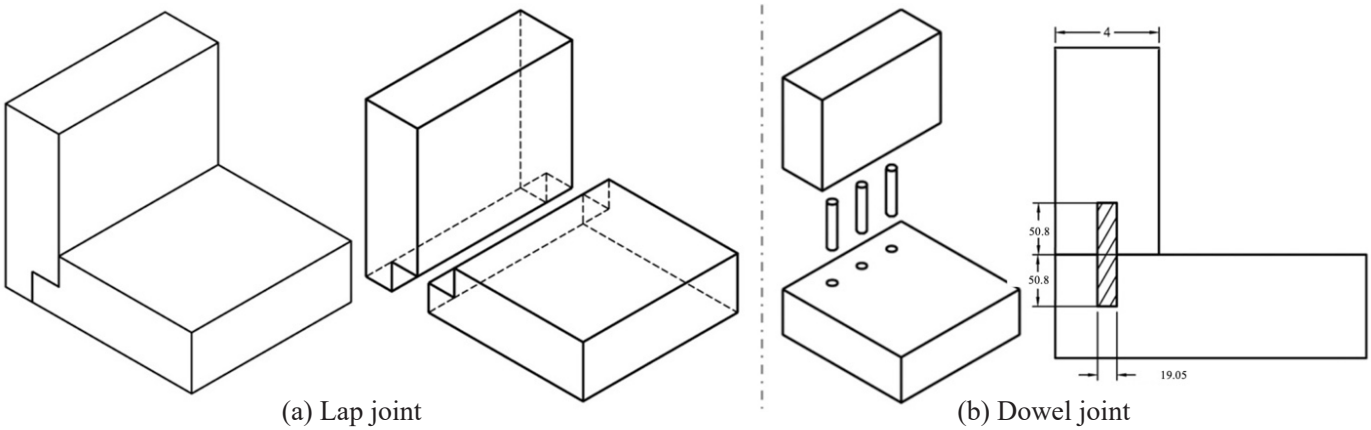

Figure 2. Selected joinery for CLT connections.

depth of each hole was maintained at 50.8 mm, a measurement chosen to guarantee sufficient engagement of the dowels, thereby enhancing the robustness of the connection.

Test procedure

L-shape corner joint test

To comprehensively understand the mechanical behavior of L-shaped joinery specimens, specimens were subjected to both compression and tension load tests. Specifically, the moment resistances of cross-laminated timber (CLT) joints were assessed under loads that applied a closing force, known as compression moments, at point A and loads that applied an opening force, referred to as tension moments, at point B in Figure 3. This approach was essential, as corner joints experience both compression moment and tension moment loading configurations when case furniture was subjected to lateral loading. Evaluating the performance under these distinct loading conditions ensured that the findings were applicable to a variety of practical scenarios where these joints may be employed.

Thirty-six CLT corner joint specimens were tested, with eighteen subjected to compression and the other eighteen to tension. These specimens were evaluated for connection moment resistance using an MTS universal testing machine (MTS Systems Corp., Minneapolis, MN, USA). The loading configurations for testing joint moment resistances to closing and opening action forces are shown in Figure 4. The L-shaped specimens were secured to a robust, heavy metal base using bolts and nuts for stability, with a bar clamp employed to prevent base movement and restrict displacement of the vertical member. Specimens were constructed using the three types of CLTs, identified as YYY, YPY, and PYP, and were tested as both lap and dowel joints. Each specimen was subjected to a constant displacement rate of 1.27 mm/min to determine the maximum load capacity before failure.

In both compression and tension bending tests, the connection moment resistance of CLT joinery was determined by multiplying the ultimate failure load (F) by the moment arm, representing the distance from the loading head to the CLT joint face. A 215.9 mm moment arm was utilized for YYY and YPY specimens, while PYP specimens used a 165.1 mm arm, allowing for a thorough assessment of the bending performance across different configurations.

$$\mathrm{M}\ (N\text{-}mm) = \mathrm{F}\ (N) \times \mathrm{L}\ (mm) \qquad (1)$$

where M is connection moment resistance, *N·mm*; F is applied load, *N*; and L is moment arm, *mm*.

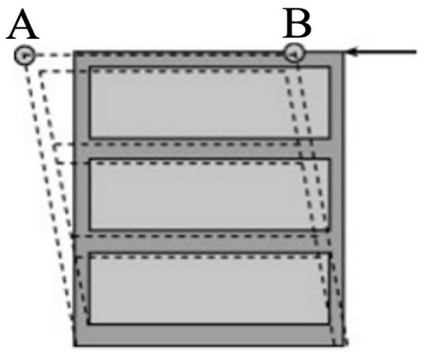

Figure 3. A typical case-type construction loaded by a vertical force (adapted from Çetin Yerlikaya and Aktaş, 2012).

Corner joint failure behavior of CLT

Failure modes of CLT corner joint specimens were assessed through mechanical testing of dowel and lap joint configurations. Failure mechanisms were categorized as material glue failure (MGF), joint glue failure (JGF), rolling shear (RS), and wood failure (WF) based on visual inspection and digital analysis. High-resolution imaging was used to document failure characteristics, and the extent of each failure type was estimated through a manual visual assessment as a percentage of the total failure area for comparative analysis. The failure percentage of each joint specimen was then correlated with connection moment resistance, and the results were compiled into a single figure to facilitate direct comparison.

Descriptive statistics

Each test variable was limited to three repetitions due to the restricted availability of CLT materials, which were donated by Virginia Tech as leftover CLT specimens from their previous experiments. CLT thickness, measuring 101.6 mm (4 in), represented the maximum that could be processed given the constraints of the laboratory's CNC machining capabilities. Additionally, issues such as delamination occurred during specimen preparation due to the limited and inconsistent quality of the material, which further reduced the number of usable specimens. As a result, this study employed descriptive statistics to analyze the data, presenting differences between groups as percentages and discussing the range of values, including the maximum and minimum observed in each combination.

Results and discussion

Delamination was observed during the CNC machining of the PYP CLT. Additionally, limitations in the available CLT inventory necessitated using smaller specimen sizes (Table 1). This constraint required an adjustment in calculating the

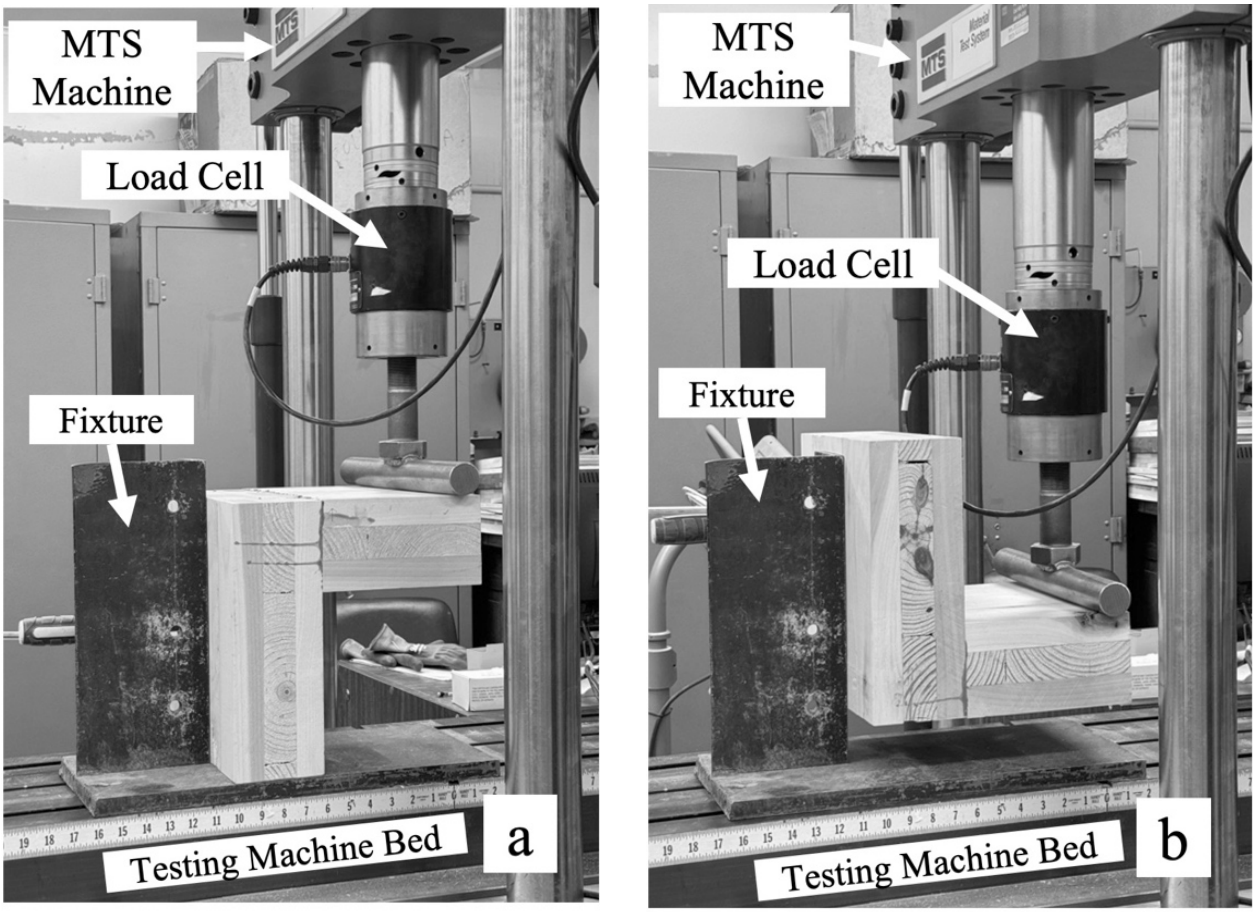

Figure 4. Method of loading the L-shape corner joint under compression (a) and tension moments (b).

Table 1. Specification of L-shaped joint specimens.

Load	Species	Specific gravity	Joint type	Face member dimension (L × W × T)	Butt member dimension (L × W × T)	Number of specimens tested
Compression	YYY	0.493	Lap	304.8 × 304.8 × 101.6	254.0 × 304.8 × 101.6	3
			Dowel	304.8 × 304.8 × 101.6	203.2 × 304.8 × 101.6	
	YPY	0.497	Lap	304.8 × 304.8 × 101.6	254.0 × 304.8 × 101.6	3
			Dowel	304.8 × 304.8 × 101.6	203.2 × 304.8 × 101.6	
	PYP	0.483	Lap	254.0 × 304.8 × 101.6	203.2 × 304.8 × 101.6	3
			Dowel	254.0 × 304.8 × 101.6	152.4 × 304.8 × 101.6	
Tension	YYY	0.493	Lap	304.8 × 304.8 × 101.6	254.0 × 304.8 × 101.6	3
			Dowel	304.8 × 304.8 × 101.6	203.2 × 304.8 × 101.6	
	YPY	0.497	Lap	304.8 × 304.8 × 101.6	254.0 × 304.8 × 101.6	3
			Dowel	304.8 × 304.8 × 101.6	203.2 × 304.8 × 101.6	
	PYP	0.483	Lap	254.0 × 304.8 × 101.6	203.2 × 304.8 × 101.6	3
			Dowel	254.0 × 304.8 × 101.6	152.4 × 304.8 × 101.6	

Note: Y: Yellow-poplar, P: Southern pine; Specific gravity unit: kg/m^3; Member unit: mm

connection moment resistance, with the moment arm reduced from 215.9 mm to 165.1 mm.

Table 2 presents the average connection moment resistance and coefficient of variation (COV) of the L-shaped joints under compression and tension, considering various corner joint configurations. Among the three CLTs tested, the dowel joint configuration often exhibited a higher connection moment resistance than the lap joint configuration. However, this trend was not consistent across all species and loading conditions. YYY dowel joints subjected to a compression moment had

Table 2. Average connection moment resistance of L-shaped joints.

	Joinery	YYY	YPY	PYP
Average connection moment — Compression, N·mm (COV)	Dowel	4560 (12.2%)	5170 (9.27%)	3610 (9.39%)
	Lap	4660 (28.1%)	2930 (14.7%)	2850 (9.82%)
Average connection moment — Tension, N·mm (COV)	Dowel	3070 (5.28%)	3250 (16.0%)	2780 (11.2%)
	Lap	3190 (15.2%)	2980 (16.3%)	1840 (17.1%)

Note: Y: Yellow-poplar, P: Southern pine; COV: Coefficient of Variation

a connection resistance of 4560 N·mm, approximately 1.6% lower than the lap joint capacity of 4660 N·mm. Tension test results indicated a different pattern, where the lap joint was 4.1% greater (3190 N·mm) than the dowel joint (3070 N·mm).

The YPY dowel joint configuration in compression produced a higher connection moment resistance of 5170 N·mm, 76.6% higher than the lap joint's capacity of 2930 N·mm. Conversely, the difference between the dowel and lap joints in tension was minimal, with the dowel joint showing only a 9.4% higher capacity (3250 N·mm) than the lap joint (2980 N·mm).

The PYP dowel joint configuration in compression showed a 26.7% higher connection moment resistance (3610 N·mm) than the lap joint (2850 N·mm). However, in tension, the lap joint displayed a capacity 34% lower (1840 N·mm) than the dowel joint (2780 N·mm).

The variability across different species and loading conditions indicated that while dowel joints tended to offer higher moment resistance, the differences were not uniform and can vary markedly depending on the specific configuration and material properties. Additionally, the YYY species lap joint demonstrated substantial variability under compression, with a high coefficient of variation (28.1%), indicating an inconsistent response, which may be attributed to the quality of the raw CLT materials. This variability could be linked to the bonding quality issues in the materials, as highlighted by Mohamadzadeh and Hindman (2015), who suggested that yellow-poplar CLT's inherent strength might lead to adhesive rather than wood failure under shear loads, underscoring the importance of bonding quality in joint integrity.

The average connection moment results indicated that the compression moment values of the L-shaped joint generally exceeded those observed in tension (Figure 5), which is consistent with the inherent mechanical behavior of wood. Wood typically exhibits higher strength in compression, particularly along the grain, due to the thin-walled cells undergoing lateral compression when a load is applied perpendicular to the grain. This process leads to the gradual cell collapse under increasing stress until the fibers are entirely crushed, after which the load can still increase (Karacabeyli et al. 2013; Ali et al. 2014). In contrast, the tensile strength of wood is limited by the capacity of individual cell walls to resist separation under tension. The higher connection moment resistance observed in the dowel joint configuration, as compared to the lap joint configuration, can be attributed to the superior interlocking and mechanical support provided by the dowels. Mechanical support refers to the dowels embedding tightly into the wood fibers with adhesives, which enhances load transfer and joint stability while minimizing movement under load. Additionally, the use of three dowels in our tests facilitated even load distribution across the CLTs, thereby reducing the likelihood of localized stress concentrations that could lead to failure.

Connection moment resistance values for the different joinery types and species demonstrated notable variations (Table 3). Under compression, the YPY dowel joint configuration exhibited the greatest connection moment resistance at 5170 N·mm, 52% above the average value across all 36 specimens. Similarly, the YYY dowel joint under compression also showed a greater connection moment resistance, with a

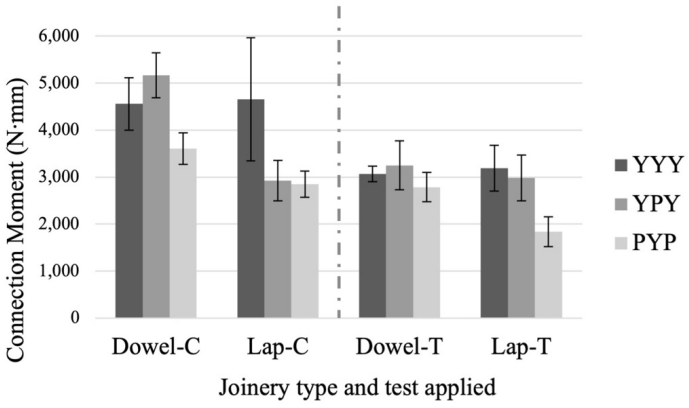

Figure 5. Average connection moment resistance of corner joints in compression and tension tests.

Table 3. Connection Moment Resistance, Coefficient of Variation, and Percentage Differences for L-Shaped Joints.

Joint type	Load	Species	Avg. Connection Moment Resistance, N-mm	COV (%)	% Difference (from Avg.)
Dowel	Compression	YYY	4560	12.2	33.8
Dowel	Compression	YPY	5170	9.27	51.7
Dowel	Compression	PYP	3610	9.39	5.86
Lap	Compression	YYY	4660	28.1	36.7
Lap	Compression	YPY	2930	14.7	-14.1
Lap	Compression	PYP	2850	9.82	-16.4
Dowel	Tension	YYY	3070	5.28	-9.95
Dowel	Tension	YPY	3250	16.0	-4.60
Dowel	Tension	PYP	2780	11.2	-18.2
Lap	Tension	YYY	3190	15.2	-6.26
Lap	Tension	YPY	2980	16.3	-12.4
Lap	Tension	PYP	1840	17.1	-46.1

Note: Y: Yellow-poplar, P: Southern pine; Unit: mm

value of 4560 N·mm, representing a 34% increase from the average. In contrast, the YPY lap joint configuration under compression showed a lower connection moment resistance of 2930 N·mm, 14% below the average. The PYP dowel joint under compression, while showing a relatively moderate connection moment resistance of 3610 N·mm, was 6% above the average. Overall, the dowel joints generally exhibited greater connection moment resistance than the lap joints, with a few exceptions depending on the species and load type. The variability in connection moment resistance, as reflected by the coefficient of variation (COV), also indicated differences in material behavior and joint performance, particularly in the lap joint configurations, which exhibited higher COV values than the dowel joints.

Figures 6(a) through 6(h) illustrate the stiffness characteristics of the evaluated joints, detailing the relationship between applied load and the resulting deflection. The data revealed a non-linear correlation, suggesting that joint failure occurred beyond the linear elastic range. The joints generally exhibited greater strength under compression moment compared to tension moment loading. Figures 6(a), 6(c), 6(e), and 6(g) present segments of the load-deflection curves from Figures 6(b), 6(d), 6(f), and 6(h), focusing on the linear elastic range for deflections not exceeding 7.62 mm for comparison.

No clear trend in stiffness was observed in Figure 6(a); however, the second specimen constructed with a PYP dowel joint (PYPDC2) showed the lowest initial slope, indicating potential weakness. Interestingly, slope increased when deflection reached approximately 3 mm, unexpectedly maintaining strength levels. Figure 6c offered a more explicit depiction of strength variations, with YPYDT1 predicted to have the highest strength while PYPDT2 appeared to be the weakest. Nonetheless, YPYDT1 experienced a decrease in strength and eventual failure at a deflection of 8.9 mm (Figure 6(d)), primarily due to the dowel being pulled out from the specimen, indicating a critical failure mode.

Specimen YPYLC2 exhibited a reduction in slope beginning at a deflection of 3.8 mm, which continues until failure (Figure 6(e)). Although this specimen did not demonstrate exceptionally high strength, as corroborated by Figure 6(f), the main damage to YPYLC2 occurred in the core layer of the CLT material, with a distinctive split along the growth rings. Figure 6(f) also highlights that YYYLC1 displayed relatively higher strength than other specimens.

Specimen PYPLT1 experienced a reduction in strength starting at a deflection of 6.35 mm, indicating a weakening of material integrity (Figure 6(g)), which was further evidenced in Figure 6(h). PYPLT1 exhibited substantial weakness, primarily due to the delamination of the CLT material shortly after initial loading. This analysis emphasized the importance of considering both mechanical properties and failure modes when assessing the performance of CLT joints under various loading conditions.

Failure Modes Analysis

The observed failure mechanisms were categorized into four types, as outlined in the methodology. Material glue failure

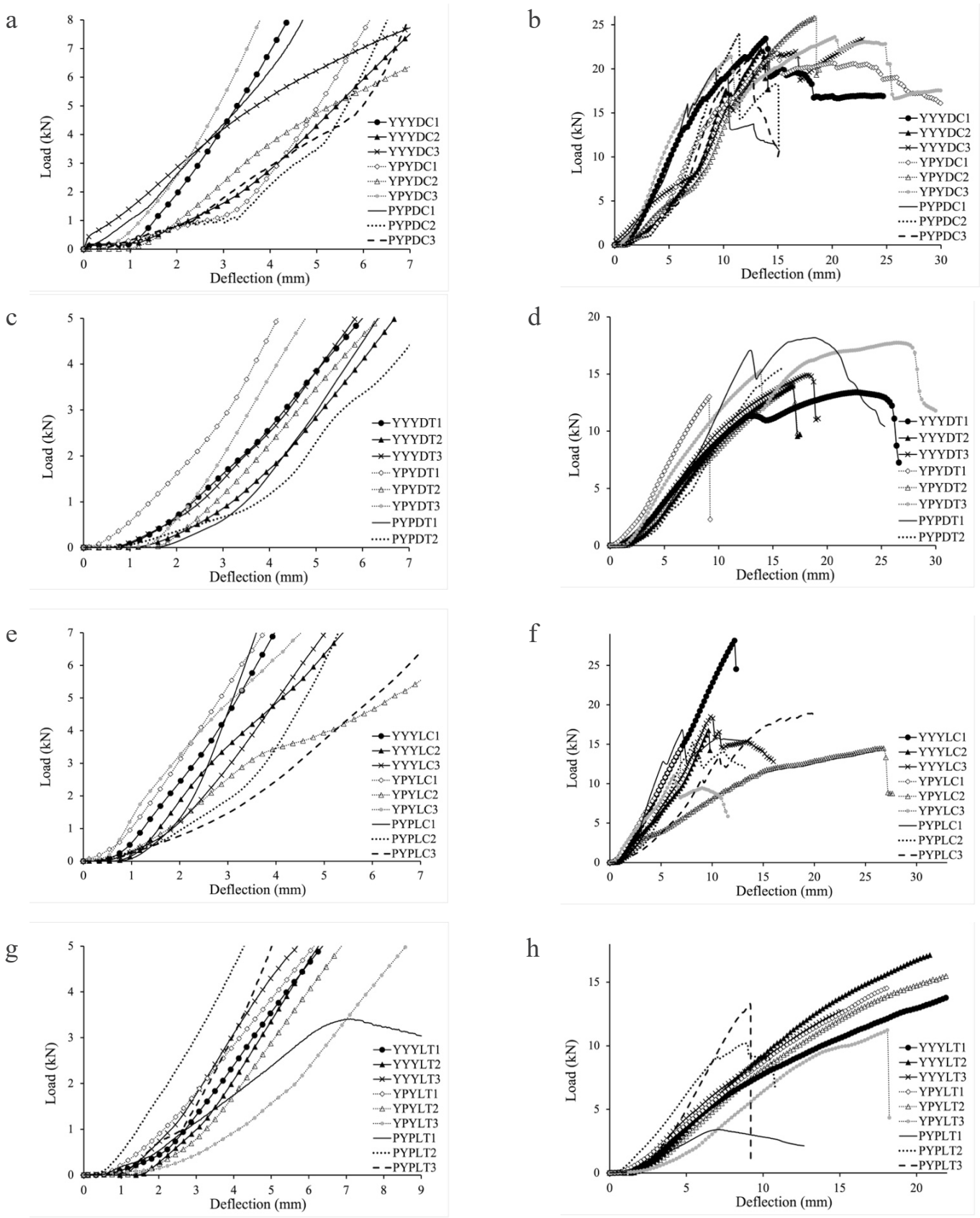

Figure 6. Load deflection curves of joints tested in: (a) compression with dowel in linear-elastic range; (b) compression with dowel in entire range; (c) tension with dowel in linear-elastic range; (d) tension with dowel in entire range; (e) compression with lap in linear-elastic range; (f) compression with lap in entire range; (g) tension with lap in linear-elastic range; (h) and tension with lap in in entire range.

(MGF) refers to delamination caused by adhesive failure between CLT layers, resulting in layer separation. Joint glue failure (JGF) occurred within the glue line at the joint interface and included instances where dowels were pulled out due to insufficient bonding. Rolling shear (RS) is commonly observed in the core layers of CLT and involves shear failure caused by the rolling action of wood fibers under stress. Wood failure (WF) was defined as the physical breakage of wood fibers and layers when the material exceeded its mechanical limits. The findings emphasize the prevalence of delamination and rolling shear failures, particularly within the core layers of CLT materials, highlighting the necessity for improvements in adhesive bonding techniques when fabricating CLT, particularly in lap joints, to enhance the structural integrity and durability of CLT assemblies under various stress conditions.

Figure 7 illustrates the characteristic failure modes observed in the tested CLT dowel and lap specimens. Dowel joints primarily exhibited failure modes characterized by the extraction of the dowel (Figure 7(e)), leading to reduced in strength and subsequent failure. In contrast, lap joints demonstrated a range of failure modes, including JGF, RS, and WF. Detailed descriptions of specific failure scenarios include dowel joint failures under compression (Figure 7(b)), and under tension (Figure 7(e)). Figures 7(c) and 7(f) show the lap joint failures under compression and tension. Notably, Figure 7(b) highlights a distinct instance of rolling shear failure shown by the marked circles. RS is a phenomenon particularly characteristic of CLT materials, which demonstrates the unique structural challenges posed by this type of construction material.

A comparative assessment of failure distribution quantified the occurrence of each failure mechanism. Figure 8 presented the failure distribution as percentages, with trend lines depicting structural patterns, providing a graphical representation for assessing the structural integrity of various CLT configurations. The result in Figure 8 indicated that a high proportion of specimens exhibited MGF and JGF, with approximately 20-

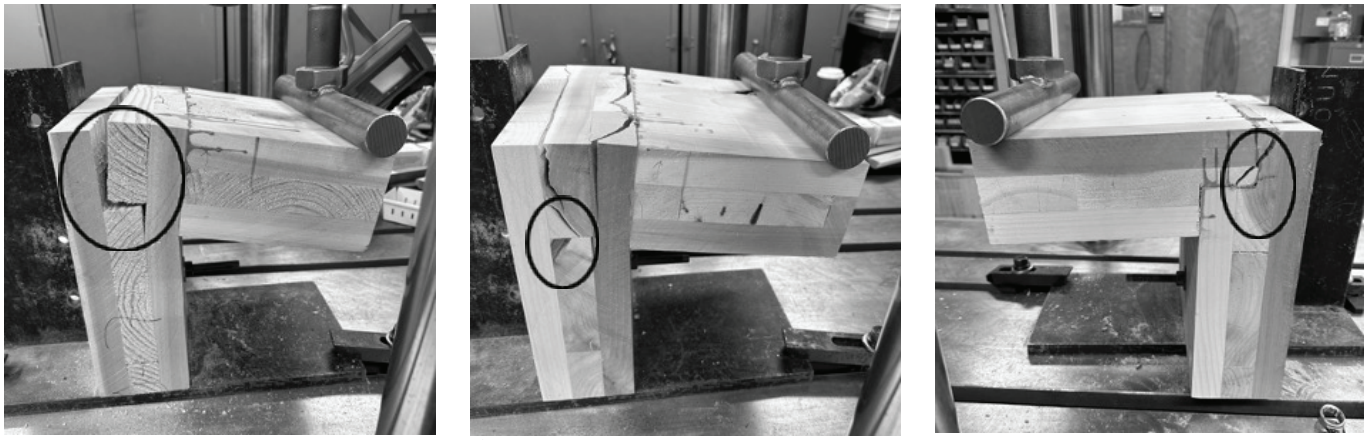

(a) DC-MGF (b) DC-RS (c) LC-WF

(d) LT-MGF (e) DT-JGF (f) LT-JGF and WF

Figure 7. Examples of failure modes of CLT specimens showing (a) to (f).

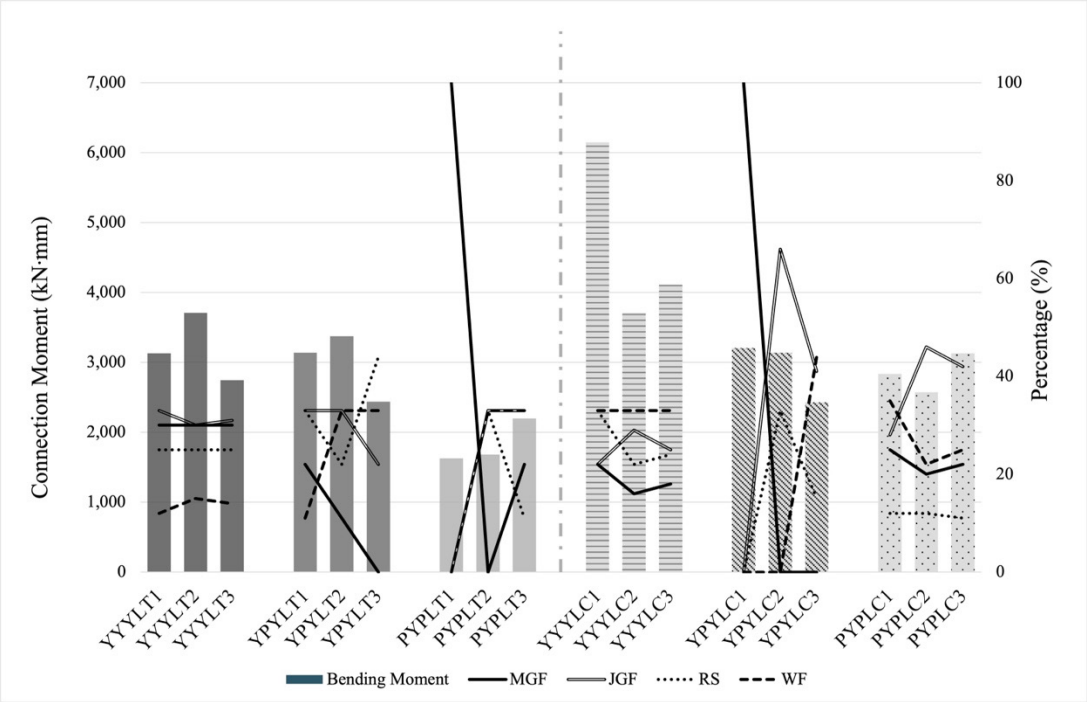

Figure 8. CLT connection moment resistance and failure modes for connections in CLT assemblies with different wood combinations.

40% experiencing MGF and 30-60% showing JGF. Specimens PYPLT1 and YPYLC1 demonstrated complete failure within the CLT material, exhibiting 100% MGF, indicating delamination. These findings emphasize the need to enhance the adhesive strength of the raw CLT materials. Additionally, there is a critical need to improve the adhesive bonding quality during the fabrication of lap joints, potentially through controlling the moisture content of the materials and utilizing adhesives more suitable for end-grain wood bonding, to improve the overall durability and structural integrity of CLT assemblies.

Conclusions

Dowel joints may offer advantages over lap joints, particularly under compression, due to their mechanical interlocking, which can enhance connection moment resistance. In contrast, lap joints were more variable, with some configurations demonstrating more inconsistency, particularly under tension loading. The study also identified potential trends across different materials and wood species, such as YPY, showing a tendency for improved performance when configured as dowel joints under compression.

Dowel joints may be more suitable for applications requiring higher resistance to compressive forces. Conversely, lap joints may require further optimization to improve their performance under tension, particularly in adhesive bonding techniques. The observed delamination and rolling shear failures highlight the need for improved adhesion and better control of properties of the parent CLT during manufacturing.

Overall, this study provides valuable insights into the performance of different CLT joinery configurations. It offers preliminary guidance for future improvements in design to optimize structural integrity and durability in furniture and other engineered wood products made of CLTs. However, further research with increased replication and broader material testing is essential to validate and expand these findings.

References

Adhikari S, Quesada H, Bond B, Hammett T (2020) Potential of hardwood lumber in cross laminated timber in North America: A CLT manufacturer's perspective. MTCJ 3(1):1–9.

Altinok M, Taş HH, Çimen M (2009) Effects of combined usage of traditional glue joint methods in box construction on strength of furniture. Mater Des 30(8):3313–3317. https://doi.org/10.1016/j.matdes.2008.12.004

Çetin Yerlikaya N, Aktaş A (2012) Enhancement of load-carrying capacity of corner joints in case-type furniture. Mater Des 37:393–401. https://doi.org/10.1016/j.matdes.2012.01.010

Chen M, Lyu J (2018) Properties of double dowel joints constructed of Medium Density Fiberboard. Maderas. Ciencia y Tecnología 20(3):369–380. https://doi.org/10.4067/S0718-221X2018005003801

Chúláin CU, Llana DF, Hogan P, McGetrick P, Harte AM (2023) Bending characteristics of CLT from recovered spruce. World Conference on Timber Engineering (WCTE 2023):888–894. https://doi.org/10.52202/069179-0121

Hassler C, McNeel JF, Denes L, Norris J, Bencsik B (2022) Challenges facing the development and market introduction of hardwood cross-laminated timbers. For Prod J 72(4):276–283. https://doi.org/10.13073/FPJ-D-22-00048

Karacabeyli E, Douglas B, FPInnovations (Institute), Binational Softwood Lumber Council (2013) CLT handbook: Cross-laminated timber.

Ma Y, Si R, Musah M, Dai Q, Xie X, Wang X, Ross RJ (2021) Mechanical property evaluation of hybrid mixed-species CLT panels with sugar maple and white spruce. J Mater Civ Eng 33(7):04021171. https://doi.org/10.1061/(ASCE)MT.1943-5533.0003760

Maleki S, Haftkhani AR, Dalvand M, Faezipour M, Tajvidi M (2012) Bending moment resistance of corner joints constructed with spline under diagonal tension and compression. J For Res 23(3):481–490. https://doi.org/10.1007/s11676-012-0288-7

Nicholls T, Crisan R (2002) Study of the stress-strain state in corner joints and box-type furniture using finite element analysis (FEA). Holz Als Roh-Und Werkstoff 60(1):66–71. https://doi.org/10.1007/s00107-001-0262-0

Satir E, Adhikari S, Hindman DP (2024) Evaluation of bending and shear properties of mixed softwood & hardwood cross-laminated timbers. J Build Eng 96:110646. https://doi.org/10.1016/j.jobe.2024.110646

Sciomenta M, Spera L, Bedon C, Rinaldi V, Fragiacomo M, Romagnoli M (2021) Mechanical characterization of novel homogeneous beech and hybrid beech-Corsican pine thin cross-laminated timber panels. Constr Build Mater 271:121589. https://doi.org/10.1016/j.conbuildmat.2020.121589

Thomas RE, Buehlmann U (2017) Using low-grade hardwoods for CLT production: A yield analysis. *In* Möttönen V, Heinonen E, eds. *Proceedings of the International Scientific Conference on Hardwood Processing* (ISCHP2017) September 25-28, 2017, Lahti, Finland (Natural Resources Institute of Finland, Helsinki):199-206, USDA Forest Service, Northern Research Station. https://research.fs.usda.gov/treesearch/55018